In-situ Study of Single Pharmaceutical Granule Drying using Synchrotron X-ray Imaging

A Thesis Submitted to the College of Graduate and Postdoctoral Studies

in partial fulfillment of the requirements for the degree of

Master of Science

in the Department of Chemical and Biological Engineering

University of Saskatchewan

Saskatoon

By

Carter Blocka

Permission to Use

The author has agreed that the Libraries of the University of Saskatchewan may make this thesis freely available for inspection. Moreover, the author has agreed that permission for extensive copying of this thesis for scholarly purposes may be granted by the professor(s) who supervised the thesis work recorded herein or, in their absence, by the Head of the Department of Chemical and Biological Engineering or the Dean of the College of Graduate and Postdoctoral Studies. Copying or publication or any other use of the thesis or parts thereof for financial gain without written approval by the University of Saskatchewan is prohibited. It is also understood that due recognition will be given to the author of this thesis and to the University of Saskatchewan for any use of the material of the thesis.

Requests for permission to copy or to make other use of the material in this thesis in whole or in part should be addressed to:

Head of the Department of Chemical and Biological Engineering

University of Saskatchewan

57 Campus Drive

Saskatoon, Saskatchewan

S7N 5A9

Canada

OR

Dean

College of Graduate and Postdoctoral Studies

University of Saskatchewan

116 Thorvaldson Building, 110 Science Place

Saskatoon, Saskatchewan S7N 5C9 Canada

Abstract

The drying process of wetted granules using common methods such as fluidized bed drying is a key unit operation in the pharmaceutical tableting industry. To ensure homogeneity and product quality for a wide range of formulations in the final tableted product, the monitoring of changes to an individual granules structure, and therein its composition and the associated properties, is essential. Granule drying can occur very rapidly, and many pharmaceutical powders are opaque in nature. Lab-based methods are therefore unable to capture the drying process occurring internally within the individual granules. Comparatively, the use of in-situ synchrotron X-ray imaging techniques allows for fast processes such as single pharmaceutical granule drying to be visualized due to the higher photon flux, good stability, and higher spatial and temporal resolutions that lead to a much faster method than conventional lab-based X-ray imaging.

This study employs the use of synchrotron X-ray imaging techniques to investigate the internal changes of single pharmaceutical granules and how the removal of moisture influences the thermal properties of the individual granules to better predict the drying process. A single granule drying method was implemented to obtain quantitative information of the granule drying process. The liquid binder of water was used with pure components and binary mixtures composed of one active pharmaceutical ingredient and one excipient to produce individual wetted granules for drying. The pharmaceutical powders include the active ingredients acetaminophen and carbamazepine, in addition to common excipients such as microcrystalline cellulose and lactose monohydrate.

A lab-based analysis investigated the effects of moisture content and porosity on the thermal conductivity and specific heat capacity of the pharmaceutical materials. A transient line heat source method was used, with relationships established between thermal conductivity and the volumetric specific heat capacity with porosity and moisture content for the pharmaceutical ingredients. In general, all compositions were observed to have a decrease in porosity with an increase in moisture content, with the thermal properties increasing with an increase in moisture content that followed a three-parameter predictive model for both the thermal conductivity and volumetric specific heat capacity. For APAP, the thermal conductivity increased from 0.171 W/(m k) to 0.402 W/(m k) and the volumetric specific heat capacity increased from 1.300 MJ/(m3 K) to 2.265 MJ/(m3 K) with a change in moisture content from 4.98 % to 14.91 %; the

thermal conductivity of MCC increased from 0.127 W/(m k) to 0.360 W/(m k) and the volumetric specific heat capacity increased from 0.701 MJ/(m3 k) to 1.739 MJ/(m3 K) with a moisture change from 4.55 % to 30.07 %; thermal conductivity of LMH increased from 0.181 W/(m k) to 0.692 W/(m k) and the volumetric specific heat capacity increased from 1.145 MJ/(m3 K) to 2.716 MJ/(m3 K) with a change in moisture content from 1.19 % to 22.75 %.

In-situ synchrotron-based X-ray techniques were used to investigate the dynamic drying of single pharmaceutical granules, quantifying internal changes occurring over the drying time. For most samples, the drying time and granule composition were determined to significantly influence the evolution of the pore volume and the moisture content, with the initial air volume fraction being as low as 0.02 and increasing to as much as 0.38 with the moisture ratio decreasing from 1.00 to as low as 0.00 throughout the drying process. Granules containing MCC were observed to shrink during the drying process, decreasing by up to 25.2 % in volume, with all other materials not observing shrinkage effects. Drying gas velocity and temperature were found to have mixed significance on the rate of increasing pore connectivity and the removal of moisture, with sample composition influencing these changes. This is easily seen in examples such as 80LMH20APAP, where the increase in velocity from 0.02 m/s to 0.10 m/s allows for a larger decrease in the moisture ratio, with increasing temperature from 25 °C to 40 °C observed to further decrease the moisture ratio over the same drying time. The effects of hydrophobicity and hydrophilicity were also observed using carbamazepine and acetaminophen respectively, with the influences of carbamazepine's material properties being minimal in both pure and binary mixtures, whereas acetaminophens hydrophilic nature was dominant in all granules that it is present, with acetaminophen loadings of 20 % to 50 % influencing the drying behaviour for both lactose monohydrate and microcrystalline cellulose. The changes in the moisture content were further analyzed for all materials and fit to nine thin-layer drying models, with the Henderson and Pabis model producing the best predictions for the single pharmaceutical granules used in this work, with R^2 values ranging between 0.635 and 0.998, with 83.3% of the drying models possessing an R^2 greater than 0.90.

The monitoring of the single pharmaceutical drying process using in-situ synchrotron X-ray imaging techniques was, for the first time, demonstrated with data collected on the pore volume evolution and changes to the moisture content obtained. This study revealed how individual

pharmaceutical granules were affected by both the velocity and temperature of the drying gas. The information gained from this research includes a three-parameter model to predict the thermal properties of the pharmaceutical granules that can be used in conjunction with the thin-layer modelling of the drying process of the single pharmaceutical granules, that will benefit the selection of materials and process conditions for drying processes in the pharmaceutical industry.

Acknowledgements

I would like to express my most sincere gratefulness to my supervisor, Dr. Lifeng Zhang, for his constant support and guidance throughout this project, whose patience and motivation through his wonderful mentorship helped to ease the challenge of research even in the most difficult of times.

I would like to thank Dr. Ning Zhu from the Canadian Light Source for his technical support and aid in synchrotron experiments and his unremitting patience in image processing. I would also like to thank Xiao Fan Ding from the University of Saskatchewan, whose recommendations and advice throughout this research have contributed greatly.

I am further grateful to everyone in the research group, with special thanks to Divyapratim Das, Tolu Emiola-Sadiq, Mojtaba Nabipoor Hassankiadeh, Denis Kalugin, and Amy Coller from the University of Saskatchewan for their assistance in synchrotron experiments.

I would like to thank the Natural Sciences and Engineering Research Council of Canada (NSERC) and the University of Saskatchewan for their financial support during the research.

I would also like to thank my committee chair, Dr. Venkatesh Meda, for providing invaluable suggestions during the research.

Lastly, I would like to thank my family and closest friends for their endless encouragement, interest, inspiration, support, and love.

Table of Contents

List of Figures

List of Tables

Nomenclature

Notation	Description	Units
A,B,C,D,E,F	curve fitting parameters	
a,b,c,g,k_0,k_1,k_2,n	thin-layer model curve fitting parameters	
Ar	Archmiedes number	
C_p	specific heat capacity	J/(kg K)
d_{50}	median particle size	m or μm
D_{eff}	moisture diffusion coefficient	m^2/s
d_{peff}	effective particle diameter	m or μm
d_{pi}	individual particle size	m or μm
d_{sv}	average particle diameter	m or μm
E_i	exponential integral	
g_a	gravitational acceleration constant	9.81 m/s^2
k	thermal conductivity	W/(m K)
k_g	thermal conductivity of the gas	W/(m K)
k_l	liquid thermal conductivity	W/(m K)
k_s	solid thermal conductivity	W/(m K)
k_s^*	thermal conductivity of the solid/liquid phase	W/(m K)
l	sample thickness	cm
MR	moisture ratio	
N/N_0	attenuation	
q	heat input	W/m
R	radius of the sample container	mm
r	radius	m
r_d	distance	mm
Re_{mf}	minimum fluidization velocity Reynolds number	
t	time	s or min
T	temperature	°C or K

t_h	heating time	s or min
u	gas velocity	m/s
u_{mf}	minimum fluidization velocity	m/s
X	moisture content	% or fraction
X_0	initial moisture content	% or fraction
X_{eq}	equilibrium moisture content	% or fraction
x_i	mass fraction	fraction
α	thermal diffusivity	m^2/s
ΔT	temperature rise	°C or K
ε	porosity	% or fraction
μ	linear attenuation coefficient	cm^{-1}
μ_a	linear attenuation coefficient of air	cm^{-1}
μ_s	linear attenuation coefficient of solids	cm^{-1}
μ_w	linear attenuation coefficient of water	cm^{-1}
v	dynamic viscosity	$(N\ s)/m^2$
ρ	density	kg/m^3 or g/cm^3
ρ_b	overall bulk density	kg/m^3 or g/cm^3
ρC_p	volumetric specific heat capacity	$MJ/(m^3\ k)$
ρC_p	volumetric specific heat capacity of the overall system	$MJ/(m^3\ k)$
$\rho C_{p,g}$	volumetric specific heat capacity of the gas	$MJ/(m^3\ k)$
$\rho C_{p,l}$	liquid volumetric specific heat capacity	$MJ/(m^3\ k)$
$\rho C_{p,s}$	solid volumetric specific heat capacity	$MJ/(m^3\ k)$

$\rho C_{p,s}^{*}$	volumetric specific heat capacity of the solid/liquid phase	MJ/(m^3 k)
ρ_g	gas density	kg/m^3 or g/cm^3
ρ_l	liquid density	kg/m^3 or g/cm^3
ρ_p	particle skeletal density	kg/m^3 or g/cm^3
ρ_p^{*}	adjusted skeletal density	kg/m^3 or g/cm^3
ρ_{pa}	particle density	kg/m^3 or g/cm^3

Abbreviations

Abbreviation	Meaning
ANOVA	analysis of variance
APAP	acetaminophen
API	active pharmaceutical ingredient
BMIT	Biomedical Imaging and Therapy Facility
CBZ	carbamazepine
CLS	Canadian Light Source
CT	computed tomography
DSC	dynamic scanning calorimetry
FOV	field of view
HPC	hydroxypropyl cellulose
LMH	lactose monohydrate
MCC	microcrystalline cellulose
PEEK	polyetheretherketone
PID	proportional integral derivative
PLA	polylactic acid
PVP	polyvinylpyrrolidone
R^2	coefficient of determination
RAM	random-access memory
RMSE	root mean square error
ROI	region of interest

Chapter 1 – Introduction

1.1 Organization of the Thesis

This thesis is written in a manuscript-based style consisting of five chapters. Chapter 1 is the thesis introduction, including the organization of the thesis, project motivation, knowledge gaps, objectives, and hypothesis. Chapter 2 includes a literature review of current studies on the granule drying process with emphasis on fluidized bed drying, the granulation process in the pharmaceutical industry, overall drying kinetics and drying kinetics for single particles/granules, and visualization and characterization techniques. Chapter 3 contains the first manuscript which determined the effects on moisture content and porosity on the thermal conductivity and volumetric specific heat capacity of the pharmaceutical powders. Chapter 4 is based on the second manuscript, investigating the dynamic drying in single pharmaceutical granules using synchrotron X-ray micro computed tomography, with extensions to thin-layer drying and modelling added to the thesis. Chapter 5 provides the main conclusions from this work, with recommendations provided for future research. The references associated with each chapter are provided at the end of each chapter for ease of reading and clarity.

1.2 Project Motivation and Knowledge Gap

The overall tableting process can be broken down into three primary operations, as depicted in Figure 1.1. Prior to the drying process, the powder ingredients are permitted to mix and consolidate into larger, individual granules by methods such as wet granulation [1]. The wet granules must then have their moisture removed, with fluidized bed drying often implemented due to the improved mass and heat transfer produced with the direct contact of the drying gas and the powder bed [2]. The then dried granules are tableted by common methods such as roll compaction.

Figure 1.1 – General Tableting Process.

The product quality and homogeneity of the produced tablets are crucial for a wide variety of formulations, with factors such as particle size influencing segregation of the active pharmaceutical ingredient in addition to the packed materials porosity [3,4]. This is further complicated by the presence of multiple granules, possessing a large range of particle shapes and sizes across multiple assorted, non-uniform granules that can lead to poor fluidization and non-uniform product quality [5].

Most studies within the literature into individual granules drying behaviour have limited research at an experimental level, with primary emphasis on the literature surrounding models and simulation [6-8]. As the drying process is often very rapid, especially for a singular granule no larger than a few millimeters in diameter, practical applications are dependent on drying parameters such as the drying gas velocity and temperature.

To better understand internal processes and ensure desirable product characteristics, the application of synchrotron X-ray imaging techniques has received increased attention as an emerging technique to monitor rapidly occurring dynamic processes. Due to the intrinsic opaque nature of pharmaceutical powders and the rapid drying process associated with induvial granule studies, lab-based methods are unable to properly capture the granule drying process fully. To remedy this, synchrotron X-ray imaging techniques possess several advantages [9]:

1. A high flux allows for a decreased exposure time, producing an improved signal-to-noise ratio for much faster computed-tomography compared to conventional methods.
2. Beam tunability to allow for materials of varying densities to be investigated while avoiding k-edge effects in the produced radiograph in addition to producing high contrast images.
3. A high spatial and temporal resolution to allow for an adjustable field of view and high resultant quality of the investigated objects produced radiographs.

1.3 Objectives

The objectives of this project were to employ synchrotron X-ray imaging techniques in conjunction with lab-based methods to:

1. Investigate the single granule drying behaviour of pharmaceutical powders under a range of operating conditions with the aid of synchrotron X-ray applications: and,
2. Predict the drying behaviour of single pharmaceutical granules using thin-layer drying modelling to help estimate thermal properties.

1.4 Hypothesis

Synchrotron X-ray imaging techniques can be employed to capture and visualize the dynamic drying process of single pharmaceutical granules, with quantifiable data obtainable because of the high temporal and spatial resolution associated with synchrotron X-ray micro computed tomography.

1.5 References

[1] Salmon, A. D., Hounslow, M. J., Seville, J. P. K., & ScienceDirect, vendor. (2007). Granulation (1st ed.).

[2] Kim, S. D., & Kang, Y. (1997). Heat and mass transfer in three-phase fluidized-bed reactors—an overview. *Chemical Engineering Science*, *52*(21–22), 3639–3660.

[3] Xiaorong He, Xi Han, LADYZHYNSKY, N., & DEANNE, R. (2013). Assessing powder segregation potential by near infrared (NIR) spectroscopy and correlating segregation tendency to tabletting performance: Pharmaceutical Powders. Powder Technology, 236, 85–99.

[4] Dias, R. P., Teixeira, J. A., Mota, M. G., & Yelshin, A. I. (2004). Particulate Binary Mixtures: Dependence of Packing Porosity on Particle Size Ratio. Industrial & Engineering Chemistry Research, 43(24), 7912–7919. https://doi.org/10.1021/ie040048b

[5] Wan Daud, W. R. (2008). Fluidized Bed Dryers — Recent Advances. Advanced Powder Technology : The International Journal of the Society of Powder Technology, Japan, 19(5), 403–418.

[6] Breinlinger, T., Hashibon, A., & Kraft, T. (2015). Simulation of the influence of surface tension on granule morphology during spray drying using a simple capillary force model. Powder Technology, 283, 1-8.

[7] Mezhericher, M., Levy, A., & Borde, I. (2007). Theoretical Drying Model of Single Droplets Containing Insoluble or Dissolved Solids. Drying Technology, 25(6), 1025–1032. https://doi.org/10.1080/07373930701394902

[8] Mortier, S. T. F. ., De Beer, T., Gernaey, K. V., Vercruysse, J., Fonteyne, M., Remon, J. P., Vervaet, C., & Nopens, I. (2012). Mechanistic modelling of the drying behaviour of single pharmaceutical granules. European Journal of Pharmaceutics and Biopharmaceutics, 80(3), 682–689. https://doi.org/10.1016/j.ejpb.2011.12.010

[9] Danalou, S. Z., Ding, X. F., Zhu, N., Emady, H. N., & Zhang, L. (2022). 4D study of liquid binder penetration dynamics in pharmaceutical powders using synchrotron X-ray micro computed tomography. International Journal of Pharmaceutics, 627, 122192.

Chapter 2 – Literature Review

2.1 Fluidized Bed Drying

Fluidization is the process in which a bed of static particles in a column supported by a distributor plate is permitted to interact with passing gas or liquid stream, transforming the bed into a fluid-like state resulting from the drag forces on the particles equaling the weight of the particles within the bed [1]. The most common of these systems seen in various industries are gas-solid systems and liquid-solid systems [2]. As far as gas-solid systems are concerned, the observed flow regimes in a fluidized bed differ depending on the operating conditions, as seen in Figure 2.1.

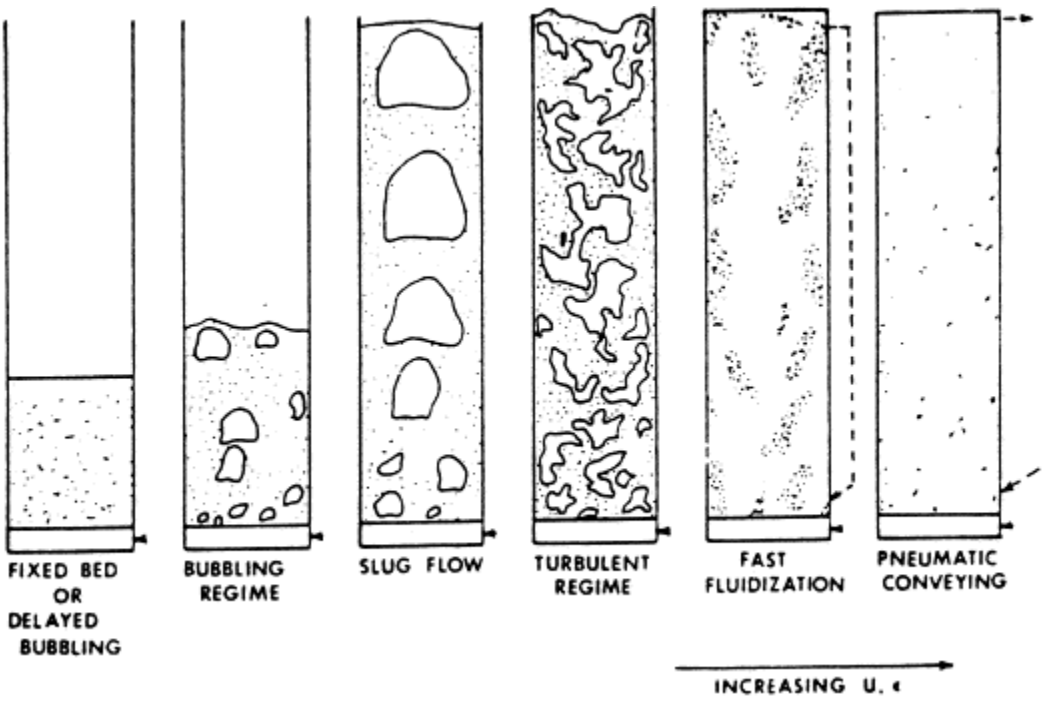

Figure 2.1 - Fluidization regimes for Geldart A particles with increasing gas velocity [3].

For lower gas flow rates, the flow is only permitted in the void spaces found between particles due to the upward drag force not being able to overcome the downward force of gravity, resulting in the particle bed remaining in a fixed state [4]. At this stage, the only observable change to the bed is the pressure drop [1,4]. With increasing the flow rate further, the resultant drag force and pressure drop increase, until at such point the drag force becomes equal to the forces of friction and gravity, creating a fluid-like motion in the bed with constant pressure drop at gas velocities beyond this point [1,4]. This point is referred to as the minimum fluidization velocity, the point at which particles can move apart and slide past one another, with the entire particle-fluid mass becoming a fluid that can be poured or pumped [4]. The value at which the minimum fluidization velocity is found results from a function of several operating parameters if not determined experimentally [1], of which the physical properties of both the particles and fluidizing medium are to be considered. This can be calculated by using the Wen and Yu correlations [5].

Ar is the Archmiedes number, used to determine the motion of fluids due to density differences. Re_{mf} is the minimum fluidization velocity Reynolds number, being the ratio of inertial forces to viscous forces at the minimum fluidization velocity, u_{mf} (m/s). This is accompanied by the effective particle diameter, d_{peff} (m), the gas density, ρ_g (kg/m^3), and the dynamic viscosity, ν (N.s/m^2). The Archimedes number can be evaluated using the average particle diameter, d_{sv} (m), gas density, ρ_g (kg/m^3), particle density, ρ_{pa} (kg/m^3), gravitational acceleration constant, g_a (9.81 m/s^2), and the dynamic viscosity, ν (N.s/m^2). The average particle size can be determined by taking the inverse sum of the ratio between the mass fractions, x_i, and the individual particle sizes, d_{pi} (m).

$$Re_{mf} = (1135.7 + 0.0408Ar)^{0.5} - 33.7 \quad (2.1)$$

$$Re_{mf} = \frac{d_{peff}\rho_g u_{mf}}{\nu} \quad (2.2)$$

$$Ar = \frac{d_{sv}\rho_g(\rho_{pa}-\rho_g)g_a}{\mu^2} \quad (2.3)$$

$$d_{sv} = 1/\sum(\frac{x_i}{d_{pi}}) \quad (2.4)$$

Of those parameters seen in the Wen and Yu correlations [5], the minimum fluidization velocity is affected by the effective particle size (m), the particle density (kg/m^3), the fluidizing media's density (kg/m^3), and the dynamic viscosity of the fluidizing media ($N.s/m^2$).

By further increasing the gas flow rate above the minimum fluidization velocity, the smooth nature of the fluid will change into a bubbling regime, wherein excess gas bubbles through the column. In beds with large height-to-diameter ratios or beds with coarse particles such as Geldart B particles, a slugging regime can be expected [1]. At this point, the observed bubbles within the column grow to the size of the column diameter. Once these bubbles begin to break down as the gas velocity is further increased, a turbulent regime can be observed. This warping and disappearance of bubbles in the turbulent regime are attributed to the high shear forces resulting from the elevated gas velocity, with finer particles becoming entrained towards the top of the column. To recirculate these fine particles, utilization of a cyclone positioned at the top of the column can be used to capture and return the entrained particles to the bed. Beyond the turbulent regime, all particles within the bed become entrained in the fluidizing media, with constant recirculating of the particles required as the system enters pneumatic conveying.

Within the applications of fluidized beds, attractive properties can be seen in comparison to other conventional drying methods. Due to the exceedingly good mixing with high heat and mass transfer capabilities because of the solid and gas phases being in direct contact, a low-cost system with a large production capacity can be offered with a high drying rate [6,7].

2.2 Granulation Process in the Pharmaceutical Industry

Concerning industrial applications of pharmaceuticals, several methods exist to prepare powders for tableting, governed by the size, density, and type of powders utilized [8,9]. In the tableting process, the step of mixing and granulation possesses significant importance on the homogeneity of the mixture to produce a product of high quality and precise formulation in an industry responsible for a wide range of dosages and formulations. The need to ensure pharmaceutical products are safe, effective, and of high quality as defined by regulating bodies [10] can result in a single batch of valuable products going to waste if the active pharmaceutical ingredients are not within an allowable tolerance [11]. To avoid this discarding, the combination of active pharmaceutical ingredients (API's) and their excipients is required to be mixed thoroughly with enough additives such as binders, fillers, preservatives, disintegrants, diluents,

lubricants, and colouring agents [12]. To best achieve this, the various powders are conditioned to granulation processes, wherein the various smaller particles form the contributing powders agglomerate into a larger mass, producing larger stable particles with the desired composition [13]. Of the various granulation processes, several advantages are present in the forms of enhanced flowability and fluidity of granulated particles, improved compressibility of granulated particles, reduction in dust emissions, reduction in segregation, and improved content uniformity of particulate substances [14]. The interactions of such benefits on granulation in the pharmaceutical sector lead to increased manufacturing efficiency, contributed to alongside enhanced mass and heat transfer characteristics.

Examining the macro scale, processing for granulation can be performed utilizing various methods. Roll compaction is a widely used method of dry granulation in the pharmaceutical industry to manufacture free-flowing agglomerates based on the concept of passing a well-mixed powder through two counter-rotating rollers, creating discrete briquettes from the high pressure of direct compaction [13]. Another dry method is the use of dry fluidized bed granulation [13], in which fine cohesive powders allow for granules to converge after a few hours. Alternative to these dry methods, the spray or wet granulation methods permit the powder mixture to agglomerate through liquid bridges to allow particle adhesion [13,15]. The wet granulated powders must then undergo a level of drying before the granules can be compacted and sintered [13], typically performed in a fluidized bed dryer due to the high rate of moisture removal [14]. Other methods of granulation include high shear granulation, extrusion-spheronisation, and drum granulation [13].

While there are many forms of granulation, wet granulation is one of the most frequently used granulation processes in the current pharmaceutical industry. By incorporating a liquid binder during the agitation process, the smaller particles are permitted to form these liquid bridges [13,15], facilitating the granulation of a larger particle. This granulation liquid can be water, alcohols, or mixtures of both [16]. Furthermore, the addition of aqueous solutions containing polymeric binders such as hydroxypropyl cellulose (HPC) or polyvinylpyrrolidone (PVP) has also seen utilization as liquid binders [17]. Following the wet granulation process, a method of drying should be utilized to remove the moisture from the granules. More practical methods of achieving this can be obtained through convective drying via fluidized bed drying or hot oven drying,

although promising alternatives in microwave drying and vacuum-assisted methods exist [18,19]. However, pharmaceutical applications are not recommended for microwave drying resulting from increased degradation of active pharmaceutical ingredients [20].

2.3 Drying Kinetics

The drying period of particles is subject to two phases. In the first drying phase, properties of velocity, temperature, and inlet humidity determine the drying kinetics [21], which produces a constant drying rate as described by Fick's law. This was first proposed by Maxwell [22], where the rate of evaporation is proportional to the radius of the particle, as only the gas side properties influence the particles surface completely covered with water [21]. This is then refined by uniform temperature and diffusion control dependent on the morphology of a particle [23], and considerations to a uniform temperature and diffusion control for multicomponent particles. However, the second drying period presents a falling rate, and the complexity of rate-limiting factors presents themselves in the form of intraparticle resistances.

The second drying period occurs when the surface water surrounding the granule has evaporated, and the water inside the particle is evaporating. For a motionless porous droplet in atmospheric flow, the time-dependence of heat transfer and temperature profiles must be considered, with the developed crust at the surface of the granule limiting mass transfer diffusion [24]. In extension to this notion, the interface between the core and crust of the particle must be considered [25]. A thin boundary layer is formed over the surface of the particle in the second drying phase, attributed to the internal moisture of the particle diffusing through the crust pores. This layer is then removed by advective airflow. A depiction of the water migration in a granule for various drying phases can be seen in Figure 2.2.

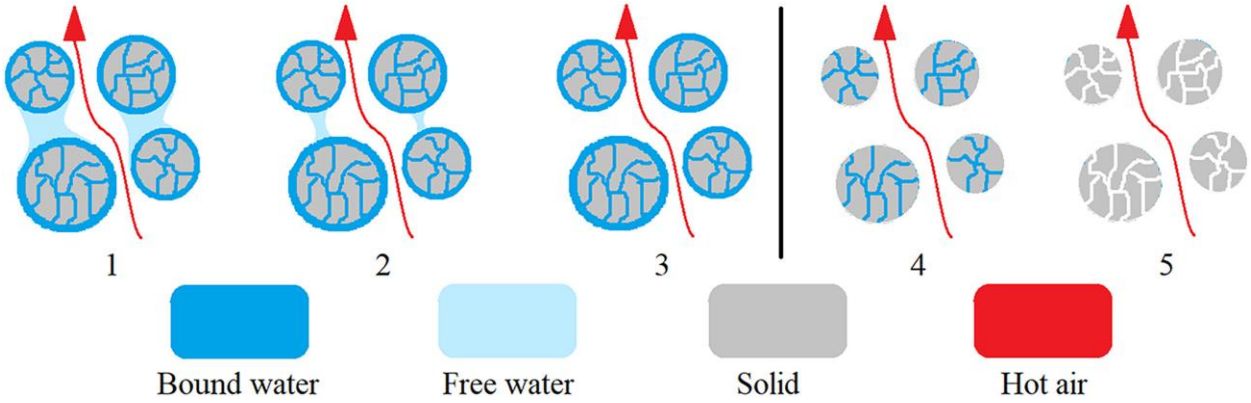

Figure 2.2 - Fluid bed drying phases [26].

Bulk effects for each component, in methods like granulation, strongly influence the properties of the resultant particle [27]. Firstly, highly soluble materials will produce smaller, more dense particles. Second, a component's molecular weight possesses limited diffusive mobility, with components of greater molecular weight concentrating the formation of the particle shell. Lastly, materials like minerals concentrate close to the center of a particle, resulting from increased diffusivity. As the diffusion of a granule's components affects the concentration of each ingredient within the particle, the final product will see an inconsistency from particle to particle. However, as many granules are required to form a single tablet, this variation is negligible.

As previously mentioned, the kinetics of drying is governed by properties of velocity, temperature, and inlet humidity [21], with particle size also affecting the drying rate to an extent [28]. Temperature, being the most influential parameter, affects the rate of water evaporation at the surface of the particle. Under rapid heating, larger particles can be produced by "shocking" the state of a granule, in which the rate of evaporation is so rapid that the redistribution of components is limited, and the particle surface shows breakage and inflation. This is not always desirable, as the effects of temperature can denature proteins specific to protein contained powders and permit carbohydrates to undergo crystallization. Utilizing a lower temperature, these effects are mitigated, with a greater particle shrinkage being observable. Other process parameters further influence drying, although to a lesser extent than that of temperature. Process humidity coincides with feed airflow rates, in addition to temperature and residence time. In decreasing the airflow rate, smaller particles can be produced. In addition to this flowrate, the drying gas utilized can affect the crystallization behaviour of the granule and its components.

The combination of bulk properties and process parameters are seen to greatly influence particle features, with more desirable results able to be obtained by fine-tuning the process parameters. A method of performing this is to define the drying kinetics of a fluidized bed based on mass transfer, generating generalized drying kinetic curves [29]. Such curves can then be used to determine the effect of process parameters on the drying rate of a sample, with increased drying rates desirable alongside decreased drying time, provided the economic impacts of operating a process at elevated conditions are minimized.

2.4 Drying Kinetics for Single Particles/Granules

Several important aspects complicate the investigation of single droplets and granules, comprised of aspects including heat transfer, mass transfer, and momentum transfer. Influenced by a process's parameters of flow, phase transitions, and the presence of mechanical instability, further difficulties arise in the potential of investigations on an industrial level. As seen in fluidized beds, a wide range of polydisperse particles are present, with no feasible means of measuring single, uniform granules within the system. The feasibility of industrial-level investigations are further lessened by the complexity and cost of equipment required for experiments, in addition to the complications of fast-drying kinetics being present. As such, there is a need to investigate single granule systems, removing the complications seen with multiple, non-uniform particles, allowing for a better controlled environment that is precisely controlled for aspects of particle size, gas flow rate, temperature, and evaporation rate. A better control over the process parameters is crucial to many experiments relating to particle drying in industry, with more accurate results being obtainable without the complications of excess noise and fluctuation in the data that may be seen at an industrial level [30,31]. It is important to produce a product of high quality with desirable characteristics, with the use of single granule studies aiding in further understanding the drying process and providing the potential to improve product quality.

In scaling down the drying process from an entire fluidized bed to a single granule, understanding the behaviour of individual granules can reveal important phenomena as principles observed for individual granules often scale up. In studying factors such as temperature, moisture content, and air velocity as they influence a single granules shrinkage, change in porosity, and the removal of moisture, understanding the single granule behaviour can help to predict how a batch of granules will behave under different drying conditions. In

addition, these findings aid in the design and optimization of fluidized bed drying by providing a foundation of how the drying parameters influence the entire bed of granules, improving efficiency and product quality. However, there are several points of contention seen in scaling down the drying process. Methods such as fluidized bed drying contain multiple, non-uniform granules that lead to interparticle effects, introducing variations in drying rates and quality that may not be observed for isolated granules that do not consider effects such as agglomeration or segregation. Furthermore, the scale effects of heat and mass transfer can differ significantly between a single granule and a bed of granules, with the differing distribution of heat affecting the overall drying efficiency. To alleviate these challenges, granule characterization and modular design approaches can be implemented to bridge the gap between laboratory and industrial scale studies, with new and developing techniques capable of providing accurate, real-time data.

In studying single granule and particle drying methods, several pre-existing methods that have been previously investigated can be considered for their advantages and disadvantages in obtaining results. A brief summary of these methods can be seen in Table 1 below. One study by Groenwold et al. had shown promising results in the use of acoustic levitation, allowing for the trouble-free generation of drying curves for stationary particles like that of a drying channel or microbalance [30]. Granules used in this method would not require an intrusive support, thus allowing the entire surface of the particle to be exposed to a stream of tempered air. However, this method produces the complication of acoustic streaming, with the unwanted side-effect of influences on drying as seen between moderate interactions of the ultrasonic waves on the drying process [30]. Alternatively, a sessile-droplet type experiment can be performed, utilizing a simple apparatus with stationary particles to examine drying kinetics [31]. While this method is far simpler than acoustic levitation and not influenced by the effects of acoustic streaming, the granules would be affixed to a substrate, with parts of the particle surface obscured, not mimicking spray drying conditions. Further complications may arise from the substrate that the granules are bound to, with some degree of the influence on drying dependent on coffee ring effects and thermal conductivity. Regardless of the method examined, the core concept remains the same with a stationary particle subjected to mass and temperatures changes from evaporation resulting from an introduced airflow.

Table 2.1 - Comparison of Two Studies on Drying Apparatuses and Methods.

Study	Materials and Methods	Additional Information
Groenwold et al. [30]	γ-Al_2O_3 dried at different air velocities and moderate temperatures to investigate the drying rate.	Acoustic levitation drying chamber with a high accuracy dew point hygrometer.
Janocha and Tsotsas [31]	Sodium Benzoate dried at different air velocities and temperatures, investigating morphology and porosity.	Sessile droplets dried successively in a lab-scale drying chamber. Furthermore, used x-ray micro-tomography.

2.5 Visualization and Characterization Techniques

Visualizing the dynamic drying process of individual granules is greatly beneficial to better understand the drying mechanism in addition to the generated dry granules that have been prepared for tableting. Several noninvasive techniques have previously been implemented in granular mixing, namely: spectroscopic, and tomographic techniques [32], those of which can be extended to elements of the granular drying process.

In terms of pharmaceutical imaging, and furthermore on drying, a noninvasive technique was implemented by Ghijis et al. in a two-dimensional setting using near-infrared imaging [33]. In this specific study, a setup with near-infrared chemical imaging was used to simultaneously measure the size and number of granules in addition to the moisture content of the material based on the absorption spectra. While such a method is capable of providing detailed insight within particulate processes that allow for more robust process models, it is of note that the spectroscopic technique is primarily characterized as a surface scanning technique, with the penetration depth of the photon's dependent on chemical and particle properties [33]. Furthermore, the drying of granules is hypothesized to possess remaining water located in the center of granules [34], with the opaque nature of the materials complicating investigations. In addition to near infrared techniques, Raman spectroscopy is often used in conjunction to reveal information related to the bulk characteristics. In a study by Kogermann et al. [35], Raman spectroscopy was implemented to quantify solid-state changes of materials such as carbamazepine via in situ monitoring for the dehydration process. However, the primary disadvantage to these spectroscopic methods is the limited region of interest as opposed to the entirety of a given sample resulting of the inherent surface bias of the techniques. Tomographic techniques possess the ability to overcome this challenge, with methods such as X-ray computed tomography and magnetic resonance imaging capable of obtaining information on particle homogeneity, although at the disadvantage of a large power source being required in addition to equipment costs that are not feasible for large-scale systems [32]. Crean et al. [36] used X-ray micro-computed tomography in conjunction with confocal Raman mapping to gain information of the intra-granular pore size, binder volumes and to provide spatial and chemical maps of internal granular components.

However, for those aforementioned techniques, there is inherent inability to capture the rapidly changing internal structure of the investigated objects, with dynamic processes occurring much faster than a single scan can be obtained. Lab-based micro-computed tomography can take up to a few hours to few hours within a limited field of view [37], with any changes occurring within a sample during imaging leading to multiple artifacts that can make analysis too involved or the data unusable [38,39]. In contrast, synchrotron-based X-ray imaging techniques can overcome many of the challenges observed within conventional methods, as seen in Figure 2.3.

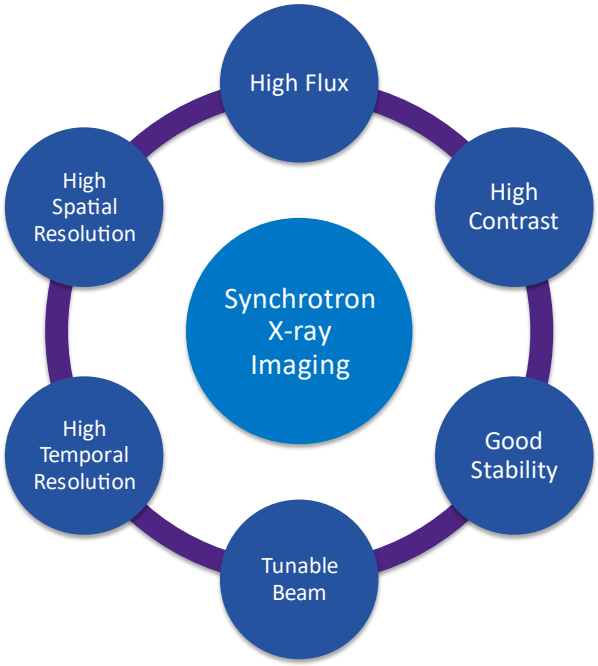

Figure 2.3 - Advantages of Synchrotron X-ray Imaging Techniques.

The application of synchrotron X-ray imaging techniques has been shown as a viable method for investigating dynamic processes related to the pharmaceutical tableting process in recent years. Li et al. [40,41] previously studied the dynamic granulation process in two-dimensional views, for the first time employing synchrotron-based X-ray techniques to observe this phenomenon. The results of these experiments found that produced granules properties were significantly influence by the granulation process, with a single-drop impact method used to demonstrate the wetting and nucleation process within various pure pharmaceutical powders and mixtures. These experiments demonstrated the utility of synchrotron X-ray imaging for studying dynamic processes, with rapidly occurring processes capable of being captured at a very rapid rate. Danalou et al. [42,43] expanded on these works, once again using synchrotron-based X-ray

imaging techniques to visualize the real-time wetting process of pharmaceutical materials. Again, using a single-droplet impact method, granule agglomeration and the rate of pore evolution were quantifiable, further exhibiting the utility of synchrotron-based X-ray imaging techniques for complex and fast process for opaque materials such as pharmaceuticals. An example of the time sequence of X-ray images can be seen in Figure 2.4.

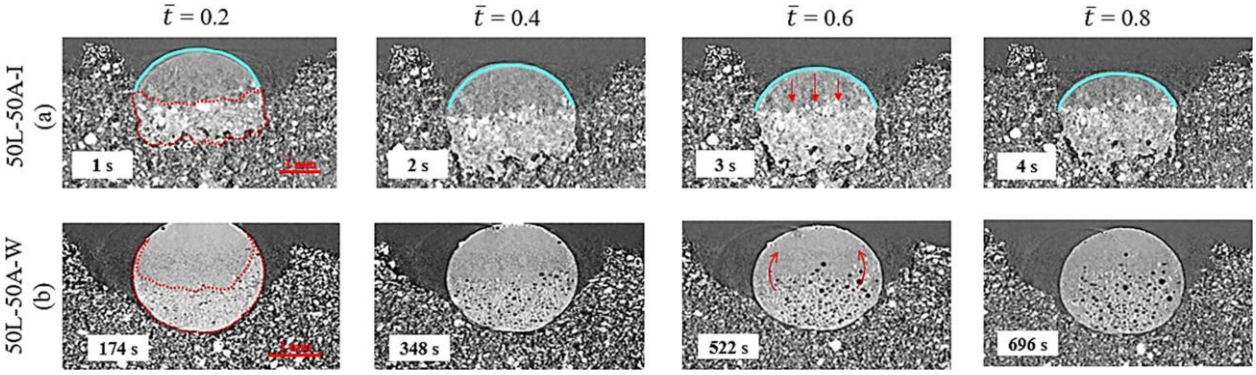

Figure 2.4 - Time CT images of the droplet penetration at time points t = 0.2, 0,4, 0.6, and 0.8. (a) 50L-50A with isopropanol, droplet cap is shown by a blue line and the granule is forming beneath the bed surface. (b) 50L-50A with deionized water, powder covers the droplet and moves inward to form the granule [42].

2.6 Shortcomings Within the Literature

Within the literature, limited research has been conducted on experimental approaches for single granule drying. As the drying process can occur quite rapidly for granules no larger than a few millimeters in diameter, methods such as synchrotron X-ray imaging have not yet been used to investigate the drying process, with research efforts within the literature possessing a primary emphasis on simulation and modelling. These works aim to use theory-based modelling to determine the drying behaviour of single pharmaceutical granules, investigating aspects such as moisture removal, temperature dependence, and granule formation [24,25,44,45]. As seen in these examples, there is a limited use of experimental techniques, with a concentration of theory-based models that provides valuable insight but does not substitute for empirical data. Experimental approaches, such as synchrotron X-ray imaging, can provide real-time observations that can aid in the further development and validation of theoretical models, gaining a more nuanced understanding of the granule's drying behaviour under various drying conditions, leading to a better control of the drying process in pharmaceutical applications.

2.7 References

[1] Green, D. W., Southard, Marylee Z., author, & McGraw-Hill Companies. (2019). Perry's Chemical Engineers' Handbook, 9th Edition (9th ed.).

[2] Khanna, Pugsley, T., Tanfara, H., & Dumont, H. (2008). Radioactive particle tracking in a lab-scale conical fluidized bed dryer containing pharmaceutical granule. Canadian Journal of Chemical Engineering, 86(3), 563–570. https://doi.org/10.1002/cjce.20073

[3] Grace, J. R. (1986). Contacting modes and behaviour classification of gas-solid and other two-phase suspensions. Canadian Journal of Chemical Engineering, 64(3), 353–363.

[4] De Nevers. (2005). Fluid mechanics for chemical engineers (3rd ed.). McGraw-Hill.

[5] Wen, C. Y. and Yu, Y. H. (1966). A generalized method for predicting the minimum fluidization velocity, AIChE J., 12, 610–612.

[6] Briens, & Bojarra, M. (2010). Monitoring Fluidized Bed Drying of Pharmaceutical Granules. AAPS PharmSciTech, 11(4), 1612–1618. https://doi.org/10.1208/s12249-010-9538-1

[7] Luthra. (2021). Developing a Lab-Scale Fluidized Bed Dryer System to Enhance Rough Rice Drying Process. ProQuest Dissertations Publishing.

[8] Van den Ban, & Goodwin, D. J. (2017). The Impact of Granule Density on Tabletting and Pharmaceutical Product Performance. Pharmaceutical Research, 34(5), 1002–1011. https://doi.org/10.1007/s11095-017-2115-5

[9] Šantl, Ilić, I., Vrečer, F., & Baumgartner, S. (2011). A compressibility and compactibility study of real tableting mixtures: The impact of wet and dry granulation versus a direct tableting mixture. International Journal of Pharmaceutics, 414(1), 131–139. https://doi.org/10.1016/j.ijpharm.2011.05.025

[10] Li, B.Y. Government of Canada, Department of Health. (2013). Regulations Amending the Food and Drug Regulations (1475 — Good Manufacturing Practices). Canada Gazette Part II, SOR/2013-74, Project 1475. https://www.gazette.gc.ca/rp-pr/p2/2013/2013-05-08/html/sor-dors74-eng.html

[11] *Food and Drugs Act*, RSC 1985, c. F-27, ss. 30.

[12] Ubhe, Tejaswi & Subscription, Cr. (2020). A Brief Overview on Tablet and It's Types. Journal of Advancement in Pharmacology. 1. 21-31.

[13] Salmon, Hounslow, M. J., Seville, J. P. K., & ScienceDirect, vendor. (2007). Granulation (1st ed.).

[14] Taghavivand, Choi, K., & Zhang, L. (2017). Investigation on drying kinetics and tribocharging behaviour of pharmaceutical granules in a fluidized bed dryer. Powder Technology, 316, 171–180. https://doi.org/10.1016/j.powtec.2016.10.061

[15] Kan, Nakamura, H., & Watano, S. (2018). Effect of collision angle on particle-particle adhesion of colliding particles through liquid droplet. Advanced Powder Technology : the International Journal of the Society of Powder Technology, Japan, 29(6), 1317–1322. https://doi.org/10.1016/j.apt.2018.02.026

[16] Li, C., & University of Saskatchewan, College of Graduate Studies Research. (2021). STUDIES ON GRANULATION, DRYING AND TRIBOCHARGING BEHAVIOUR OF PHARMACEUTICAL POWDERS IN A FLUIDIZED BED DRYER.

[17] Cai, L., Farber, L., Zhang, D., Li, F., & Farabaugh, J. (2013). A new methodology for high drug loading wet granulation formulation development. International Journal of Pharmaceutics, 441(1-2), 790-800.

[18] Chee, S., Johansen, A., Gu, L., Karlsen, J., & Heng, P. (2005). Microwave Drying of Granules Containing a Moisture-Sensitive Drug: A Promising Alternative to Fluid Bed and Hot Air Oven Drying. Chemical & Pharmaceutical Bulletin, 53(7), 770-775.

[19] Berteli, M., Rodier, E., & Marsaioli, A. (2009). Study of the microwave vacuum drying process for a granulated product. Brazilian Journal of Chemical Engineering, 26(2), 317-329.

[20] Loh, Z., Liew, C., Lee, C., & Heng, P. (2008). Microwave-assisted drying of pharmaceutical granules and its impact on drug stability. International Journal of Pharmaceutics, 359(1), 53-62.

[21] Lehmann, S., Oesau, T., Jongsma, A., Innings, F., & Heinrich, S. (2020). Material specific drying kinetics in fluidized bed drying under mechanical vibration using the reaction engineering approach. Advanced Powder Technology Japan, 31(12), 4699-4713.

[22] Maxwell, J.C. (1890). In: Niven, W.D. (ed). Collected scientific papers. Cambridge University Press, Cambridge. http://strangebeautiful.com/other-texts/maxwell-scientific-papers-vol-1.pdf, http://strangebeautiful.com/other-texts/maxwell-scientific-papers-vol-2.pdf

[23] Picknett, R. ., & Bexon, R. (1977). The evaporation of sessile or pendant drops in still air. Journal of Colloid and Interface Science, 61(2), 336–350. https://doi.org/10.1016/0021-9797(77)90396-4 [10] Frohn A, Roth N (2000) In: Frohn A, Roth N (eds) Dynamics of droplets. New York, Springer.

[24] Mezhericher, M., Levy, A., & Borde, I. (2007). Theoretical Drying Model of Single Droplets Containing Insoluble or Dissolved Solids. Drying Technology, 25(6), 1025–1032. https://doi.org/10.1080/07373930701394902

[25] Mortier, S. T. F. ., De Beer, T., Gernaey, K. V., Vercruysse, J., Fonteyne, M., Remon, J. P., Vervaet, C., & Nopens, I. (2012). Mechanistic modelling of the drying behaviour of single pharmaceutical granules. European Journal of Pharmaceutics and Biopharmaceutics, 80(3), 682–689. https://doi.org/10.1016/j.ejpb.2011.12.010

[26] Li, C., Blocka, C., & Zhang, L. (2022). Experimental investigation on drying performance of pharmaceutical granules in a pulsation-assisted fluidized bed dryer. Canadian Journal of Chemical Engineering, 100(9), 2608–2622.

[27] Meerdink, G., & van't Riet, K. (1995). Modeling segregation of solute material during drying of liquid foods. AIChE Journal, 41(3), 732–736. https://doi.org/10.1002/aic.690410331

[28] Sadek, C., Schuck, P., Fallourd, Y., Pradeau, N., Le Floch-Fouéré, C., & Jeantet, R. (2015). Drying of a single droplet to investigate process–structure–function relationships: a review. Dairy Science & Technology, 95(6), 771–794. https://doi.org/10.1007/s13594-014-0186-1

[29] Ciesielczyk, W., & Iwanowski, J. (2006). Analysis of Fluidized Bed Drying Kinetics on the Basis of Interphase Mass Transfer Coefficient. Drying Technology, 24(9), 1153-1157.

[30] Groenewold, C., Möser, C., Groenewold, H., & Tsotsas, E. (2002). Determination of single-particle drying kinetics in an acoustic levitator. Chemical Engineering Journal (Lausanne, Switzerland : 1996), 86(1), 217-222.

[31] Janocha, M., Tsotsas, M. (2021). Analysis of drying parameter effects on porosity evolution during successive layer build-up from dried deposited droplets. Proceedings of the 13th International Conference on Fluidized Bed Technology, 76(2), 292-297.

[32] Nadeem, H., & Heindel, T. J. (2018). Review of noninvasive methods to characterize granular mixing. Powder Technology, 332, 331–350.

[33] Ghijs, M., Vanbillemont, B., Nicolaï, N., De Beer, T., & Nopens, I. (2021). Two-dimensional moisture content and size measurement of pharmaceutical granules after fluid bed drying using near-infrared chemical imaging. International Journal of Pharmaceutics, 595, 120069.

[34] Mortier, S. T. F. C., De Beer, T., Gernaey, K. V., Remon, J. P., Vervaet, C., & Nopens, I. (2011). Mechanistic modelling of fluidized bed drying processes of wet porous granules: A review. European Journal of Pharmaceutics and Biopharmaceutics, 79(2), 205–225.

[35] Kogermann, K., Zeitler, J. A., Rantanen, J., Rades, T., Taday, P. F., Pepper, M., … Strachan, C. J. (2007). Investigating Dehydration from Compacts Using Terahertz Pulsed, Raman, and Near-Infrared Spectroscopy. Applied Spectroscopy, 61(12), 1265–1274.

[36] Crean, B., Parker, A., Roux, D. L., Perkins, M., Luk, S. Y., Banks, S. R., … Roberts, C. J. (2010). Elucidation of the internal physical and chemical microstructure of pharmaceutical granules using X-ray micro-computed tomography, Raman microscopy and infrared spectroscopy. European Journal of Pharmaceutics and Biopharmaceutics, 76(3), 498–506.

[37] Keklikoglou, K., Arvanitidis, C., Chatzigeorgiou, G., Chatzinikolaou, E., Karagiannidis, E., Koletsa, T., Magoulas, A., Makris, K., Mavrothalassitis, G., Papanagnou, E.-D., Papazoglou, A. S., Pavloudi, C., Trougakos, I. P., Vasileiadou, K. Vogiatzi, A. (2021). Micro-CT for Biological and Biomedical Studies: A Comparison of Imaging Techniques. Journal of Imaging, 7(9), 172.

[38] Triche, B. L., Nelson, Jr, John T, McGill, N. S., Porter, K. K., Sanyal, R., Tessler, F. N., McConathy, J. E., Gauntt, D. M., Yester, M. V., Singh, S. P. (2019). Recognizing and Minimizing Artifacts at CT, MRI, US, and Molecular Imaging. Radiographics, 39(4), 1017-1018.

[39] Barrett, J. F., & Keat, N. (2004). Artifacts in CT: recognition and avoidance. Radiographics, 24(6), 1679-1691.

[40] Li, C., Zhu, N., Emady, H. N., & Zhang, L. (2019). Synchrotron-based X-ray in-situ imaging techniques for advancing the understanding of pharmaceutical granulation. International Journal of Pharmaceutics, 572, 118797.

[41] Li, C., Zhang, Y., Zhu, N., Emady, H. N., & Zhang, L. (2021). Experimental investigation of wet pharmaceutical granulation using in-situ synchrotron X-ray imaging. Powder Technology, 378, 65-75.

[42] Danalou, S. Z., Ding, X. F., Zhu, N., Emady, H. N., & Zhang, L. (2022). 4D study of liquid binder penetration dynamics in pharmaceutical powders using synchrotron X-ray micro computed tomography. International Journal of Pharmaceutics, 627, 122192.

[43] Zeinali Danalou, S., Blocka, C., Yang, J., Zhu, N., Emady, H. N., Wasan, E., & Zhang, L. (2023). Advanced 3D and 4D microstructure study of single granule formation for pharmaceutical powders using synchrotron x-ray imaging. AIChE Journal, 69(5), n/a.

[44] Breinlinger, T., Hashibon, A., & Kraft, T. (2015). Simulation of the influence of surface tension on granule morphology during spray drying using a simple capillary force model. Powder Technology, 283, 1-8.

[45] Vandeputte, T., Ghijs, M., Van Hauwermeiren, D., Dos Santos Schultz, E., Schäfer, E., Stauffer, F., De Beer, T., Nopens, I. (2023). Mechanistic modeling of semicontinuous fluidized bed drying of pharmaceutical granules by incorporating single particle and bulk drying kinetics. International Journal of Pharmaceutics, 646, 123447.

Chapter 3 – Effects of moisture content and porosity on the thermal conductivity and volumetric specific heat capacity of pharmaceutical powders

The contents of this chapter have been published in the International Journal of Pharmaceutics.

Contribution of the MSc Student

Conceptualization, writing of the original draft and reviewing, methodology, investigation, and visualization were performed by Carter Blocka. Mojtaba Nabipoor Hassankiadeh aided in the investigation and review of the writing. Dr. Lifeng Zhang provided supervision throughout the research, aiding in the conceptualization, writing review, project administration, and funding acquisition. Dr. Oon-Doo Baik provided further review of the writing.

Contribution of the Chapter

In this chapter, the thermal properties of various pharmaceutical powders were investigated using a transient line heat source method. A quantitative study was performed on the effects of moisture content and porosity for both pure components and mixtures. Empirical correlations were developed to predict the changes in thermal conductivity and volumetric specific heat capacity from these effects using linear regression.

3.1 Abstract

Thermal conductivity and specific heat capacity are two important parameters for the drying process of pharmaceutical materials during methods such as wet granulation that can be observed in the overall tablet manufacturing process. In this study, a transient line heat source method was used for the first time to determine the thermal conductivity and volumetric specific heat capacity of common pharmaceutical components and binary mixtures, with moisture content ranging from 0 % to 30 % w.b and active ingredient loading between 0 % and 50 % by weight, similar to those parameters seen in larger scale fluidized beds. A three-parameter least squares regression empirical correlation relating the thermal properties to moisture content and porosity was evaluated at a 95 % confidence interval, with R^2 values ranging from 0.832 to 0.997. Relationships were established between thermal conductivity, volumetric specific heat capacity, porosity, and moisture content for pharmaceutical ingredients including acetaminophen, microcrystalline cellulose, and lactose monohydrate.

3.2 Introduction

Tableted pharmaceutical products are used in the oral route of drug administration, possessing high dose flexibility in pre-formulated products, and increased stability in shelf life when stored under the proper conditions. In addition to these advantages, pharmaceutical tablets have an ease of portability, handling, and patient acceptance when compared to other forms of drug delivery methods such as intravenous. The global pharmaceutical market has increased steadily over the past two decades, with leading tableted products representing approximately 90 % of the global market for pharmaceuticals intended for human use [1]. As of 2021, approximately 84 % of the highest grossing pharmaceutical products are orally administered, accounting for a market of $35 billion, growing at a rate of 10 % annually [1]. Pharmaceutical tablets are typically manufactured from a combination of an active pharmaceutical ingredient, and one or more excipients used as fillers, stabilizers, disintegrants, binders, or even flavor maskers.

The production of pharmaceutical tablets is dependent on three core processes. In the first step of manufacturing, a pre-formulated powder mixture undergoes mixing and agglomeration via the use of either direct compression, wet granulation, or fluidized bed granulation. Compared to direct tableting that can use microcrystalline cellulose or lactose monohydrate as a diluent/binder [2,3] or wet granulation that uses lactose monohydrate as a diluent/binder [3], fluidized bed granulation sees the use of a binder solution such as water sprayed onto the fluidized powder mixture, with both microcrystalline cellulose and lactose monohydrate being used as diluents. This step is performed to allow for liquid bridges to form between the particles within the powder matrix, permitting the growth and consolidation of wetted granules [4,5]. A form of convective drying must then be used to remove the moisture from the wetted granules, preparing the product for compaction and packaging. Fluidized bed drying is most commonly used for this purpose, achieving a high degree of mass and energy transfer between the drying gas and the granules [6,7]. Finally, the dry granules can be tableted, most commonly performed by roll compaction, before being packaged and sent to the market.

Of notable concern in the manufacturing process, the convective heating used to remove the moisture from the wet granules affects the drying rate, and therein, a plant's level of production. Furthermore, the degradation of active pharmaceutical ingredients (APIs) such as acetaminophen occurs rapidly at elevated temperatures in the presence of trace moisture [8], limiting the operating

conditions of the drying process. In the initial stage of drying, properties of velocity, temperature, and inlet humidity govern the drying kinetics, with the rate of liquid diffusion proportional to the concentration gradient as described by Fick's law [9-11]. Once the surface liquid of the granules has evaporated, transport of liquid to the granule surface through the intergranular pore network occurs, with evaporation further permitting moisture removal [12-15] While aspects of velocity and inlet humidity can be seen to affect the overall drying process, the parameters of temperature and moisture content in the pharmaceutical industry can be seen as a greater concern due to the optimization of production level of a plant and operating cost having to balance with limited API degradation as not to waste expensive batches that are required to meet high quality.

In analyzing and modelling the drying of wet granules, thermal conductivity and the specific heat capacity are essential parameters required in the equation of energy [16]. Furthermore, these parameters influence the rate of heat dissipation within bulk [17]. With the development of various relationships between these thermal properties and materials characteristics such as moisture content and porosity, more robust and precise modelling can be obtained for the design and operation of large-scale pharmaceutical drying processes.

For various forms of pure APAP, Sacchetti [18] employed dynamic scanning calorimetry (DSC) method and investigated the relationship between molar heat capacity and temperature, with results ranging from −40 °C to 200 °C. The results were observed to be linear, with the relative stability of polymorphs observed to be in lower heat capacities and free energy as a consequence of their crystallographic packing arrangements. In the study performed by Krok et al. [19], the thermal properties of common pharmaceutical excipients such as MCC and lactose were investigated for various temperatures between 20 °C and 120 °C in addition to changes in relative density from 0.4 to 0.9. In some cases, the results were modelled to be approximately linear, with non-linear behaviour observed in results where modified intermolecular forces caused by microstresses were postulated to affect the empirical model. Picker and Hoag [20] have furthered the knowledge of materials such as MCC, with results showing that the thermal properties of this material are affected by the addition of water, lowering the transition temperatures when investigated by modulated temperature DSC between 20 °C and 270 °C at a heating rate of 60 °C/min with granules composed of 50 %w/w to 130 %w/w water. Based on the results of these studies, the drying process of common pharmaceutical components can only be estimated using

the thermal properties of pure components in the absence of moisture. However, the thermal properties of pharmaceutical formulations are influenced by the components, with the thermal conductivity and heat capacity expected to be different for changes in material loading, porosity, and moisture content seen during the drying process. Therefore, there is a necessity in the measurement of the thermal properties of common pharmaceutical components and formulations under a variety of conditions to develop and apply correlations that can be used to predict the drying behaviour observed before blending and compaction in the overall tablet manufacturing process.

While more robust methods such as modified differential scanning calorimetry (DSC) can be used to simultaneously determine the thermal properties of a material for various temperatures, the preparation and retrieval of results can be expensive and time-consuming, with the small amount of sample required for these measurements to be placed with extreme caution as not to generate large measurement errors. Furthermore, DSC possesses the weakness of the pressure of the sample increasing with the heating in a hermetic pan, not allowing for the specific heat to be measured under a constant pressure. Comparatively the transient heat line source method is an inexpensive method capable of obtaining results very quickly and reliably, as the repeatability of measurements possesses a low deviation. Furthermore, there is a lacking presence of thermal data for pharmaceutical materials, with no data present for binary mixtures and the effect of moisture and porosity on their thermal properties. Therefore, the transient heat line method was selected as a rapid and reliable method to quickly determine the thermal properties in an inexpensive manner.

The transient line heat source method can be applied to both fluid bed granulation and tableting processes. In fluid bed granulation, this method can be used to measure the thermal conductivity of the granules and the bed, monitoring how the thermal properties may change with a change in moisture content. In tableting, the method can be employed to measure the thermal conductivity of the tablet and the powder mixture used in the formulation of tablets during the compaction process, evaluating how the effect of packing can change the thermal properties. By measuring the temperature response of the material to a sudden heat input, the transient line heat source method can provide information about the thermal properties of the material. This information is useful for optimizing process parameters, such as temperature and time, to ensure product quality and consistency in both the drying process and tablet manufacturing as a whole.

In comparison to other methods such as DSC or TGA, laser flash [21], transient plane source [22], and hot wire method [23], the transient heat line method is quite robust; being cost effective, rapid, repeatable, and the applicability to a wide range of materials and mixtures due to the ease of use. Furthermore, the transient heat line source method possesses the advantage of not requiring investigation at high temperatures, as the resultant temperature curves do not change more than a few degrees (from ambient temperature of approximately 24 °C) before cooling back down to the original temperature.

The objectives of this study are (a) to investigate the thermal conductivity and volumetric heat capacity of acetaminophen (APAP), microcrystalline cellulose (MCC), and lactose monohydrate (LMH) for pure components and binary mixtures, and (b) to determine the relationships between thermal conductivity and volumetric heat capacity with porosity, moisture content, and sample composition for these common pharmaceutical materials. Both fluid bed granulation and fluid bed drying can be more accurately modelled, with parameters of moisture content and porosity changing during these dynamic processes.

3.3 Theory and Modelling

Current modelling methods for predicting the thermal properties of pharmaceuticals are lacking in accuracy when investigating the complex interactions of multicomponent systems. Determining the simultaneous effects of moisture content and porosity, a better estimate of the thermal values can be obtained, which are useful in equations of heat and mass balance. Furthermore, the effect of API loading on the thermal properties of excipients has not been investigated alongside the changes observed from both moisture content and porosity, making the modelling of mixtures difficult and inaccurate.

In this study, to approximate the thermal conductivity and volumetric heat capacity for granulated media, it can be assumed that a continuous, homogenous, porous system can be represented in the form of a packed bed. For a system such as this, the material composition consists of powdered material, a liquid binder such as water, and air. Assuming constant physical properties, the thermal conductivity and volumetric heat capacity can be approximated by the following equations:

$$k = k_s^*(1-\varepsilon) + k_g\varepsilon \qquad (3.1)$$

$$\rho C_p = \rho C_{p,s}{}^{*}(1-\varepsilon) + \rho C_{p,g}\varepsilon \quad (3.2)$$

where k, $k_s{}^{*}$, and k_g are the thermal conductivity of the overall system, the solid/liquid phase, and the gas, respectively; ρC_p, $\rho C_{p,s}{}^{*}$, and $\rho C_{p,g}$ is the volumetric specific heat capacity of the overall system, the solid/liquid phase, and the gas, respectively; ε being the porosity of the system. The solid/liquid phase influences the wetted properties of the pharmaceuticals, affecting the thermal properties and porosity by

$$k_s{}^{*} = k_s(1-X) + k_l X \quad (3.3)$$

$$\rho C_{p,s}{}^{*} = \rho C_{p,s}(1-X) + \rho C_{p,l} X \quad (3.4)$$

$$\varepsilon = 1 - \left(\frac{\rho_b}{\rho_p^*}\right) \quad (3.5)$$

$$\rho_p^* = \rho_p(1-X) + \rho_l X \quad (3.6)$$

Where k_s and k_l are the solid and liquid thermal conductivity, respectively; $\rho C_{p,s}$ and $\rho C_{p,l}$ is the solid and liquid volumetric specific heat capacity respectively; ρ_b is the overall bulk density; $\rho_p{}^{*}$ is the adjusted skeletal density; ρ_p and ρ_l are the solid skeletal density and the liquid density respectively; X is the moisture content fraction.

The result of these equations can be seen in equation (3.11) in the Results and Discussion section, in which a parallel empirical correlation is used to fit the experimental data. The application of a parallel empirical correlation for fitting thermal conductivity data is consistent with literature sources such as Guo et al. [17]. With such a method, a very good approximation of the thermal properties can be achieved, with the ability to extract coefficients that represent the contributions of both the solid and liquid phase of moistened media.

3.4 Materials and Methods

3.4.1 Materials

Three common pharmaceutical powders used in the production of acetaminophen products were investigated in this study, with the use of reverse osmosis water as a liquid binder. The physical characteristics and details regarding the pharmaceutical powders can be seen in Table 3.1. The initial moisture content of powders was measured using an HC103 Halogen Moisture Analyzer (METTLER TOLEDO, Canada). Characterization of the pharmaceutical powders was previously performed by Li et al. [24].

Table 3.1 – Properties of Pharmaceutical Powders.

Material	Median particle size, d_{50} (μm) [24]	Particle skeletal density, ρ_p (g/cm^3) [24]	Initial moisture content, M (fraction)	Initial porosity, ε (fraction)	Supplier
APAP	96	1.72	0.0498	0.486	Hebei Jiheng Pharmaceutical
MCC	128	1.61	0.0455	0.693	FMC BioPolymers
LMH	70	1.52	0.0119	0.319	Foremost Farms

3.4.2 Equipment

Transient line heat source methods have been used widely in engineering practices for the measurement of the thermal properties of solid and granular materials. This method involves the use of a needle with a heater and a temperature sensor inside, allowing for current to pass through the heater while the temperature sensor monitors changes over time. When analyzing the time dependence of the temperature sensor while the probe is inserted into a testing media, aspects such as thermal conductivity can be determined. Temperature data obtained from this type of method were previously converted to thermal properties by approximations and equations that existed in the Laplace domain such as in Blackwell's method for determining thermal constants [25]. Further modifications to Blackwell's method derive a general form of a semi-analytical solution as presented in Knight et al. [26], with refined algorithms generated by METER Group [27] that allow for the use of short heating times and mitigated effects of contact resistance and sample diffusivity. For a dual-needle method, the heater and temperature sensor seen in conventional transient heat source methods can be separated. In doing this, the heated needle can apply heat for a set time, while the temperature needle monitors any changes during the heating period and the cooling period. The readings obtained from this process can then subtract the ambient temperature and the drift rate, resulting in the following equations fitting via a linear least squares method [27].

$$\Delta T = \left(\frac{q}{4\pi k}\right) E_i\left(\frac{-r_d^2}{4\alpha t}\right) \qquad t \leq t_h \qquad (3.7)$$

$$\Delta T = \left(\frac{q}{\pi k}\right)\left\{E_i\left(\frac{-r_d^2}{4\alpha(t-t_h)}\right) - E_i\left(\frac{-r_d^2}{4\alpha t}\right)\right\} \qquad t > t_h \qquad (3.8)$$

Where ΔT is the temperature rise at the measuring needle; q is the heat input at the heated needle; k is the thermal conductivity; r_d is the distance between the needles; α is thermal diffusivity; t and

t_h are time and heating time respectively; E_i is an exponential integral approximated using polynomials [28].

To satisfy the necessary conditions for the vessel sizing to mitigate external effects from the surrounding environment, the radius of the sample container must be much greater than the spacing between the probes. This can be calculated by

$$R > 2.6\sqrt{\alpha t} \tag{3.9}$$

Where R is the radius of the sample container, α is the thermal diffusivity, and t is the measurement time.

As the values of q, r_d, t, and t_h can be controlled, a linear least squares method can be applied by assuming the value of α that minimizes the square differences between the measurement and the above model and simultaneously produces a result for both α and k. With these parameters known, the volumetric specific heat capacity can be calculated simply by

$$\rho C_p = \frac{k}{\alpha} \tag{3.10}$$

where ρC_p is the volumetric specific heat capacity; k is the thermal conductivity; α is the thermal diffusivity.

A diagram of the apparatus can be seen in Figure 3.1. The sample vessel is an aluminum cylinder, with dimensions of 32 mm diameter × 5 mm thickness × 100 mm length (volume of 80.4 cm^3). A TEMPOS SH-3 sensor (dual needle) with dimensions 1.3 mm diameter, 30 mm length, and 6 mm spacing, was inserted into the center of the sample at the top of the cylinder. The dimensions of the cylinder are large enough to contain the probes, with spacing between the probes and the vessel wall much greater than the spacing between the probes to allow for minimal external effects from the surrounding environment. The sensor was connected to a TEMPOS controller by a DB-15 connector, with the device configured to the diffusivity/heat capacity mode. This mode uses a high-power and a read time of 2 min.

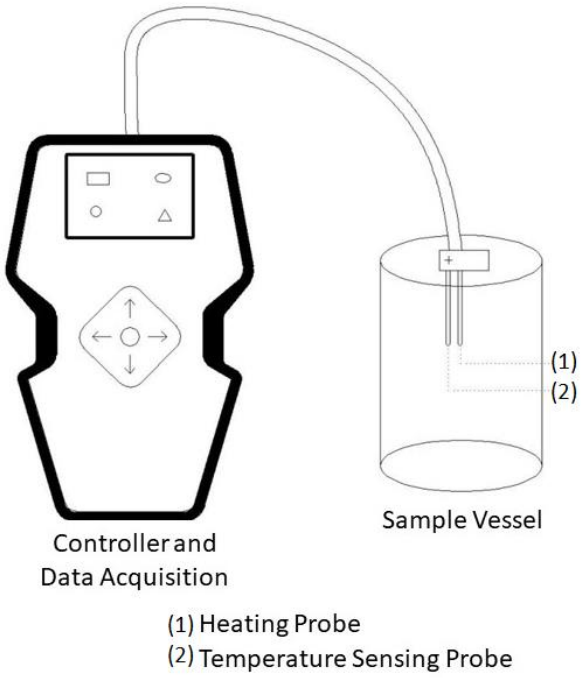

Figure 3.1 - Apparatus setup for the measurement of thermal properties of common pharmaceutical components.

3.4.3 Experimental Procedure

Five replicates of each sample were taken, with the mean and standard deviation calculated for thermal conductivity and volumetric specific heat capacity. The moisture content, M, was measured before each experiment using a HC103 Halogen Moisture Analyzer. The bulk density, ρb, was measured by the ratio of the mass of the sample that filled the vessel per the vessel volume. Weight measurements were taken using a ME4002TE Precision Balance (METTLER TOLEDO, Canada).

The samples were first prepared by measuring out an excess of the unwetted powders into a plastic container, with binary mixtures adhering to a ratio by mass. For binary and wetted mixtures, the samples were mixed thoroughly for 5 min until a homogenous state was reached. The moisture content of the samples was determined before each experiment, with reverse osmosis water added to the powder matrix until the desired moisture content was obtained, except for the unwetted samples that were measured without any additional moisture. To better allow for uniform moisture distribution in the samples, the wetted materials were left for 15 min in an airtight container after water was added to reach mass equilibrium. As observed in Callahan et al. [29], the effects of temperature and relative humidity on the equilibrium moisture content of wetted

pharmaceuticals have been observed to be negligible for materials including MCC and LMH. Furthermore, it was recognized that the use of an airtight container can help to mitigate any potential effects in the short term by preventing the exchange of moisture to the surrounding environment, maintaining a more stable moisture content. However, this is not a foolproof solution, as long-term storage in these containers is still subject to effects of temperature and relative humidity. Therefore, samples were used immediately after preparation, and were stored in airtight containers when not in use. Additionally, samples stored for longer than one day were disposed of and re-prepared, as samples such as those containing primarily LMH at very high moisture contents were observed to segregate after being left unattended overnight. Each sample was also disposed of at the end of each measurement. The empty aluminum vessel was then weighed, and the prepared sample was then inserted into the aluminum vessel until it was filled. In the aluminum vessel, the sample was compacted by a packing rod of a similar diameter to the aluminum vessel until it could no longer compact. The vessel was then refilled and repacked with more samples until filled. At this point, the sample was levelled by the flat edge of an 8″ tapered, metal, micro spatula. The final weight of the filled cylinder was recorded to determine the mass of the added sample, and therein, the bulk density.

With the sample and vessel prepared, the TEMPOS SH-3 was inserted and fixed in the center of the sample at the top of the vessel. When inserting the dual needle, caution was taken to ensure that both probes remained parallel, not forcing the TEMPOS SH-3 if resistance was present. The attached TEMPOS controller was used to record temperature data and automatically calculate thermal properties, with all data collected and stored on the device. When the setup was ready, the diffusivity/heat capacity mode was started and permitted to run to completion. This mode first collects data for 30 s to equilibrate and determine if the temperature drift is below a threshold of 0.002 °C/s. If the temperature drift is below this threshold, then the instrument will automatically enter the active heating mode, otherwise, the equilibration step will repeat. In the active heating mode, a current is applied to the heater needle for 30 s, during which time the sensing needle is monitored, with measurements taken at 1-second intervals. After these 30 s, the heating current is shut off, and the temperature is monitored for an additional 90 s. The starting temperature and drift are then subtracted from temperatures, producing ΔT values that are used to solve equations (7), (8), and (10). The samples were removed by using a 6″, metal scoopula, and the vessel was cleaned with reverse osmosis water and dried with pressurized air.

The obtained data were imported into SPSS Statistics 28 to determine variable significance utilizing ANOVA testing. Furthermore, the data determined to have a significant effect on the thermal conductivity and volumetric specific heat capacity were imported into OriginPro 2021b for nonlinear curve fitting with results from SPSS using the least squares method.

3.5 Results and Discussion

Moisture content for the samples ranged between 0 % and 30 % w.b., with binary mixtures API loading varying from 0 % to 50 % by weight as these ranges are typically seen within the production process of pharmaceutical tableted products. It should be noted that moisture contents beyond 15 % in the presence of high APAP loading were observed to produce a very hard solid that is impenetrable by the thermal probe. Furthermore, LMH is a highly hygroscopic material, observed to quickly form a pseudo-liquid phase at moisture contents between 10 and 23 %, with the further addition of moisture beyond 23 % generating highly unstable readings as the mixture would form 2 phases of liquid and the pseudo-liquid phase that would settle during measurements. For those samples composed of APAP and/or LMH at elevated moisture levels beyond those obtained, readings were unobtainable due to either the inability to insert the probe into the sample without potentially damaging the equipment, or the sample behaving too much like a liquid and producing unstable and unrepeatable results. APAP/LMH mixtures were possible to work with as the combination of the individual difficulties for pure components became complimentary when mixed. As APAP on its own formed a very hard solid and LMH formed more of a slurry, the addition of APAP to LMH was able to convert the slurry to a more solid, wetted material that was workable without the pseudo-liquid phase falling out of the mixture. However, as can be seen in the data, this worked up until around 15% moisture content for higher API loadings, where the previous difficulties of the APAP began to present itself in the material becoming too solid to penetrate with the thermal probe. As recommended by METER Group in the TEMPOS Thermal Properties Analyzer Manual [27], the SH-3 sensor cannot be used in liquids because of the large heat pulse and resulting free convection in liquid samples. In addition to this, it is acknowledged within this manual that it would be very difficult to drill small diameter, parallel holes to accommodate the SH-3 needles in a solid material. Other probes such as the KS-3 sensor could be used for both high and low-viscosity liquids, however, this sensor is not capable of determining the volumetric specific heat capacity or thermal diffusivity required to calculate the thermal

conductivity. Therefore, at the discretion of the manufacturer and what was observed in the application, the results are limited to dry powders and granular material.

The thermal conductivity of all samples was found to increase when the moisture content increased, as the absorption of water into the powder matrix leads to increased heat transfer via conduction as air is displaced. For APAP, the thermal conductivity increased from 0.171 W/(m k) to 0.402 W/(m k) with a change in moisture content from 4.98 % to 14.91 %; MCC increased from 0.127 W/(m k) to 0.360 W/(m k) with a moisture change from 4.55 % to 30.07 %; LMH increased from 0.181 W/(m k) to 0.692 W/(m k) with a change from 1.19 % to 22.75 %. However, the type of material was found to have an effect on the rate at which this increase occurs, with the changes in thermal conductivity for APAP and MCC gradually increasing as the moisture content increased, while LMH was seen to rapidly increase with the first addition of moisture before developing steady growth. Compared to those results observed in Krok et al. [19], the thermal conductivity of unwetted MCC and LMH at the associated porosity are noticeably different for lactose, while MCC matches closely the value reported for Avicel pH 101 [19]. This is likely due to variances in moisture content and the method of packing, with Krok et al. [19] having previously discussed the issue of fracturing behaviour observed with evaporation in hydrous forms of lactose in addition to the influence of microstresses on the intermolecular forces of a sample. The volumetric specific heat capacity was also found to increase for all samples as the moisture content increased, with the similar absorption of water leading to the increased values as compared to air within the pore structure of the material. For APAP, the volumetric specific heat capacity increased from 1.300 MJ/(m3 K) to 2.265 MJ/(m3 K); MCC increased from 0.701 MJ/(m3 k) to 1.739 MJ/(m3 K); LMH increased from 1.145 MJ/(m3 K) to 2.716 MJ/(m3 K). Compared to those results previously seen in the literature [18-20], the volumetric specific heat capacity agrees well for ambient conditions for the initial values of porosity and moisture content observed in each material. Compared to those results seen in Sacchetti [18], the results for unwetted APAP in this study match closely to the documented values. In addition to these findings, the porosity for all samples was observed to decrease with increasing moisture content. This decrease in porosity can be seen in Fig. 3.2, Fig. 3.3, Fig. 3.4 below. The behaviour of decreasing porosity is expected with the increase in moisture content, as the increase in moisture trends the mixtures toward a liquid state, reducing the overall pore volume by replacing the gas phase of air with a liquid phase in water. The range of porosity

as they are influenced by the moisture content for the packed materials can be seen in Figures 3.2-3.4.

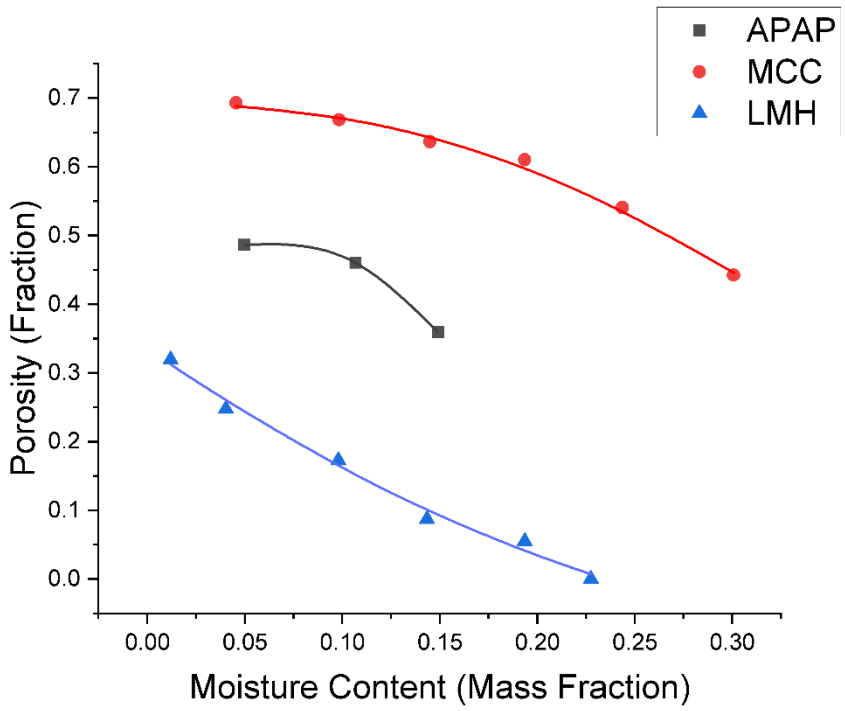

Figure 3.2 - Comparison of experimental results and model results for the porosity of pure components.

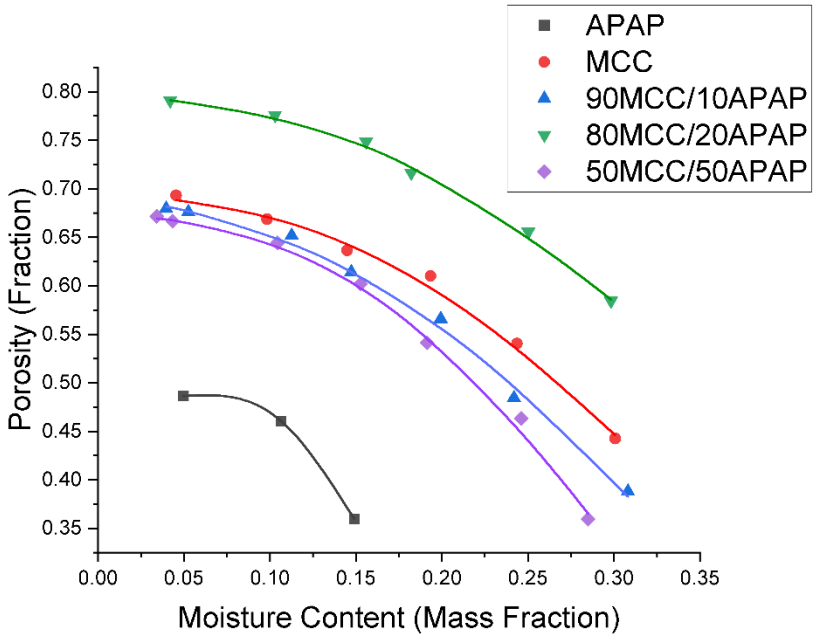

Figure 3.3 - Comparison of experimental results and model results for the porosity of MCC mixtures.

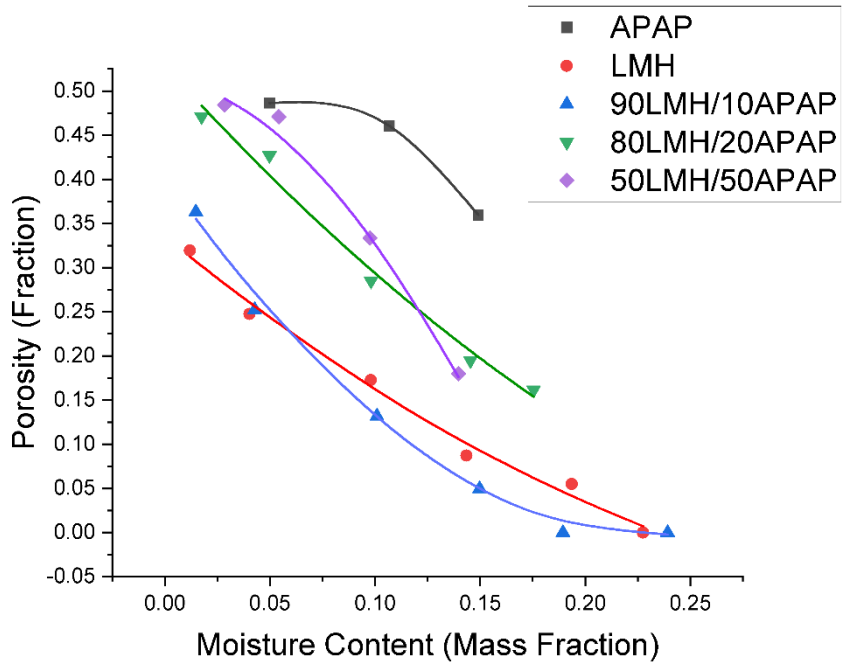

Figure 3.4 - Comparison of experimental results and model results for the porosity of LMH mixtures.

For APAP, the porosity decreased from 48.64 % to 35.96 %; MCC decreased from 69.31 % to 44.25 %; and LMH from 31.95 % to 0 %. Like the results found for thermal conductivity, the changes in porosity for APAP and MCC are gradual, while the changes in LMH occur more rapidly. These experimental values reflect the nature of LMH as a material prone to moisture sorption and caking [30], relating to the higher moisture content that affects bulk density and the proximate composition. For the binary mixtures, it was found that the loading of the API influences the properties of thermal conductivity and volumetric-specific heat capacity. As the loading of the API increases, it is observed that the results trend more closely toward the results of purely the API.

As can be seen in Fig. 3.4, there are several data points that trend closely to or were determined to be zero. The porosity of a sample is expected to decrease with an increase in moisture content. The porosity of the materials becomes zero at high moisture contents due to the filling of void spaces with water, resulting in the reduced ability for particles to move and rearrange. At a certain point, the materials reach a fully saturated state, where there is no additional void space available for water to occupy. On the particle movement and rearranging, as the

moisture content is increased, water molecules coat the surfaces of particles, creating a cohesive force between them. This force results in compaction and further reduction of porosity.

Examining the results for the significance of the parameters on the changes in thermal properties, one-way ANOVA results were obtained and can be seen in Table 3.2. A 95 % confidence interval was used, with results < 0.05 being significant.

Table 3.2 - ANOVA results for the significance of investigated variables on thermal properties.

Parameter	Thermal conductivity significance	Volumetric specific heat capacity significance
Moisture content	<0.001	<0.001
Porosity	<0.001	<0.001

As can be seen from the analysis, there is a significant influence on the thermal properties by the changes in moisture content and porosity.

The dependence of thermal properties on moisture content and porosity of a sample has previously been recognized by Guo et al. [17], where a parallel empirical correlation was combined with a linear regression model to obtain a formula that accounts for both porosity and moisture content. This empirical correlation can be derived using the parameters introduced in (3.1), (3.3), (3.5), and (3.6). By using a least square regression, an expanded model can be obtained as shown below.

$$k = (A * (1 - X) + B * X)(1 - \varepsilon) + C * \varepsilon \quad (3.11)$$

where k is thermal conductivity; A, B, and C are curve fitting parameters; M is the moisture content; ε is porosity. While the first half of the equation represents the thermal conductivity of the wet granule material, the C component represents the thermal conductivity of the air (typically 0.02619 W/(m K) at 25 °C and 1 bara [31]. To better reflect the effect of porosity, the value for C was fixed to the value of thermal conductivity for air with minimal reduction to the obtained R^2 and curve fitting. Equation (11) was used to correlate the experimental data, with coefficients and their standard errors seen in Table 3.3. Fig. 3.5, Fig. 3.6, Fig. 3.7 show the experimental data and the fitted curves.

Table 3.3 - Coefficients and R2 to Eq. (3.11) for common pharmaceutical materials for C =

Material	A (W/(m K))	B (W/(m K))	R^2	RMSE
APAP	0.130 ± 0.074	3.261 ± 0.604	0.996	0.015
MCC	0.308 ± 0.023	1.401 ± 0.084	0.992	0.007
LMH	0.430 ± 0.089	1.837 ± 0.489	0.832	0.072
90MCC/10APAP	0.316 ± 0.013	1.211 ± 0.046	0.996	0.005
80MCC/20APAP	0.449 ± 0.031	2.090 ± 0.109	0.995	0.007
50MCC/50APAP	0.346 ± 0.013	1.555 ± 0.050	0.997	0.005
90LMH/10APAP	0.409 ± 0.077	1.705 ± 0.407	0.882	0.061
80LMH/20APAP	0.419 ± 0.155	2.979 ± 1.061	0.846	0.080
50LMH/50APAP	0.189 ± 0.095	4.823 ± 0.815	0.971	0.035

0.02624 W/(m K)

The correlated results have a relatively good fit to the data as seen by the R2 values. However, the results for MCC and its mixtures are exceptionally good for their fit to the proposed empirical correlation. This empirical correlation works well for systems that have limited moisture diffusion, with the limited moisture evaporation occurring at ambient temperatures allowing for a solid–liquid layer system to be correlated [17].

As seen in Krok et al. [19], several pharmaceutical materials exhibit a linear relationship with thermal conductivity when investigating solely the packing fraction. However, with the introduction of moisture, we can see that a non-linear distribution of the data presents itself, with elevated moisture contents surpassing values observed from solely packing fraction. In addition, the incorporation of terms that involve the moisture content can more accurately predict the experimental values obtained, with improved R^2 and RMSE values in comparison to linear correlations.

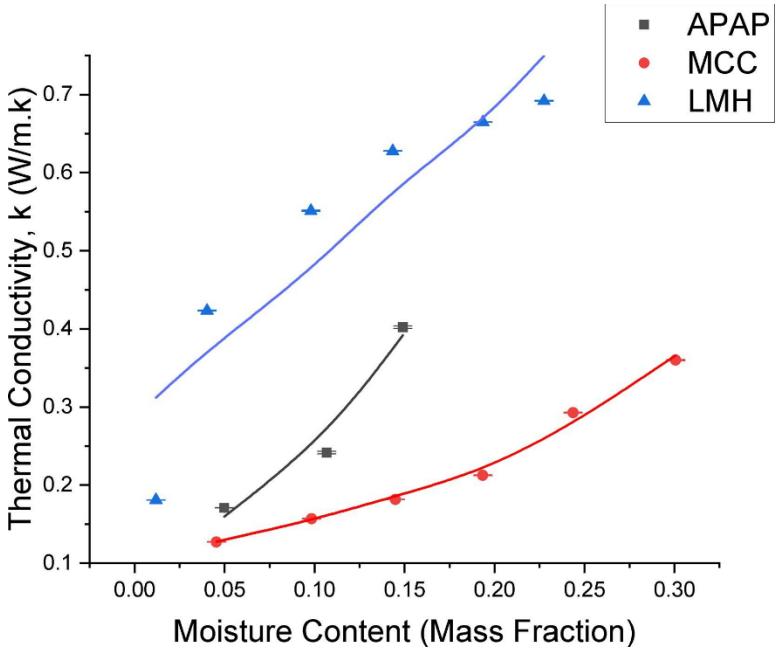

Figure 3.5 - Comparison of experimental results and correlated results for thermal conductivity of pure components using Eq. (3.11).

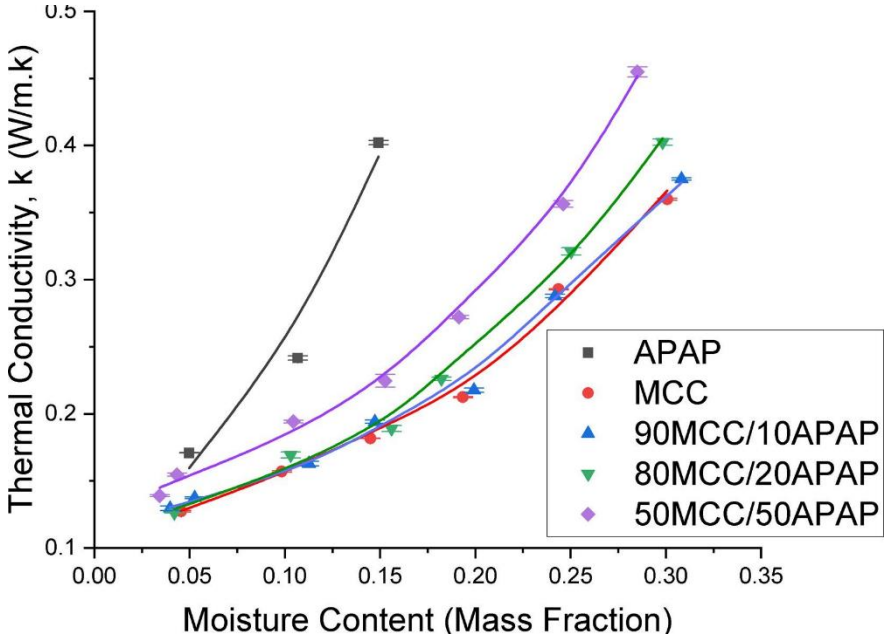

Figure 3.6 - Comparison of experimental results and correlated results for thermal conductivity of MCC mixtures using Eq. (3.11).

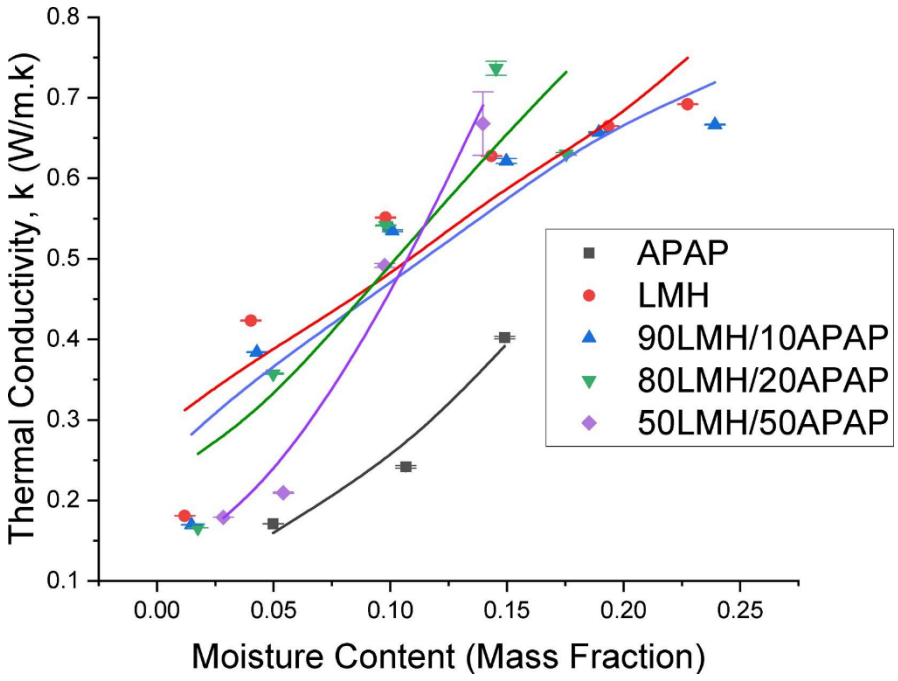

Figure 3.7 - Comparison of experimental results and correlated results for thermal conductivity of LMH mixtures using Eq. (3.11).

Similar to those empirical correlations developed for thermal conductivity, the development of equations for the volumetric specific heat capacity often forms linear or lower-order polynomial correlations with dependence on the sample's moisture content [17,32,33]. Expanding upon a linear correlation, porosity can be considered for the volumetric specific heat capacity in a similar way to equation (10), where similar implementations were made based on equations (3.2), (3.4), (3.5), and (3.6).

$$\rho C_p = (D * (1 - X) + E * X)(1 - \varepsilon) + F * \varepsilon \qquad (3.12)$$

Where ρC_p is the volumetric specific heat capacity, D, E, and F are curve fitting parameters; X is the moisture content; ε is porosity. Equation (12) was used to correlate the experimental data, with coefficients seen in Table 3.4. Figures 3.8-3.10 show the comparison between experimental data and the fitted curves.

Table 3.4 - Coefficients and R^2 to Eq. (3.12) for common pharmaceutical materials for F = 0.0012 MJ/(m^3 K)

Material	D (MJ/(m^3 k))	E (MJ/(m^3 k))	R^2	RMSE
APAP	1.731 ± 0.616	13.370 ± 5.121	0.998	0.127
MCC	2.779 ± 0.330	4.491 ± 1.180	0.905	0.103
LMH	1.804 ± 0.095	6.015 ± 0.520	0.980	0.077
90MCC/10APAP	2.770 ± 0.194	4.230 ± 0.707	0.956	0.078
80MCC/20APAP	4.475 ± 0.412	8.653 ± 1.426	0.968	0.088
50MCC/50APAP	2.846 ± 0.132	8.367 ± 0.501	0.993	0.054
90LMH/10APAP	1.935 ± 0.109	5.401 ± 0.577	0.976	0.087
80LMH/20APAP	2.207 ± 0.354	8.672 ± 2.428	0.920	0.182
50LMH/50APAP	2.187 ± 0.326	10.803 ± 2.803	0.962	0.120

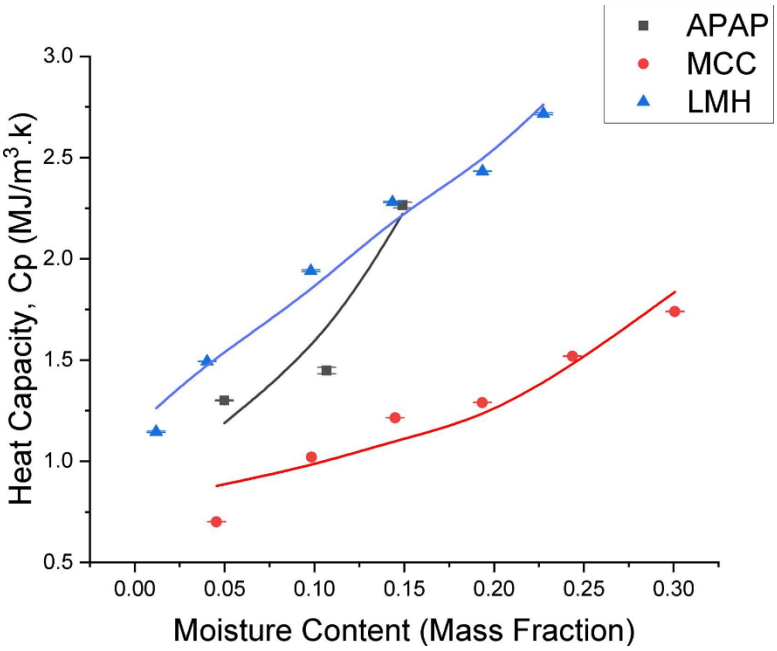

Figure 3.8 - Comparison of experimental results and correlated results for the volumetric specific heat capacity of pure components using Eq. (3.12).

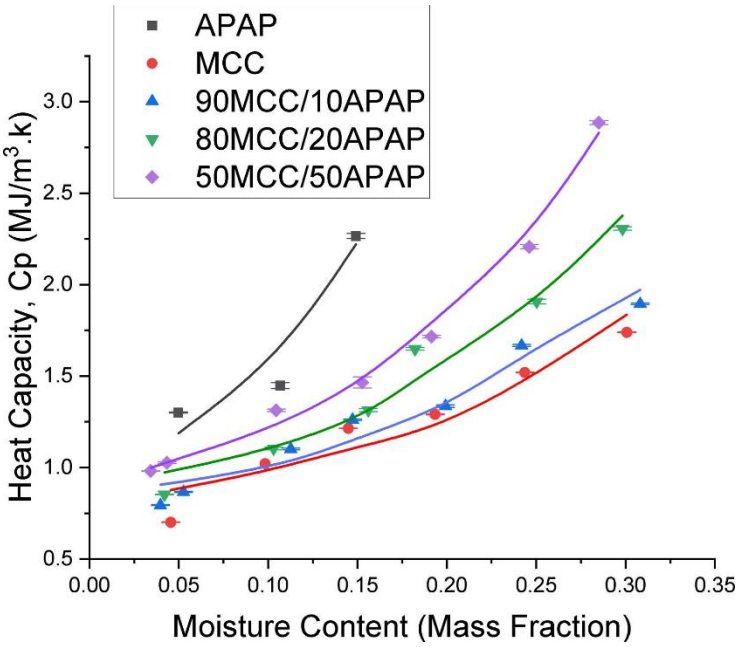

Figure 3.9 - Comparison of experimental results and correlated results for the volumetric specific heat capacity of MCC mixtures using Eq. (3.12).

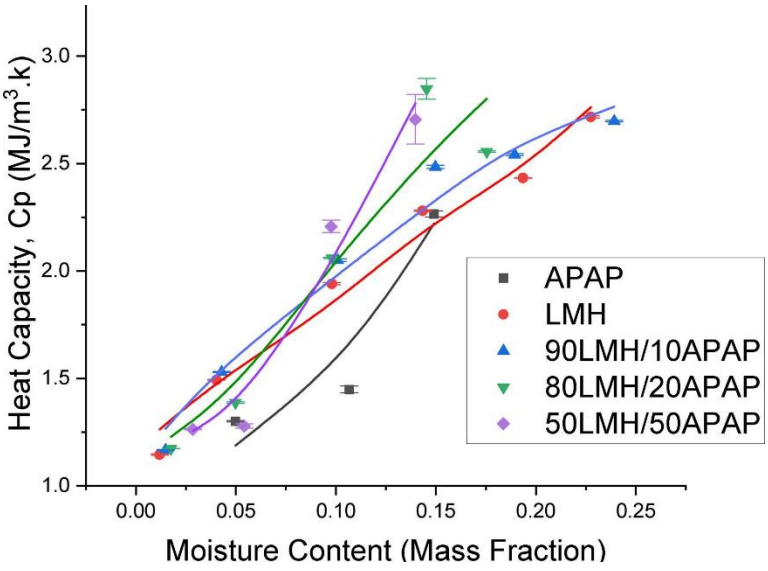

Figure 3.10 - Comparison of experimental results and corrlated results for the volumetric specific heat capacity of LMH mixtures using Eq. (3.12).

However, while the use of an empirical correlation that incorporates the effect of porosity can be seen as a good ability to predict the volumetric specific heat capacity at higher API loading

for all materials, a linear relationship is much better suited for materials greatly composed of MCC. The results for a linear fit of this data can be seen in Table 3.5.

Table 3.5 - Coefficients and R2 to linear regression for common pharmaceutical materials

Material	Slope (MJ/(m^3 K))	Constant (MJ/(m^3 K))	R^2	RMSE
APAP	9.324 ± 4.676	0.721 ± 0.513	0.799	0.190
MCC	3.844 ± 0.275	0.590 ± 0.053	0.980	0.047
LMH	6.923 ± 0.542	1.176 ± 0.077	0.976	0.084
90MCC/10APAP	4.035 ± 0.229	0.639 ± 0.042	0.984	0.047
80MCC/20APAP	5.661 ± 0.424	0.549 ± 0.081	0.978	0.073
50MCC/50APAP	6.818 ± 0.893	0.626 ± 0.157	0.921	0.179
90LMH/10APAP	6.895 ± 0.917	1.231 ± 0.134	0.934	0.144
80LMH/20APAP	10.520 ± 1.992	0.981 ± 0.226	0.903	0.201
50LMH/50APAP	14.227 ± 2.267	0.725 ± 0.205	0.952	0.136

3.6 Conclusions

In this work, a transient line heat source method was applied to determine the thermal conductivity and volumetric specific heat capacity of common pharmaceutical components including APAP, MCC, and LMH and their mixtures. The curve fitting method of a three-parameter non-linear regression using the least squares method produced well-fit correlations for thermal conductivity and volumetric specific heat capacity, with linear regression producing a better correlation for samples composed of primarily MCC. Moisture content and porosity are determined to have a significant impact on thermal conductivity and volumetric specific heat capacity in the tested range of 0 % to 30 %. The obtained correlations could be used to predict thermal conductivity and volumetric specific heat capacity using moisture content and the packed sample porosity.

3.7 Acknowledgements

This research is funded in part by the University of Saskatchewan, the Natural Sciences and Engineering Research Council of Canada, and The Mosaic Company.

3.8 References

[1] Alqahtani, M., Kazi, M., Alsenaidy, M., & Ahmad, M. (2021). Advances in Oral Drug Delivery. Frontiers in Pharmacology, 12, 618411.

[2] Kumar, V., de la Luz Reus-Medina, M., & Yang, D. (2002). Preparation, characterization, and tabletting properties of a new cellulose-based pharmaceutical aid. International Journal of Pharmaceutics, 235(1), 129–140.

[3] Huang, W., Shi, Y., Wang, C., Yu, K., Sun, F., & Li, Y. (2013). Using spray-dried lactose monohydrate in wet granulation method for a low-dose oral formulation of a paliperidone derivative. Powder Technology, 246, 379–394.

[4] Salmon, A., Hounslow, M. J., Seville, J. P. K., & ScienceDirect, vendor. (2007). Granulation (1st ed., Handbook of powder technology ; v. 11).

[5] Kan, Nakamura, H., & Watano, S. (2018). Effect of collision angle on particle-particle adhesion of colliding particles through liquid droplet. Advanced Powder Technology : the International Journal of the Society of Powder Technology, Japan, 29(6), 1317–1322. https://doi.org/10.1016/j.apt.2018.02.026

[6] Chee, S., Johansen, A., Gu, L., Karlsen, J., & Heng, P. (2005). Microwave Drying of Granules Containing a Moisture-Sensitive Drug: A Promising Alternative to Fluid Bed and Hot Air Oven Drying. Chemical & Pharmaceutical Bulletin, 53(7), 770-775.

[7] Berteli, M., Rodier, E., & Marsaioli, A. (2009). Study of the microwave vacuum drying process for a granulated product. Brazilian Journal of Chemical Engineering, 26(2), 317-329

[8] Gilpin, R., & Zhou, W. (2004). Studies of the Thermal Degradation of Acetaminophen Using a Conventional HPLC Approach and Electrospray Ionization-Mass Spectrometry. Journal of Chromatographic Science, 42(1), 15-20.

[9] U Lehmann, S., Oesau, T., Jongsma, A., Innings, F., & Heinrich, S. (2020). Material specific drying kinetics in fluidized bed drying under mechanical vibration using the reaction engineering approach. Advanced Powder Technology : The International Journal of the Society of Powder Technology, Japan, 31(12), 4699-4713.

[10] Maxwell, J.C. (1890). In: Niven, W.D. (ed). Collected scientific papers. Cambridge University Press, Cambridge. http://strangebeautiful.com/other-texts/maxwell-scientific-papers-vol-1.pdf, http://strangebeautiful.com/other-texts/maxwell-scientific-papers-vol-2.pdf

[11] Picknett, R., & Bexon, R. (1977). The evaporation of sessile or pendant drops in still air. Journal of Colloid and Interface Science, 61(2), 336-350.

[12] Mezhericher, M., Levy, A., & Borde, I. (2007). Theoretical Drying Model of Single Droplets Containing Insoluble or Dissolved Solids. Drying Technology, 25(6), 1025–1032. https://doi.org/10.1080/07373930701394902

[13] Mortier, S. T. F. ., De Beer, T., Gernaey, K. V., Vercruysse, J., Fonteyne, M., Remon, J. P., Vervaet, C., & Nopens, I. (2012). Mechanistic modelling of the drying behaviour of single pharmaceutical granules. European Journal of Pharmaceutics and Biopharmaceutics, 80(3), 682–689. https://doi.org/10.1016/j.ejpb.2011.12.010

[14] Breinlinger, T., Hashibon, A., & Kraft, T. (2015). Simulation of the Spray Drying of Single Granules: The Correlation Between Microscopic Forces and Granule Morphology. Journal of the American Ceramic Society, 98(6), 1778-1786.

[15] Meerdink, G., & van't Riet, K. (1995). Modeling segregation of solute material during drying of liquid foods. AIChE Journal, 41(3), 732–736. https://doi.org/10.1002/aic.690410331

[16] Assar, M., Golmohammadi, M., Rajabi-Hamaneh, M., & Hassankiadeh, M. (2016). A Combined Experimental and Theoretical Approach to Study Temperature and Moisture Dynamic Characteristics of Intermittent Paddy Rice Drying. Chemical Engineering Communications, 203(9), 1242-1250.

[17] Guo, W., Lim, C., Bi, X., Sokhansanj, S., & Melin, S. (2013). Determination of effective thermal conductivity and specific heat capacity of wood pellets. Fuel (Guildford), 103, 347-355.

[18] Sacchetti, M. (2001). Thermodynamic analysis of DSC data for acetaminophen polymorphs. Journal of Thermal Analysis and Calorimetry, 63(2), 345-350.

[19] Krok, A., Vitorino, N., Zhang, J., Frade, J., & Wu, C. (2017). Thermal properties of compacted pharmaceutical excipients. International Journal of Pharmaceutics, 534(1-2), 119-127.

[20] Picker, K., & Hoag, S. (2002). Characterization of the thermal properties of microcrystalline cellulose by modulated temperature differential scanning calorimetry. Journal of Pharmaceutical Sciences, 91(2), 342-349.

[21] Alkahari, M. R., Abdul Aziz, M. S., Furumoto, T., Tanaka, R., Ueda, T., & Hosokawa, A. (2012). Thermal Conductivity of Metal Powder and Consolidated Material Fabricated via Selective Laser Melting. Key Engineering Materials, 523–524, 244–249.

[22] Andreotta, R., Ladani, L., & Brindley, W. (2017). Finite element simulation of laser additive melting and solidification of Inconel 718 with experimentally tested thermal properties. Finite Elements in Analysis and Design, 135, 36–43.

[23] Langecker, G. R., & Rautenbach, R. (1976). A method for measuring the thermal conductivity of isotropically compressed powders. Powder Technology, 15(1), 39–42.

[24] C. Li, C. Blocka, L. Zhang, Can. J. Chem. Eng. 2022, 1. https://doi.org/10.1002/cjce.24485

[25] Blackwell, J. (1954). A Transient-Flow Method for Determination of Thermal Constants of Insulating Materials in Bulk Part I—Theory. Journal of Applied Physics, 25(2), 137-144.

[26] Knight, J., Kluitenberg, G., Kamai, T., & Hopmans, J. (2012). Semianalytical solution for dual probe heat-pulse applications that accounts for probe radius and heat capacity. Vadose Zone Journal, 11(2), Vzj2011.0112.

[27] METER Group. (2018). TEMPOS Thermal Properties Analyzer: Manual. NE Hopkins Court Pullman, WA: METER Group.

[28] Abramowitz, M., & Stegun, Irene A. (1972). Handbook of mathematical functions with formulas, graphs, and mathematical tables. New York: Wiley.

[29] Callahan, J. C., Cleary, G. W., Elefant, M., Kaplan, G., Kensler, T., & Nash, R. A. (1982). Equilibrium Moisture Content of Pharmaceutical Excipients. Drug Development and Industrial Pharmacy, 8(3), 355–369. https://doi.org/10.3109/03639048209022105

[30] Listiohadi, Y., Hourigan, J., Sleigh, R., & Steele, R. (2008). Moisture sorption, compressibility and caking of lactose polymorphs. International Journal of Pharmaceutics, 359(1), 123-134.

[31] Stephan, K., & Laesecke, A. (1985). The Thermal Conductivity of Fluid Air. Journal of Physical and Chemical Reference Data, 14(1), 227-234.

[32] Ngabe, B., & Finch, J. (2014). Determination of specific heat capacity of sulphide materials at temperatures below 100°C in presence of moisture. Minerals Engineering, 58, 73-79.

[33] Pavlík, Z., Fiala, L., Vejmelková, E., & Černý, R. (2013). Application of Effective Media Theory for Determination of Thermal Properties of Hollow Bricks as a Function of Moisture Content. International Journal of Thermophysics, 34(5), 894-908.

Chapter 4 – Experimental Investigation of Dynamic Drying in Single Pharmaceutical Granules Containing Acetaminophen or Carbamazepine using Synchrotron X-ray Micro Computed Tomography

The contents of this chapter have been published in the International Journal of Pharmaceutics.

Contribution of the MSc Student

Conceptualization, writing of the original draft and reviewing, methodology, investigation, and visualization were performed by Carter Blocka. Xiao Fan Ding aided in the investigation and review of the writing. Dr. Lifeng Zhang provided supervision throughout the research, aiding in the conceptualization, writing review, project administration, and funding acquisition. Dr. Ning Zhu aided in the investigation and provided further review of the writing.

Contribution of the Chapter

In this chapter, a deeper understanding of the dynamic drying of single pharmaceutical granules is provided. Synchrotron X-ray imaging techniques were used for the visualization of the process. Pore volume evolution and moisture content changes were investigated for the first time at an experimental level. Modelling of thin-layer drying was developed to predict changes in the moisture content, with further modelling performed to predict changes to the porosity using linear regression. These findings provide valuable information to understand the drying process at a granular level and could be used in conjunction with those models proposed in Chapter 3 to optimize and improve more complex simulations of pharmaceutical drying.

4.1 Abstract

Drying time, velocity, and temperature are important aspects of the drying process for pharmaceutical granules observed during tablet manufacturing. However, the drying mechanism of single granules is often limited to modelling and simulation, with the internal and physical changes difficult to quantify at an experimental level. In this study, in-situ synchrotron-based X-ray imaging techniques were used for the first time to investigate the dynamic drying of single pharmaceutical granules, quantifying internal changes occurring over the drying time. Two commonly used excipients (lactose monohydrate (LMH) and microcrystalline cellulose (MCC)) were used as pure components and binary mixtures with one of either two active pharmaceutical

ingredients of differing hydrophilicity/hydrophobicity (acetaminophen (APAP) and carbamazepine (CBZ)). Water was used as a liquid binder to generate single granules of 25 % to 30 % moisture content. Results showed that for most samples, the drying time and composition significantly influences the pore volume evolution and the moisture ratio, with the velocity and temperature of the drying air possessing mixed significance on increasing the rate of pore connectivity and moisture removal depending on the sample composition. Effects of active ingredient loading resulted in minimal influence on the drying of CBZ and generated binary mixtures, with APAP and its respective mixtures' drying behaviour dominated by the material's hydrophilic nature.

4.2 Introduction

Within the pharmaceutical tableting process, the drying of wet granules by a convective method is an essential unit operation in the preparation of the product for the downstream process of compaction and packaging. The removal of moisture is used to extend a product's shelf life, decreasing the weight of the product while simultaneously ensuring stability [1,2]. For this application, fluidized bed drying is most commonly used, possessing a high level of mass and energy transfer that is observed between the drying gas and the individual granules [3,4]. The drying kinetics within the initial stages of drying are governed by aspects of velocity, temperature, and humidity, with Fick's law describing the rate of liquid diffusion as proportional to the concentration gradient with consideration to the water vapour concentration at the surface [5,6]. Following the initial period, the falling rate period introduces more complex moisture removal, with the liquid surface receding and affecting surface tension in the granule formation [7]. Additionally, the intergranular pore network further allows for liquid transport to the vapour-liquid interface at the granule surface, with evaporation permitting the removal of moisture [8-11].

Well documented within the literature, key factors of drying air velocity and temperature influence the drying process by shortening the drying time as these parameters increase in value [12,13-15]. However, certain materials such as acetaminophen found within the pharmaceutical industry are susceptible to degradation at elevated temperatures while moisture is present [16], limiting the conditions of the drying operation to maximize the drying rate while minimizing these undesirable effects. The addition of active pharmaceutical ingredients into mixtures may also affect the final granules' characteristics, with size, shape, and density observed as influential parameters

[17,18]. Furthermore, different types of pharmaceutical ingredients exhibit flowability challenges as mechanical properties change in the presence of moisture. While diluent and binder materials such as lactose monohydrate are observed to form a paste-like slurry at elevated moisture contents, active ingredients such as acetaminophen and carbamazepine form very hard solids, with other materials such as microcrystalline cellulose exhibiting mild yet loose clumping while still maintaining flowability due to the complex nature of water uptake [19,20]. The differences in these mechanical properties and each material change in the presence of moisture are consequently important in determining the final granules attributes, and by proxy, tableted products. This is further justified for some of the most common excipients in the tablet manufacturing process, such as microcrystalline cellulose, whose interactions with water are complicated due to particles swelling and shrinking during the wetting and drying processes respectively [21].

The moisture content changes observed in the drying process have previously been documented alongside changes observed in the pore volume as significant parameters on the thermal conductivity and volumetric specific heat capacity for common pharmaceutical components and mixtures [19]. These thermal properties are of particular importance for granular materials of high sphericity, as various mathematical drying models evaluate thermal properties within the equations of mass and heat transfer in spherical coordinates [8,22].

In investigating single granule materials and the drying operations surrounding them, limited research has been performed on an experimental level, with primary emphasis on the literature surrounding models and simulation [7-9,23]. Previous works by Groenewold et al. [24] aimed to determine single-particle drying kinetics using acoustic levitation for γ-Al_2O_3. Experiments were conducted between 25 °C and 30 °C with air velocity varied between 0.020 m/s and 0.088 m/s, measuring outlet humidity using a hygrometer. The findings of this work were comparable to results observed in a drying channel or a microbalance, with accurate derivations of drying curves feasible up to 0.065 m/s. This method presents an attractive experiment design that can be performed easily and quickly, with the entire surface area of the particles exposed to the drying air as intrusive support is not required. However, the particles are subject to the primary effects of acoustic streaming, producing a higher drying rate than expected by the boundary layer theory [25]. In addition to this, the particles tend to move around, making the positioning and tracking of the particles difficult. Another study by Janocha and Tsotsas [26] examined single

sessile droplets drying using a cuboid glass drying chamber with laminar flow. Experiments were conducted between 21 °C and 75 °C, with air velocity varied between 0.1 m/s and 1.5 m/s. The methodology of the experiment used X-ray micro-computed tomography to gain information on the inner structure of the samples during the drying process. The methods within this work present an attractive option for visualizing the drying process using X-ray micro-computed tomography, with the ease of use in positioning a single, stationary sample within a relatively simple apparatus that can be connected to an existing, preconditioned air stream. However, the samples must have the downside of being fixed to a substrate to eliminate motion artifacts during imaging [27], not allowing for the entire surface area of the sample to be exposed to the drying air.

While the studies of single granule drying are limited due to concerns of fast drying kinetics and instability during imaging brought upon by sample motion, several investigations using synchrotron X-ray micro-computed tomography have previously been conducted for pharmaceuticals on a dynamic scale. Lab-based micro-computed tomography is highly time-consuming for obtaining a high-resolution dataset, with dynamic studies not being feasible as imaging times can take up to a few hours within a limited field of view of the sample [28]. Due to lab-based limitations and the time required to obtain high-resolution data, it can be expected that any changes occurring within a sample during imaging can lead to multiple artifacts that can make analysis too involved or the data unusable [29,30]. Conversely, synchrotron-based X-ray imaging can overcome the challenges seen in conventional methods. Possessing a high flux with good stability, synchrotron X-ray micro-computed tomography can obtain high contrast results much faster than conventional methods, with single high-resolution scans taking a matter of seconds, in addition to much greater spatial and temporal resolutions [31].

Synchrotron imaging has been used to capture rapidly occurring processes, emphasizing the use of X-ray projections and micro-computed tomography. In works by Li et al. [17, 32], common pharmaceutical powders were quantitatively studied using a single droplet impact method to study the dynamic wet granulation process using synchrotron-based X-ray imaging techniques. These works found that the particle properties of size, sphericity, and hydrophilicity significantly influence the granulation process and the resulting granules, with the internal structure differences and porosity of each granule decreasing from the top of the granule to the bottom [17]. Furthermore, these studies demonstrated a high potential for applying synchrotron X-ray imaging

for studying dynamic processes, with further experiments drawing more information for single droplet studies that analyzed spreading and tunnelling mechanisms within pharmaceutical materials, better-describing water movement and penetration [32]. In works by Danalou et al. [31,33], synchrotron-based X-ray imaging techniques were once again applied, visualizing the real-time wetting process of pharmaceutical powder beds for various binary mixtures and liquid binders. These works found that for most compositions, an increase in porosity is observed for higher active pharmaceutical ingredient loading in the form of acetaminophen, with further results showing significant differences in agglomeration depending on the excipient used and the selected liquid binder [31]. Additionally, a single droplet impact method was implemented to evaluate the rate of pore evolution and distribution during the dynamic wetting process, further demonstrating the effectiveness and attractiveness of using synchrotron-based X-ray imaging methods for complex and fast processes that occur within opaque materials such as pharmaceuticals [33].

Therefore, the objectives of this study were (a) to investigate and compare the single granule drying behaviour of acetaminophen (APAP), microcrystalline cellulose (MCC), lactose monohydrate (LMH), and carbamazepine (CBZ) for pure components and binary mixtures under several drying air velocities and temperatures, and (b) to visualize and quantify the changes for single granules undergoing the drying process with the aid of synchrotron X-ray applications to characterize the 3D internal properties with emphasis on changes within the pore volume and changes in the moisture content of a sample. This work aimed to study the real-time single-granule drying dynamics for various individual pharmaceuticals and mixtures.

4.3 Theory and Modelling

The modelling of single particle and single granular drying are derived in spherical geometries for simplicity and convenience in numerical analysis, with results often comparable in accuracy to more complex geometries [34]. Equations of heat and mass transfer in a sphere can be represented by taking into consideration Fourier's law of heat conduction and Fick's law of diffusion respectively. These are presented by the following equations:

$$\frac{\partial X}{\partial t} = \frac{1}{r^2}\frac{\partial}{\partial r}\left(r^2 D_{eff}\frac{\partial X}{\partial r}\right) \tag{4.1}$$

$$\frac{\partial(\rho C_p T)}{\partial t} = \frac{1}{r^2}\frac{\partial}{\partial r}\left(r^2 k\frac{\partial(T)}{\partial r}\right) \tag{4.2}$$

where X is the moisture content of the granule; t is time; D_{eff} is the moisture diffusion coefficient; r is the radius of the granule; ρ is the granule density; C_p is the specific heat capacity; T is the temperature; k is the thermal conductivity.

In the drying model, with emphasis on the equation for heat transfer, the parameters of specific heat capacity and thermal conductivity can be seen. In previous works, these parameters have been determined to be significantly impacted by the moisture content and porosity of a given material [19], complicating the solutions to these equations as they must be solved simultaneously. These thermal properties can be predicted by the following correlations:

$$k = (A * (1 - X) + B * X)(1 - \varepsilon) + C * \varepsilon \quad (4.3)$$

$$\rho C_p = (D * (1 - X) + E * X)(1 - \varepsilon) + F * \varepsilon \quad (4.4)$$

where A, B, C, D, E, and F are curve fitting parameters; k is the thermal conductivity; ρC_p is the volumetric specific heat capacity; X is the moisture content of the sample; ε is porosity.

However, during the drying process, the removal of moisture and the evolution of pore volume changes can be observed throughout the process, giving way to a time dependency for the parameters of moisture content (X) and the contribution of air to the porosity (ε). These parameters are therefore important to monitor during the drying of singular granular media, as more refined modelling can be produced to better predict a material's drying endpoint.

In predicting moisture content changes for a given period, several popular models found within the literature can be used to predict the moisture ratio as a function of time such that all obtained results of a study are comparable [35, 36]. The moisture ratio can be described as:

$$MR = \frac{X - X_{eq}}{X_0 - X_{eq}} \quad (4.5)$$

where MR is the moisture ratio; X is the moisture content; X_0 is the initial moisture content; X_{eq} is the equilibrium moisture content. However, the equilibrium moisture content is often negligible [37,38], and a simplified approximation can be used in the form:

$$MR = \frac{X}{X_0} \quad (4.6)$$

where MR is the moisture ratio; X is the moisture content; X_0 is the initial moisture content.

While equations 4.1 and 4.2 are capable of providing a comprehensive understanding of coupled effects between different physical phenomena that may be overlooked by simpler models, the solutions to these are often complex and computationally expensive, with a larger time dedication required that may not meet the constraints of an industrial or research setting where time and resources are limited. More practically, thin-layer drying models are more accessible due to containing fewer parameters, being less resource-intensive while providing reasonably accurate predictions of the drying behaviour with less computational effort. These types of models can provide good approximations based on experimental data without the need for a full physical model of the drying process, allowing for a straightforward approach to develop a predictive model specific to the materials and drying conditions of interest, and have been observed to work well in conditions where uniform temperature and concentration assumptions are valid [35].

Collected experimental data can be fitted to thin-layer drying models (Table 4.1) used for the approximation of drying curves and moisture content by looking at the variation in the moisture ratio (*MR*) as a function of time (*t*). In this work, non-linear regression was performed using SPSS and OriginPro to predict coefficients by the least squares method. Each model can be compared for increased values of the coefficient of determination, R^2, and reducing the root mean square error, RMSE.

Table 4.1 - Thin-layer drying models applied for drying curve prediction.

Model number	Model name	Equation	Reference
1	Lewis	$MR = \exp(-k_0 t)$	[39]
2	Page	$MR = \exp(-k_0 t^n)$	[40]
3	Henderson and Pabis	$MR = a\exp(-k_0 t)$	[41]
4	Logarithmic	$MR = a\exp(-k_0 t) + c$	[42]
5	Two-term	$MR = a\exp(-k_1 t) + b\exp(-k_2 t)$	[43]

6	Two-term exponential	$MR = a\exp(-k_0 t) + (1 - a)\exp(-k_0 at)$	[44]
7	Wang and Singh	$MR = 1 + at + bt^2$	[45]
8	Midilli and Kucuk	$MR = a\exp(-k_0 t^n) + bt$	[46]
9	Hii et al.	$MR = a\exp(-k_0 t^n) + c\exp(- gt^n)$	[47]

Of the nine thin-layer drying models investigated, the Henderson and Pabis model was found to possess a relatively good agreement between experimental and predicted values with the smallest deviations and is considered the best thin-layer drying model for the moisture ratio of the single pharmaceutical granules used in this work. Due to the Henderson and Pabis model containing fewer parameters, the behaviour of the numerical convergence is more reliable with fewer sensitivities to initial conditions and bounds, being less prone to errors. Conversely, models such as the Midilli Kucuk model are more complex, possessing non-linear terms that introduce challenges in estimating the parameters, leading to numerical instability and convergence issues where optimization algorithms can struggle to find a stable solution. Further discussion on the thin-layer drying model results can be seen in section 4.5.2, with elaboration on the varying factors related to the drying process and the applicability of the models.

4.4 Materials and Methods

4.4.1 Materials

Four pharmaceutical powders were investigated in this study, with reverse osmosis water used as a liquid binder. Two common excipients were selected for comparison between drying behaviour and the effect of active pharmaceutical ingredient loading. Two active pharmaceutical ingredients were chosen to examine the effect of hydrophobicity on the drying. The physical characteristics of each pharmaceutical powder can be seen in Table 4.2. The model drugs of acetaminophen and carbamazepine were selected due to their diverse physical properties. Acetaminophen has been shown to be a relatively hydrophilic material with moderate stability, whose influence on the drying process is well-understood within the literature. Carbamazepine has been shown to be moderately hydrophobic, whose poor solubility profile serves to contrast the moderate solubility associated with acetaminophen. In addition, both acetaminophen and carbamazepine are widely used in clinical settings, relevant for studies that aim to optimize processes within the tableting industry, such as drying for commonly used medications.

The initial moisture content of individual samples and mixtures was brought to 30 % w/w, except for pure lactose monohydrate at 25 % w/w. The moisture content of each sample was measured using an HC103 Halogen Moisture Analyzer (METTLER TOLEDO, Canada). Granules of 3.29 ± 0.45 mm were used, similar to those sizes seen in a previous study [33]. Characterization of APAP, MCC, and LMH was previously performed by Danalou [31,33].

Table 4.2 - Properties of pharmaceutical powders.

Component	Abbreviation	Median particle size, d_{50} (μm) [31,33]	Particle skeletal density, ρ_p (g/cm^3) [31,33]	Supplier
Acetaminophen	APAP	50.9 ± 3.9	1.701 ± 0.001	Hebei Jiheng Pharmaceutical

Carbamazepine	CBZ	37.4 ± 12.5	1.381 ± 0.001	Sigma-Aldrich
Microcrystalline Cellulose	MCC	110.4 ± 6.6	1.555 ± 0.009	FMC BioPolymers
Lactose Monohydrate	LMH	47.9 ± 2.3	1.543 ± 0.004	Foremost Farms

The pharmaceutical powders used in this study are often abbreviated based on their composition. To clarify the naming and present the mass percentages of each powder, Table 4.3 presents the naming of each sample in addition to their composition and granule diameters.

Table 4.3 - Labeling of pharmaceutical powders used in this study.

Sample Name	Composition (mass percentage)	Wet Granule Projected Area Diameter (mm)	Dry Granule Projected Area Diameter (mm)	Change in Projected Area Diameter (mm)
APAP	100 % Acetaminophen	3.36 ± 0.33	3.36 ± 0.33	0.00 ± 0.00
CBZ	100 % Carbamazepine	3.48 ± 0.37	3.43 ± 0.34	0.05 ± 0.07
MCC	100 % Microcrystalline Cellulose	3.27 ± 0.34	3.11 ± 0.35	0.15 ± 0.02
LMH	100 % Lactose Monohydrate	3.23 ± 0.40	3.23 ± 0.40	0.00 ± 0.00
90MCC10APAP	90 % Microcrystalline Cellulose 10 % Acetaminophen	3.42 ± 0.27	3.25 ± 0.28	0.18 ± 0.07
80MCC20APAP	80 % Microcrystalline	3.23 ± 0.50	3.10 ± 0.49	0.12 ± 0.03

50MCC50APAP	Cellulose 20 % Acetaminophen 50 % Microcrystalline Cellulose 50 %	3.29 ± 0.13	3.27 ± 0.08	0.02 ± 0.09
90LMH10APAP	Acetaminophen 90 % Lactose Monohydrate 10 %	3.66 ± 0.20	3.66 ± 0.20	0.00 ± 0.00
80LMH20APAP	Acetaminophen 80 % Lactose Monohydrate 20 %	3.22 ± 0.15	3.22 ± 0.15	0.00 ± 0.00
50LMH50APAP	Acetaminophen 50 % Lactose Monohydrate 50 %	3.41 ± 0.33	3.41 ± 0.33	0.00 ± 0.00
50MCC50CBZ	Acetaminophen 50 % Microcrystalline Cellulose 50 % Carbamazepine	3.53 ± 0.35	3.45 ± 0.31	0.09 ± 0.06
50LMH50CBZ	50 % Lactose Monohydrate 50 % Carbamazepine	3.24 ± 0.15	3.24 ± 0.15	0.00 ± 0.00

4.4.2 Equipment

The pharmaceutical samples were positioned onto a custom-designed support made from 3D-printed polylactic acid (PLA) (Figure 4.1 b)). The design of the support is that of three cylinders at an offset angle, allowing for various morphological differences between granules to be permitted into the sample holder.

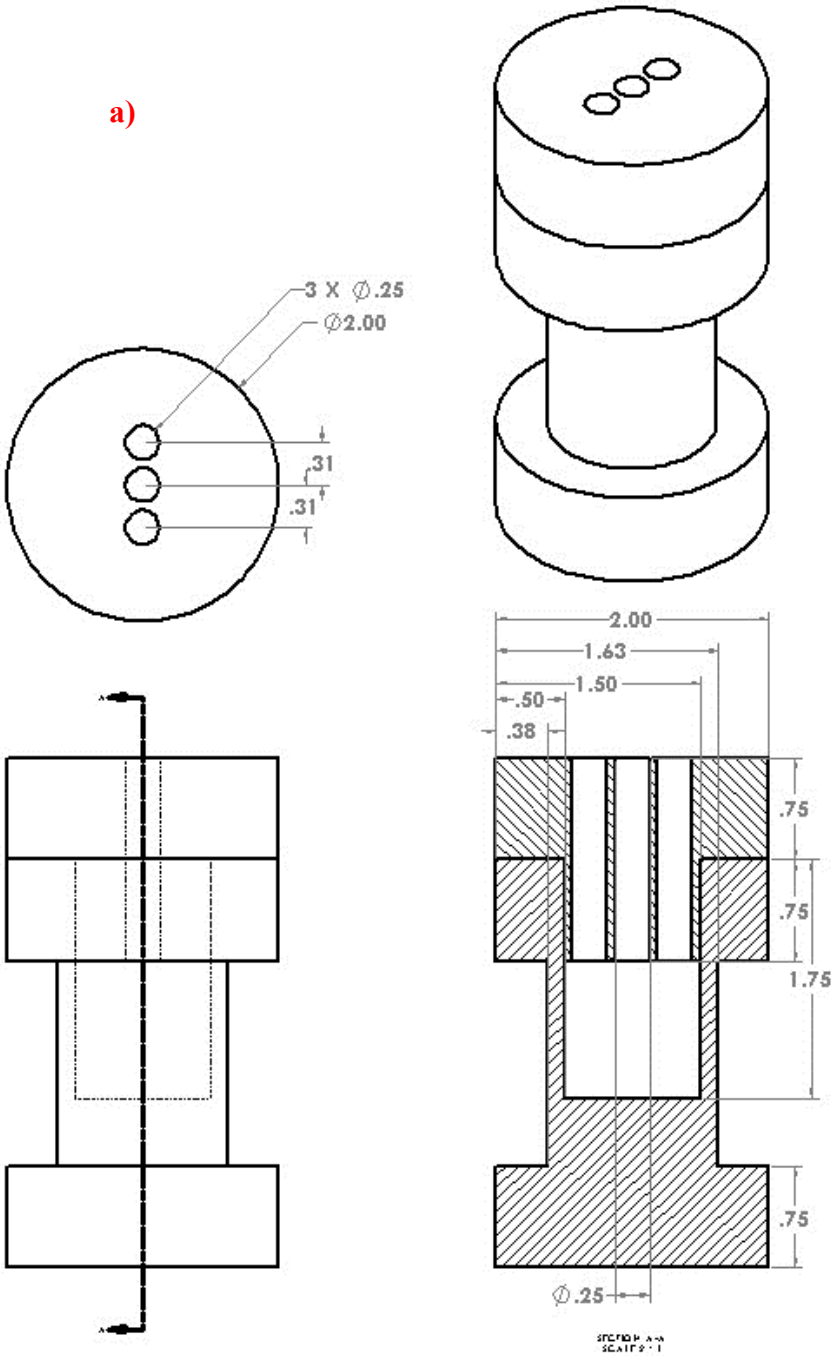

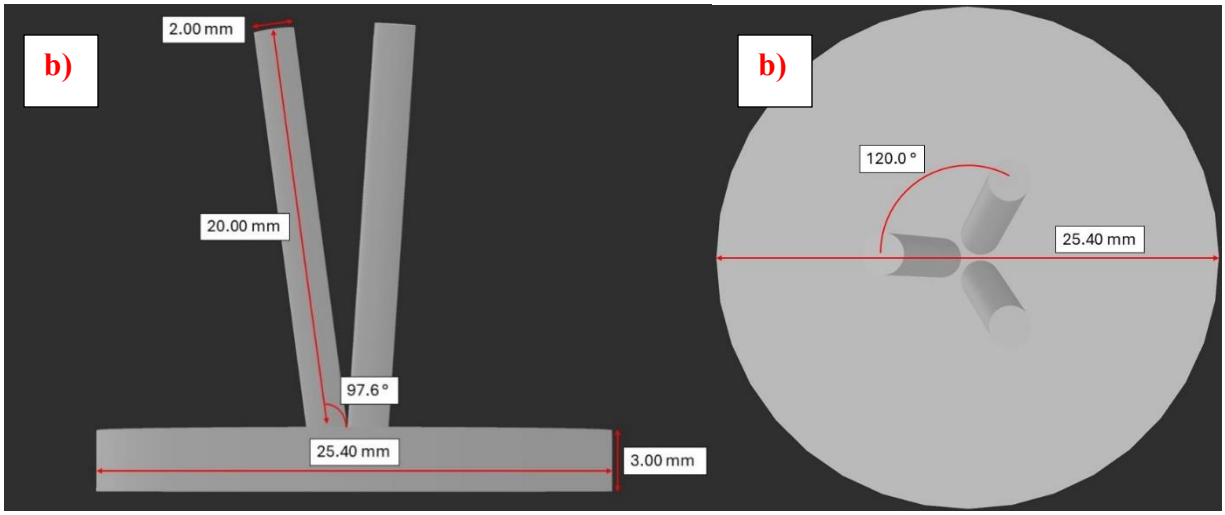

Figure 4.1 - a) Drawing of the PEEK Vessel used to contain individual granules and PLA support (dimensions in inches), b) Side and top-down view of 3D printed PLA support for single granules.

While methods of fluidization or acoustic levitation would be ideal in exposing the entirety of the samples to the drying air, the movement of the samples observed within these methods would lead to motion artifacts even with fast scan times of a matter of seconds at synchrotron facilities. Furthermore, it is expected that the positioning of the sample would be different between scans, making data analysis very difficult as certain regions of interest would be found in different locations if a scan were feasible with those methods. Therefore, support is necessary to attempt to expose the sample to the drying air as much as possible, while minimizing surface area that would be covered by a substrate.

The 3D-printed support is inserted into a polyetheretherketone (PEEK) vessel that is sealed by a lid and flange to allow the body of the vessel to rotate during scans. PEEK was selected as the construction material for the vessel due to its high durability and low x-ray absorption rate [48]. The PEEK vessel can be seen in Figure 4.1 a).

To monitor parameters of temperature and relative humidity, sensors are positioned at the inlet, outlet, and within the vessel, with measurements sent to an external data logging system to monitor parameters of temperature and relative humidity throughout the experiments.

Connected to the inlet of the PEEK vessel is an air pre-conditioning setup. Building air is fed into the setup at 100 psi and ambient temperatures (23 °C), proceeding through a heater that is connected to a PID controller, with a temperature probe positioned after a needle valve to

maintain the desired temperature. The air then proceeds through a flow meter to ensure the desired air flow rate going to the vessel and then travels through a length of flexible tubing that then connects to the PEEK vessel. The region after the needle valve is covered in a heated blanket to maintain temperature, and the entire main section is covered in insulation to reduce thermal losses. The flexible tubing is attached to a length of heat tape that is connected to its manual controller to further maintain temperature and is wrapped in insulating heat wrap. The length of tubing and the heating associated was to remain flexible as the piping had to be oriented in such a way that the connections to the PEEK vessel would stay outside of the region of the beam at the Canadian Light Source and still allowed for some rotation while connected to the CT rotation stage. A diagram of the entire setup can be seen in Figure 4.2.

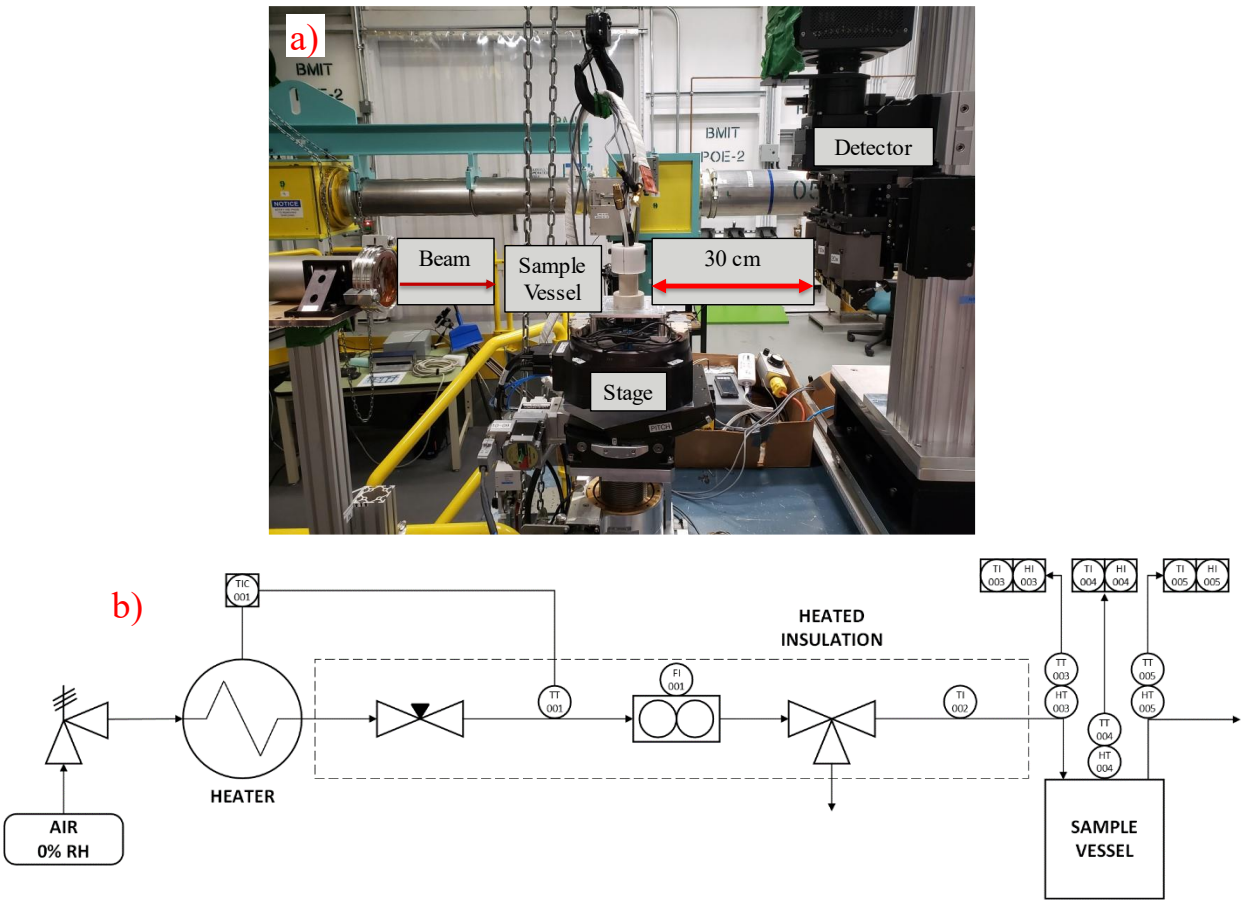

Figure 4.2 – a) In situ setup of single granule drying apparatus at 05B1-1 beamline, b) Process flow diagram of single granule drying apparatus.

Interval CT scans of *in situ* single granule drying were performed over the drying time at the 05B1-1 beamline of the Biomedical Imaging and Therapy Facility (BMIT) at the Canadian

Light Source (CLS). The X-ray source was a filtered white beam that was filtered through a 0.8 mm aluminum filter, with a peak photon energy of 20 keV at a current of 220 mA. X-ray projections were captured through an indirect detection optical system composing of an AA-40 beam monitor (Hamamatsu Photonics K.K., Japan) attached to a 500 μm-thick LuAG scintillator coupling with a PCO.DIMAX HS4 camera (PCO AG, Germany). It has an effective pixel size of 5.5 μm. Additional experiments were also conducted where projections were captured by an indirect detector with a Whitebeam microscope (Optique Peter) with 2X magnification and a 200 μm thick LuAG scintillator coupling with a PCO.DIMAX HS4 camera (PCO AG, Germany). It has an effective pixel size of 6 μm. A sample-to-detector distance of 30 cm was selected to improve absorption and edge enhancement of the obtained data while minimizing the effects of coherent diffraction, without the sample-to-detector distance becoming too short such that the Compton scattering photons would increase and result in deteriorated spatial resolution [49].

Each raw CT dataset consisted of 15 scans taken over 25 minutes, determined to be the drying endpoint for all samples where relative humidity measurements at the vessel outlet would no longer change. Each dataset included 20 dark-field images and 50 flat-field images for flat-field image correction. The data acquisition speed for each scan was 1500 projections per 180° rotation of the sample, with no delay between projections at an exposure time of 1 ms. These scanning parameters were determined to be the most optimal. Adjustments could be made to the exposure time, although an increase would result in a slower temporal resolution that would compromise capturing dynamic processes, or a shorter exposure time that would result in a poorer signal-to-noise ratio [50]. The field of view (FOV) for each projection was 8.14 mm × 3.56 mm.

4.4.3 Experimental Procedure

The moisture content, X, was measured for each sample before each experiment using an HC103 Halogen Moisture Analyzer.

Samples were first prepared by measuring out a small amount of the unwetted powders into small plastic containers, with binary mixtures measured by a mass ratio. The samples were generated in a larger quantity using a high sheer mixer, incorporating water to the desired moisture content over an extended period. For binary and wetted mixtures, the samples were mixed thoroughly for 5 minutes until a homogenous state was reached. The samples were then sieved through a 3.36 mm sieve, apart from pure LMH whose granules were formed by rolling a small

amount of paste into a spherical shape using a micro spatula. The moisture content of the samples was determined before each experiment, with reverse osmosis water added to the powders until the desired moisture content was achieved. Moisture content was determined using an HC103 Halogen Moisture Analyzer (METTLER TOLEDO, Canada). To allow for a uniform distribution within the bulk material, the wetted samples were allowed to rest for 15 minutes in an airtight container to reach equilibrium, similar to a previous study [19]. All samples were brought to 30 % moisture content, apart from pure LMH which was brought to 25 % moisture content as further increasing the addition of moisture would see the samples transform into a slurry. Samples were used immediately after preparation and were discarded if not currently in use. Each sample was disposed of at the end of each experiment. Multiple PLA supports were used such that previously used supports could be cleaned with reverse osmosis water and left to dry while at least one clean support could be used in the PEEK vessel. Single granules of approximately 3 mm in diameter (3.29 ± 0.45 mm observed from reconstructed CT data) that were spherical in nature were selected from the bulk and positioned on the PLA supports using a micro spatula before being inserted into the PEEK vessel and enclosed with the lid and flange. For each experiment, a single granule was used.

The PEEK vessel was screwed into the CT stage by an M4 screw, with the lid of the vessel connected to the air pre-conditioning setup adjacent to the stage. The length of flexible tubing and data acquisition cables were supported by an overhead crane to stay out of the way of the beam. Building air was connected to the system within the hutch, with manual valves used to vary the drying air velocity between 0.02 m/s and 0.10 m/s within the sample vessel as read by the flow meter. Heating elements were connected electrically to wall power and monitored by the individual controllers and the sensors connected to the PEEK vessel, with temperatures varying between 25 °C and 40 °C.

The drying air was permitted to reach steady state based on the output of the flow meter and the temperature sensors connected to the sample vessel and was maintained for five minutes before being redirected away from the sample vessel. The flanges fastening the lid of the vessel were removed to allow for a pre-prepared sample to be inserted with the tripod support, affixing the supports to the base of the vessel using double sided tape. The vessel was then reassembled

and an initial scan was taken of the sample before the drying air was directed to the sample vessel to begin the air drying process.

Scans were taken at intervals of 1 minute for the first 5 minutes, and then every 5 minutes until 25 minutes had elapsed. At the rate of 1500 projections per CT scan, it was not possible to perform interval scanning faster than one minute as there is a buffer time between scans because of the data being saved from the RAM. Data acquisition was then stopped, the hutch was opened, and the sample was removed with the PLA support from the PEEK vessel. The PEEK vessel was put back together with a new, clean PLA support to maintain temperature. The sample was discarded, and the PLA support was cleaned with reverse osmosis water and set aside to dry while an already clean support was substituted in its place. The system was then reset for another experiment.

With the obtained raw data, CT reconstruction with phase retrieval was performed using UFO-KIT-based software [51,52]. Dark and flat images were collected to spatially normalize the images where no sample was present. An example of the collected projections and the CT reconstruction process can be seen in Figure 4.3.

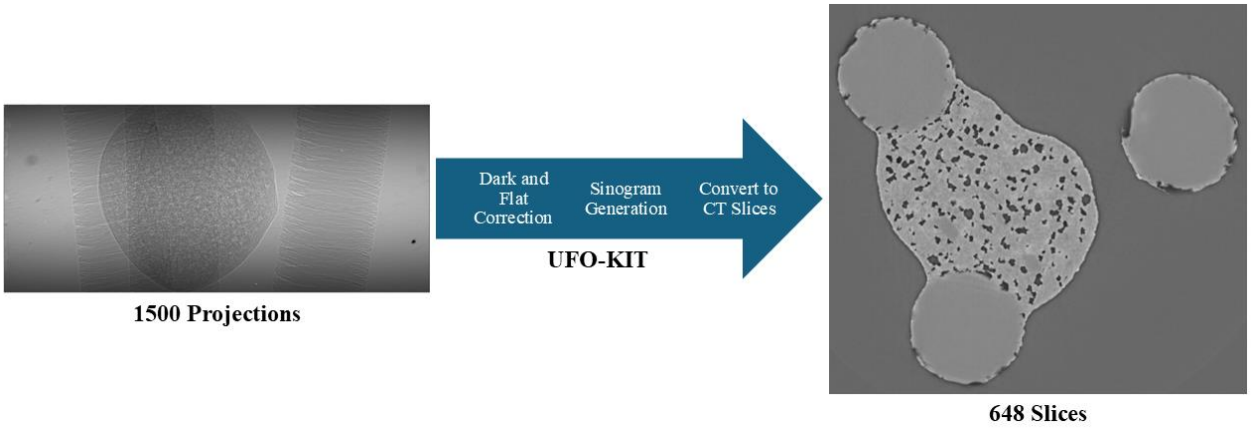

Figure 4.3 - Example of the CT reconstruction process using the collected X-ray projections for 80LMH20APAP sample.

Thresholding was performed using ImageJ (National Institutes of Health, USA) and Dragonfly version 2022.2.0.1367 (Objects Research Systems (ORS) Inc., Canada) was used for 3D rendering and to measure regions of interest within the scanned granules. Due to the varying densities found within a sample, highly attenuating regions will absorb more X-ray photons,

leading to lighter grey colours in the CT reconstructions [53]. A multistep segmentation method can then be used to separate the granule from the surrounding air and supports, similar to the methods used by Danalou et al. [33]. An example of the segmentation process can be seen in Figure 4.4.

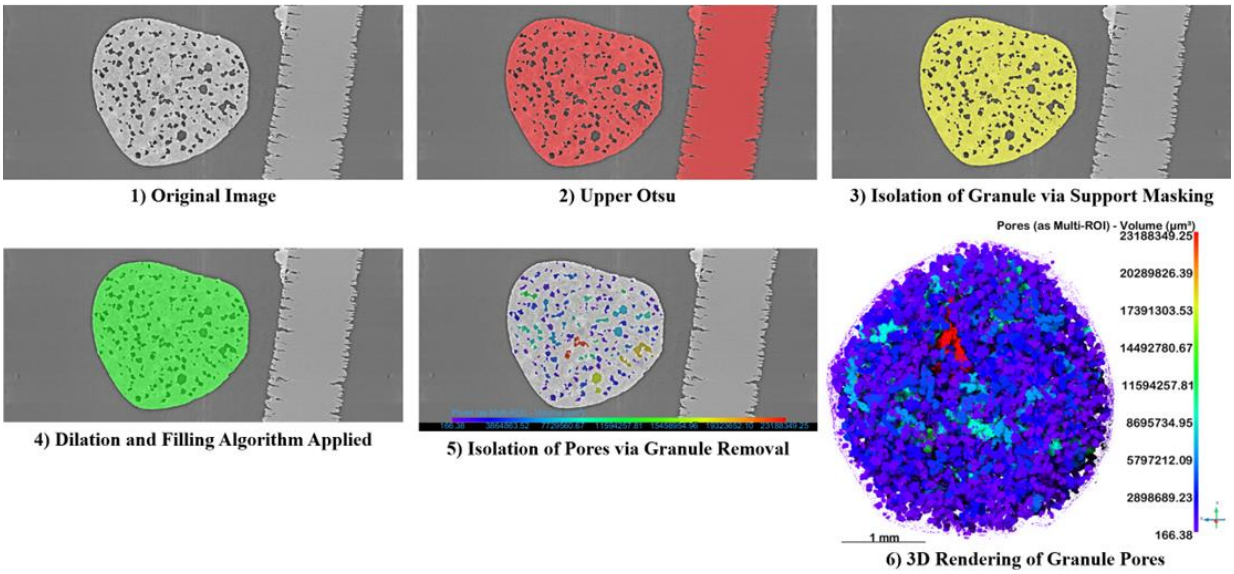

Figure 4.4 - Segmentation process and 3D rendering for the pore volume in an 80LMH/20APAP sample.

Firstly, the upper half of the grayscale histogram values can be separated by the upper Otsu method, with the granule further isolated by removing the supports by subtracting a mask from the region of interest (ROI). A dilation algorithm was then applied to a copy of the granule ROI to include all pores inside the granule, and the pores were then isolated by subtracting the granule ROI from the dilated copy. Lastly, 3D volume rendering was used, and histogram data of the regions of interest were extracted. Quantified data was imported into SPSS statistics 28 to determine significance using ANOVA testing, with OriginPro 2021b used for graph generation and nonlinear curve fitting with results from SPSS using the least squares method.

4.5 Results and Discussion

During the drying process, granules of pure components and mixtures were evaluated for internal structural changes within the pore volume, with further information gained through analysis of the grayscale histograms obtained for the entire region bounded by the granule's surface as seen in step 4 of Figure 4.4. To verify the results for air and water contents, the fractional results

within the volume of voids were brought into fraction forms for all samples and time points, with the underlying volume balance within the voids adding to unity. Pure components of APAP, MCC, LMH, and CBZ were investigated, with binary mixtures composed of 90 % to 50 % excipient by weight (MCC or LMH) with the remainder being an API (APAP or CBZ). Two common excipients were used to compare their nature of drying in addition to API loading, with the selected APIs used to compare the hydrophilic nature of APAP to the moderately hydrophobic nature of CBZ [54,55]. Initial moisture contents were measured at 30 % for all samples, apart from pure LMH which was limited to 25 % moisture content due to dissolution effects occurring at higher moisture contents. Ten interval scans were performed, with one scan taken every minute from 0 to 5 minutes, with the remaining scans taken at 5-minute intervals. The aim in the selection of these intervals was to capture the initial stages of drying as rapidly as possible with the given 1500 projections, with changes observed after the first 5 minutes being relatively constant.

4.5.1 Pore Volume

To better understand the internal changes and map pore size distribution, 3D volume rendering was applied to the segmented data. A time series example of this can be seen in Figure 4.5, with the respective time series data shown in Figure 4.6.

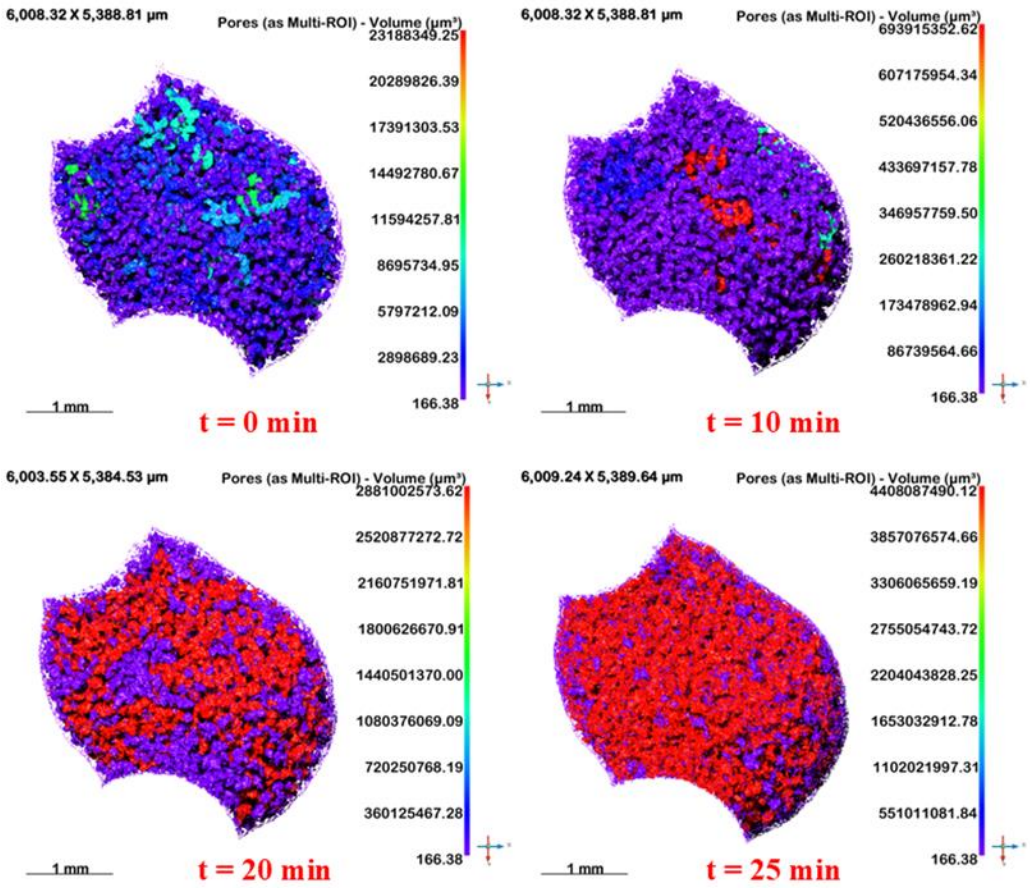

Figure 4.5 - 3D Rendering of the pore volume changes over a 25 minute drying time for an 80LMH/20APAP sample at 0.10 m/s and 25 °C.

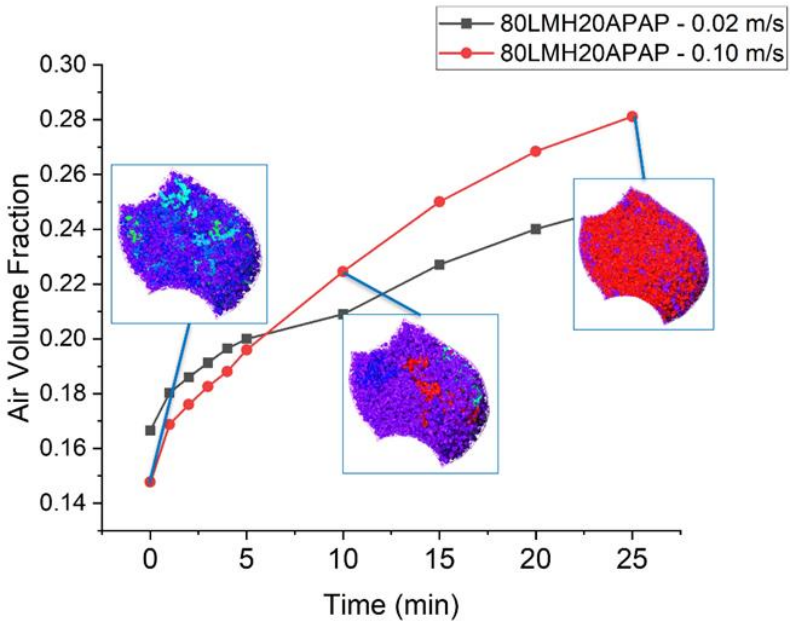

Figure 4.6 - Quantified changes to the pore volume for 80LMH20APAP at 0.02 m/s and 0.10 m/s at 25 °C.

As can be seen in Figure 4.5, the initial granules have a uniform pore distribution, with many small pores isolated within all parts of the granule. As drying is introduced, the individual pores begin to shrink and connect into a much larger pore network, with connectivity occurring from the outermost regions of the granule, with connections forming from the edge to the center. This is consistent with the drying mechanism of porous materials, with pockets of air observing an affine shrinkage as adjacent pores lose moisture and begin to merge with one another, resulting in the formation of a larger, interconnected void space [56,57]. The air evolution within the pore volume of the granules is quite uniform from the quantified results, as seen in Figure 4.4, with a gradual increase observed for all samples, not observing any sharp changes with an increase in the drying time.

Within the first 5 to 10 minutes, this pore network development can be observed, generating large, interconnected pockets of air within the granules. This connective behaviour continues until most of the pores create a singular pore network of up to 38 % of the granule's volume, with further drying allowing for additional smaller pores surrounding the single larger network to become connected.

For materials such as APAP that are noted to be hydrophilic, the generation of the fully developed pore network is observed to be very slow under mild drying conditions, with little pore growth and connection occurring beyond a relatively sharper initial increase. With an increase in the gas velocity and temperature, this change in the pore network becomes much more apparent, with larger amounts of air found within the pore volume at the end of drying. The changes to the air volume fraction for APAP can be seen in Figure 4.7. As hydrophilic materials exhibit an affinity for water, the distribution of water within the material is likely to be more uniform, resulting in an existing pore network with minimal closed pores as moisture evaporation is permitted. Comparatively, CBZ, which is shown to be moderately hydrophobic, maintains moderate pore network growth at both mild and elevated drying conditions, as illustrated in Figure 4.8. As hydrophobic materials resist wetting, larger initial pores may be exhibited and result in larger void spaces within the material as the drying process proceeds, with a greater contribution of air to the pore volume as moisture is removed.

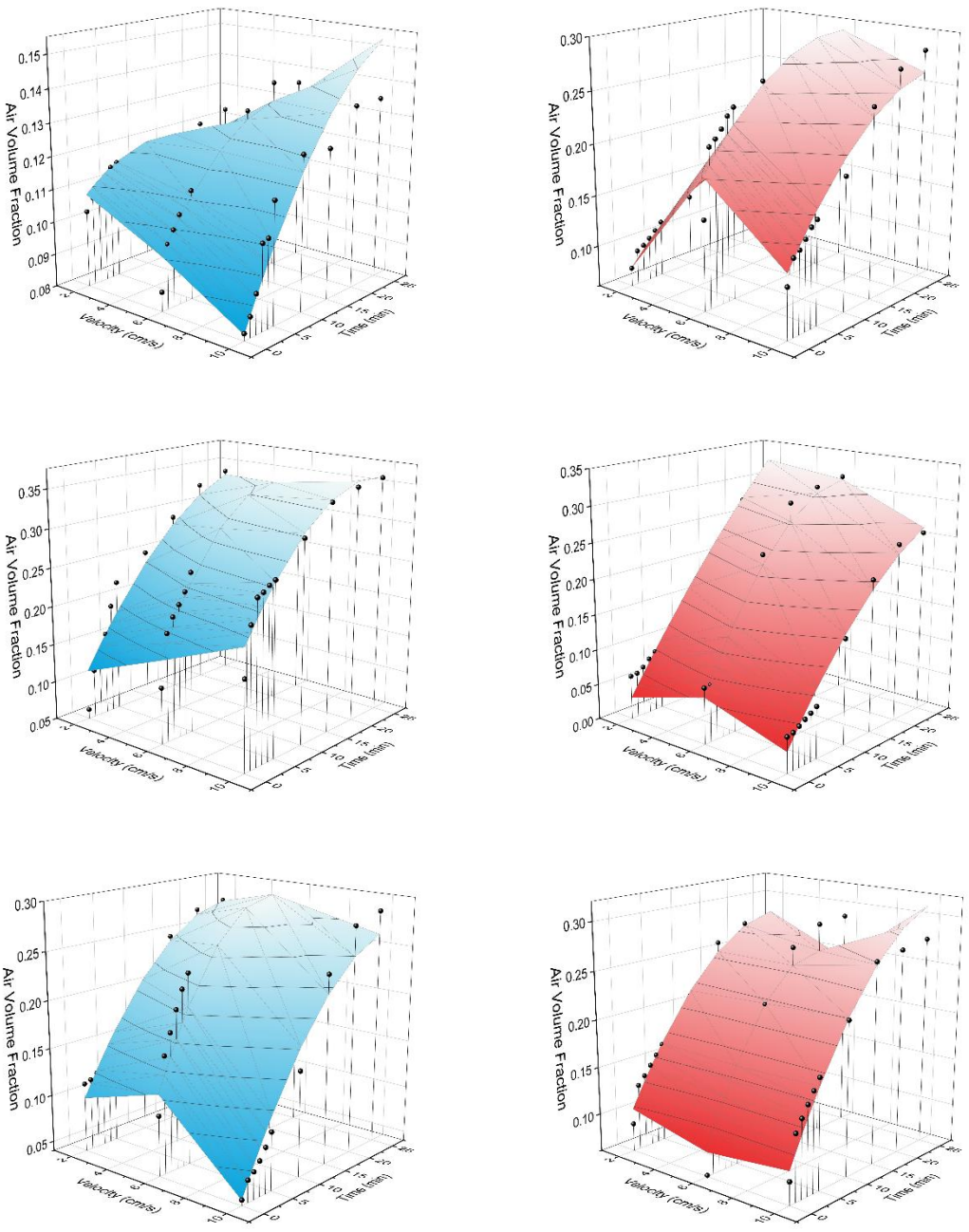

Figure 4.7 - APAP, MCC, and LMH data points and fitted surfaces for the air volume changes observed during the drying process for increasing velocity and increasing temperature (25 °C in blue, 40 °C in red). (Top left: APAP - 25 °C, Top right: APAP - 40 °C, Middle left: MCC - 25 °C, Middle right: MCC – 40 °C, Bottom left, LMH – 25 °C, Bottom right: LMH - 40 °C).

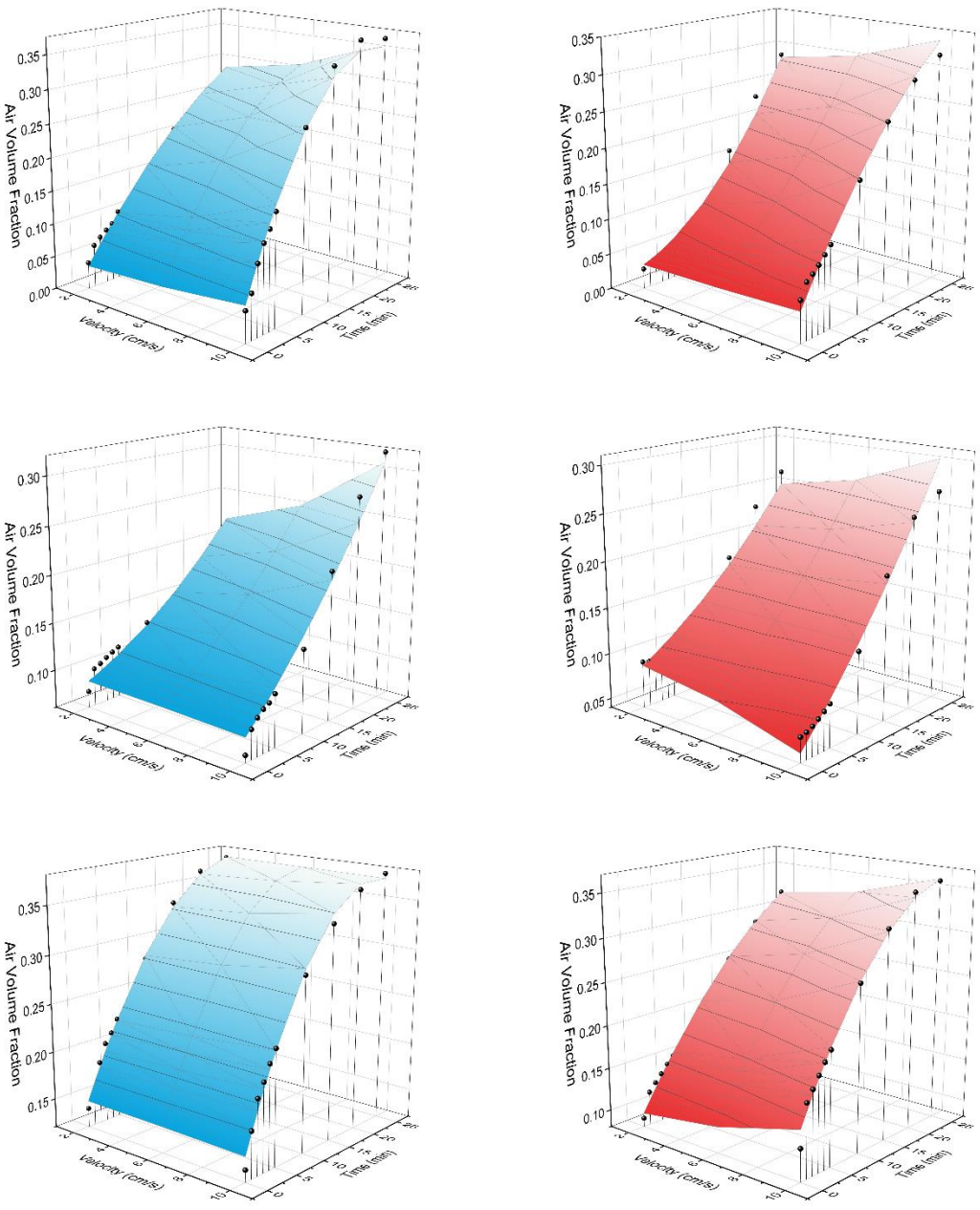

Figure 4.8 - CBZ, 50MCC50CBZ, and 50LMH50CBZ data points and fitted surfaces for the air volume changes observed during the drying process for increasing velocity and increasing temperature (25 °C in blue, 40 °C in red). (Top left: CBZ - 25 °C, Top right: CBZ - 40 °C, Middle left: 50MCC50CBZ - 25 °C, Middle right: 50MCC50CBZ – 40 °C, Bottom left, 50LMH50CBZ – 25 °C, Bottom right: 50LMH50CBZ - 40 °C)..

Comparing the excipients' drying behaviour, both MCC and LMH see a similar drying pattern, with steady changes to the pore network in Figure 4.7 similar to that shown in Figure 4.5. However, granules containing MCC have been observed to shrink during the drying process,

decreasing by up to 25.2 % in volume. Compared to the other pharmaceutical materials tested, this shrinking behaviour is not observed for APAP, LMH, or CBZ, with this change only observed in pure MCC, binary mixtures of MCC/APAP with higher MCC loadings, and mixtures with CBZ. The shrinkage of the MCC granules has been observed to be a complex process influenced by the trapping of water in fine capillaries and internal pores, with methods such as hot air over-drying being considered slower in terms of a water removal mechanism than methods such as freeze-drying, allowing for the solid material to shrink by capillary forces resulting from the high surface tension of water [58].

The effect of API loading on the development of the air volume fraction within the pore network can be seen in Figures 4.8-4.10. With an increase of APAP loading on both excipients, the coalescence of the pores shifts toward the drying behaviour of pure APAP, with this effect predominant in binary samples where LMH is the excipient. As LMH tends to be freely soluble in the presence of moisture, the dominant hydrophilic effects of APAP are expected to be more influential in the development of the pore structure, whereas MCC is insoluble in water, allowing for the material properties to contribute to the solid fraction within the granule. Conversely, the binary mixtures with CBZ and the excipients were not observed to be significantly influenced by API loading as CBZ is moderately hydrophobic in nature, with the evolution of the air volume fraction comparable to the pure components.

A summary of the changes observed within the pore volume can be seen from the ANOVA results depicted in Table 4.4. All samples tested were included, with parameters of temperature, velocity, and time tested for each sample set. It should be noted that the results were also tested for sample composition across all samples, with the results finding significant influence from the sample composition on the pore volume changes with a p-value <0.001 (significance <0.05).

Table 4.4 - ANOVA results for the significance of investigated variables on the pore volume.

Material	Drying time significance	Drying air velocity significance	Drying air temperature significance
APAP	0.206	0.003	<0.001
MCC	<0.001	0.419	<0.001
LMH	<0.001	0.468	0.755
90MCC10APAP	<0.001	0.112	<0.001
80MCC20APAP	<0.001	0.492	0.498
50MCC50APAP	<0.001	0.957	0.001
90LMH10APAP	<0.001	0.788	0.016
80LMH20APAP	<0.001	0.031	0.483
50LMH50APAP	<0.001	0.095	0.281
CBZ	<0.001	0.049	0.249
50MCC50CBZ	<0.001	0.618	0.738
50LMH50CBZ	<0.001	0.262	0.121

Of the changes observed within the pore volume, it is most notable that a significant change in the air fraction occurs for all samples throughout the drying time as expected. For all samples, apart from APAP at 25 °C, an increase in the air fraction within the pore volume was observed. These changes were quantified, with the initial air volume fraction being as low as 0.02 and increasing to as much as 0.38 throughout the drying process. Pure APAP samples and higher loadings of APAP observe changes in the air volume fraction between 0.02 and 0.31, with increasing gas velocity and temperature increasing the change in the air volume within the samples. All samples containing CBZ are observed to have changes in the air volume fraction between 0.03 and 0.38, with very little variance between samples dried at different drying gas velocities and temperatures. Excipient samples of MCC have an air volume fraction increase from 0.02 up to 0.36, and LMH samples change from 0.05 up to 0.31. Effects of drying gas velocity and temperature were found to be of mixed significance depending on the composition and API loading for both excipients.

With increasing the gas velocity, significant changes were found for both pure API's in addition to 80LMH20APAP. For APAP, the hydrophilic nature of the material requires elevated drying conditions to better liberate any bound water, opening the pore network to allow air to occupy the volume. With CBZ already being moderately hydrophobic, the water within the

samples does not require much energy input for evaporation to occur, with the increase in velocity removing the moisture at an increased rate as expected, thus increasing the air volume changes within the pore network. While the pore network of pure LMH was not found to be significantly impacted by increasing velocity, increasing velocity was found to be significant at moderate APAP loadings within the binary mixtures. This is likely due to a region between pure LMH and pure APAP loadings, where the drying does not become too dominated by either material's inherent properties, and the changes in the pore volume are permitted with increasing velocity affecting the removal of moisture and increase in air volume within the pore volume. Additionally, the soluble nature of LMH allows for APAP to present itself more dominantly within the solid fraction of the granules. The remaining granules' pore volume changes were not found to be significantly influenced by an increase in the drying air velocity.

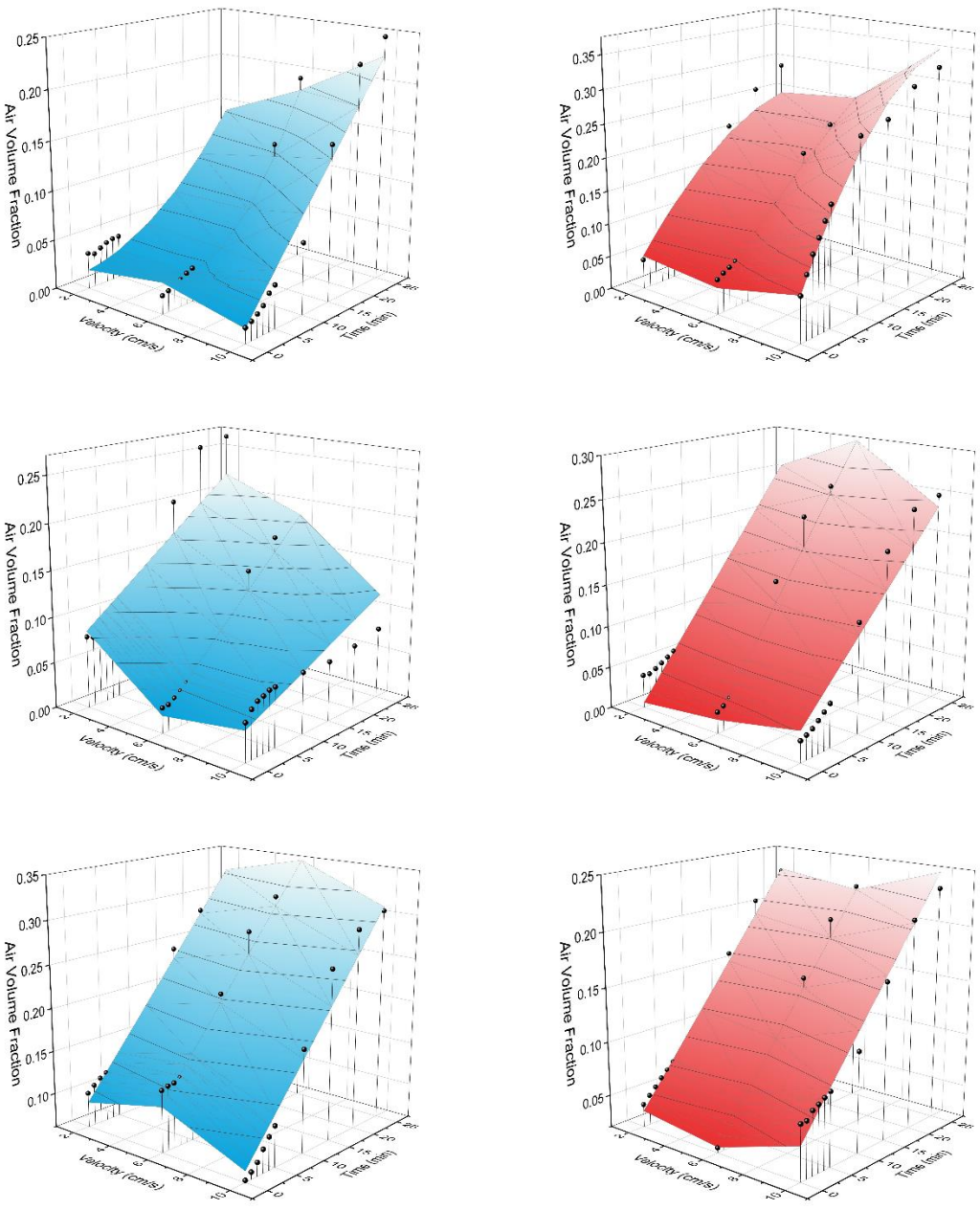

Figure 4.9 - 90MCC10APAP, 80MCC20APAP, and 50MCC50APAP data points and fitted surfaces for the air volume changes observed during the drying process for increasing velocity and increasing temperature (25 °C in blue, 40 °C in red). (Top left: 90MCC10APAP - 25 °C, Top right: 90MCC10APAP - 40 °C, Middle left: 80MCC20APAP - 25 °C, Middle right: 80MCC20APAP – 40 °C, Bottom left, 50MCC50APAP – 25 °C, Bottom right: 50MCC50APAP - 40 °C).

The effect of temperature on the pore volume changes was found to have mixed significance depending on the material. Both pure APAP and MCC were found to be

significantly influenced by an increase in temperature, with 90MCC10APAP, 50MCC50APAP, and 90LMH10APAP also observing this change. Similar to the changes to APAP observed with increasing velocity, an increase in drying air temperature promotes evaporation, better allowing the material to be liberated of moisture due to the increased energy. For MCC, the sloped regions following the initial stages of drying can be seen to be much steeper with an increase in drying air temperature, again resulting in the promotion of evaporative forces and the displacement of moisture within the granules with air. For the binary mixtures, the compositions of MCC/APAP are within regions close to either pure APAP or pure MCC, with similar phenomena expected similarly to that behaviour observed in the pure components. For the 90LMH10APAP samples, the effects of the pure components are not dominated by one or the other at this composition, allowing for temperature changes to significantly affect the changes to the pore volume. The remaining samples' pore volume changes were not found to be significantly influenced by an increase in the drying air temperature.

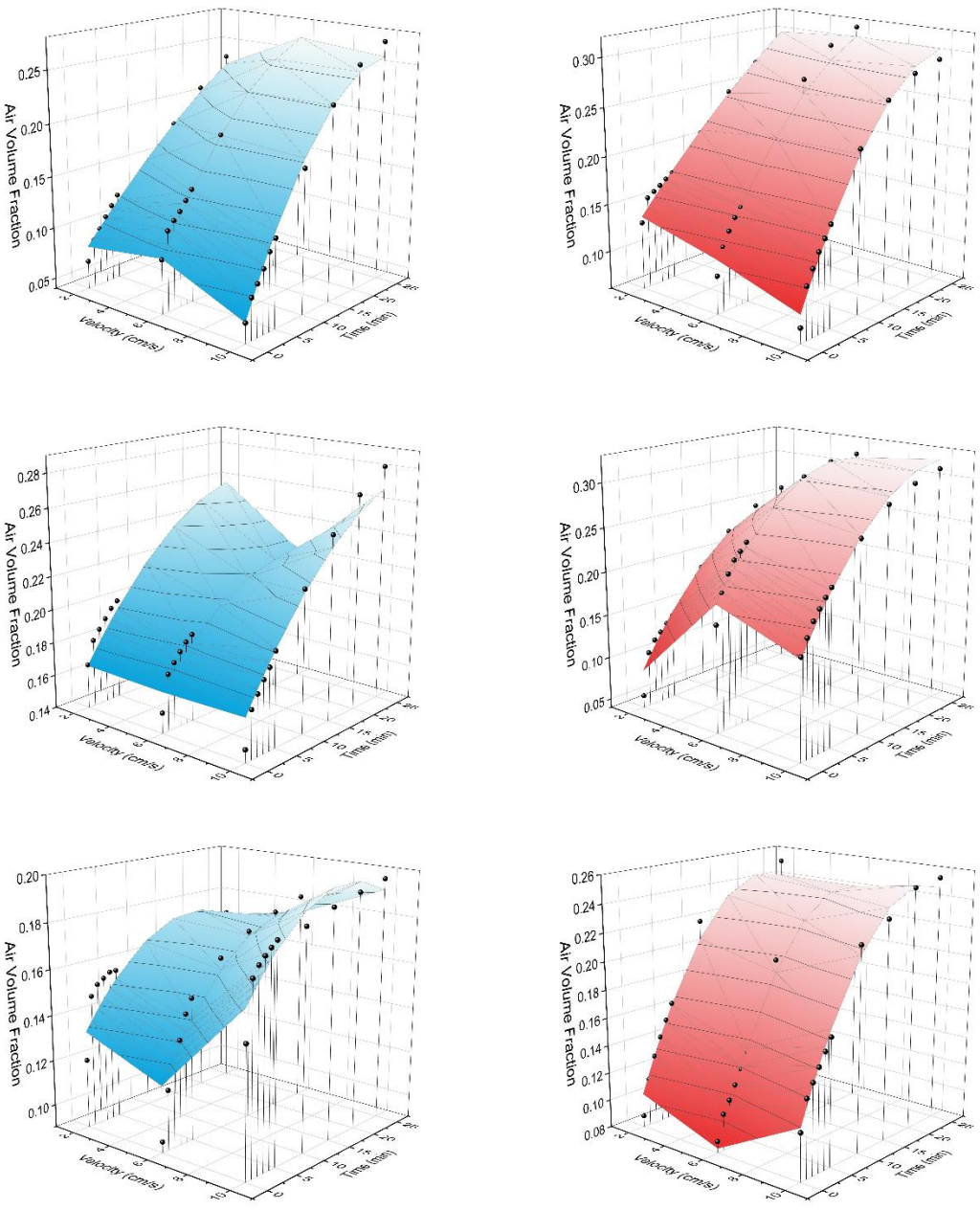

Figure 4.10 - 90LMH10APAP, 80LMH20APAP, and 50LMH50APAP data points and fitted surfaces for the air volume changes observed during the drying process for increasing velocity and increasing temperature (25 °C in blue, 40 °C in red). (Top left: 90LMH10APAP - 25 °C, Top right: 90LMH10APAP - 40 °C, Middle left: 80LMH20APAP - 25 °C, Middle right: 80LMH20APAP – 40 °C, Bottom left, 50LMH50APAP – 25 °C, Bottom right: 50LMH50APAP - 40 °C).

In comparing the differences between APIs and the drying behaviour observed, the effect of hydrophilicity and hydrophobicity can be discussed. Comparing results for 25 °C experiments,

APAP does not produce much change within the pore volume due to the material's hydrophilic nature, maintaining a low pore volume fraction in the region of 0.11, while CBZ can change from 0.03 to 0.37. Introducing temperature changes, CBZ still follows a similar trend, while APAP is now capable of changing up to a pore volume fraction of 0.28. This again demonstrates the expected moisture liberation of hydrophilic materials, with the increase in energy better allowing for moisture removal through evaporation, with this removal being replaced with the surrounding air in a more efficient removal as hydrophilic materials maintain a more prevalent and interconnected pore structure [59]. With the addition of excipients, CBZ maintains its drying behaviour, having minimal effects on the drying behaviour of the excipients, while APAP exhibits more of a dominance on the drying pattern of the excipients, trending closer to the drying behaviour of pure APAP at higher API loadings. Within the individual pore volumes, as the water evaporates during the hot air drying process, the pore structure and stability for each API is are susceptible to collapse and deformation as the drying rate increases resulting from an increase in the drying gas velocity and temperature. APAP was observed to dry out much more rapidly with increasing the drying conditions, as indicated by the overall changes to the total pore volume as seen in Figure 4.7. Furthermore, the time series CT reconstructions revealed moderate pore collapsing within the increased conditions, with individual micro-pores increasing the connectivity between macro-pores as they expand into one another before deforming. In contrast, the drying of CBZ was not observed to encounter structural issues, as the lack of strong water interaction allows for the moisture to be removed freely as seen between all conditions in Figure 4.8, with pore collapse not observed in the time series CT reconstructions.

To predict the changes in the pore volume, a linear regression fitting can be used with the individual and interactive terms of time, temperature, and velocity, as seen in the surfaces for the air volume changes. For this, a linear regression was performed with backward elimination to obtain significant parameters. In modelling the fit of these parameters, it was observed that temperature did not play a significant role without the inclusion of squared terms, with the effects of time and velocity having mixed significance depending on the material. A summary of the linear regression model can be seen in Tables 4.5-4.8.

Table 4.5 - Linear regression results for pure components pore volume evolution.

Parameter	APAP	Std. Error	MCC	Std. Error	LMH	Std. Error
(constant)	0.212	0.0154	0.163	0.012	-0.009	0.028
u	-0.049	0.006			0.063	0.012
t	-0.002	5.57E-04	0.008	0.001	0.009	0.001
T^2	-1.58E-04	1.26E-05	-1.10E-04	1.32E-05	8.48E-05	2.15E-05
u^2	0.003	4.91E-04	0.002	1.83E-04	-0.006	9.74E-04
t^2						
ut	3.56E-04	5.51E-05	0.004	8.52E-04	0.003	9.34E-04
uT^2	7.47E-05	4.94E-06	1.66E-05	4.58E-06	-4.70E-05	8.81E-06
ut^2			-1.82E-04	3.17E-05	-1.53E-04	3.25E-05
tT^2	5.76E-06	6.78E-07				
tu^2			-3.11E-04	8.75E-05	-2.16E-04	9.63E-05
T^2u^2	-5.48E-06	4.04E-07	-2.35E-06	3.90E-07	4.35E-06	7.21E-07
T^2t^2	-1.17E-07	2.38E-08	1.29E-07	2.48E-08		
u^2t^2			1.42E-05	3.43E-06	1.26E-05	3.62E-06
R^2	0.966		0.969		0.934	
RMSE	0.012		0.019		0.021	

Table 4.6 - Linear regression results for MCC binaries pore volume evolution.

Parameter	90MCC10 APAP	Std. Error	80MCC20 APAP	Std. Error	50MCC50 APAP	Std. Error
(constant)	-0.043	0.026	0.241	0.032	0.054	0.008
u	0.026	0.011	-0.060	0.013	0.043	0.004
t					0.010	5.40E-04
T^2	7.14E-05	2.16E-05	-1.48E-04	2.69E-05		
u^2	-0.002	9.18E-04	0.004	0.001	-0.004	4.00E-04
t^2	1.33E-04	5.62E-05				
ut	-0.004	0.001	0.002	3.82E-04		
uT^2	-2.40E-05	8.33E-06	3.78E-05	1.07E-05	-3.42E-05	2.77E-06
ut^2	1.64E-04	5.02E-05				
tT^2	1.26E-05	2.14E-06	4.72E-06	6.95E-07	-1.63E-06	4.42E-07
tu^2	4.35E-04	1.08E-04	-1.48E-04	3.51E-05		
T^2u^2	2.24E-06	6.82E-07	-2.26E-06	8.78E-07	3.21E-06	2.85E-07
T^2t^2	-3.88E-07	8.77E-08				
u^2t^2	-1.54E-05	4.55E-06				
R^2	0.960		0.900		0.973	
RMSE	0.019		0.025		0.014	

Table 4.7 - Linear regression results for LMH binaries pore volume evolution.

Parameter	90LMH10 APAP	Std. Error	80LMH20 APAP	Std. Error	50LMH50 APAP	Std. Error
(constant)	0.004	0.011	0.286	0.013	0.176	0.008
u	0.025	0.004	-0.040	0.005	-0.016	0.003
t	0.005	3.94E-04	0.004	6.76E-04	-0.002	5.90E-04
T^2	8.78E-05	8.83E-06	-1.90E-04	1.03E-05	-2.53E-05	5.21E-06
u^2	-0.002	3.48E-04	0.003	4.37E-04	0.002	2.03E-04
ut	0.001	8.15E-05	-0.00114	2.40E-04	6.72E-04	2.09E-04
uT^2	-1.79E-05	3.50E-06	6.19E-05	4.06E-06	-1.93E-06	6.70E-07
ut^2	-3.14E-05	3.00E-06				
tT^2	6.77E-07	2.61E-07	7.00E-06	5.57E-07	9.00E-06	4.87E-07
tu^2			9.95E-05	1.96E-05	-5.82E-05	1.71E-05
T^2u^2	1.22E-06	2.86E-07	-4.43E-06	3.32E-07		
T^2t^2			-1.69E-07	1.96E-08	-1.96E-07	1.71E-08
R^2	0.988		0.974		0.968	
RMSE	0.008		0.009		0.008	

Table 4.8 - Linear regression results for CBZ samples pore volume evolution.

Parameter	CBZ	Std. Error	50MCC50CBZ	Std. Error	50LMH50CBZ	Std. Error
(constant)	0.034	0.005	0.089	0.005	0.182	0.007
t	0.021	0.002	0.002	0.001	0.019	0.002
T^2					-5.48E-05	5.38E-06
u^2	2.78E-04	1.07E-04	1.96E-04	9.80E-05	-3.17E-04	7.45E-05
t^2	-4.22E-04	8.77E-05	9.21E-05	3.95E-05	-4.02E-04	6.40E-05
tT^2	-1.13E-05	1.39E-06	1.19E-06	4.13E-07	-4.02E-06	1.19E-06
tu^2	1.41E-04	1.88E-05	3.77E-05	5.12E-06	3.80E-05	1.21E-05
T^2u^2	-1.18E-07	6.95E-08	-3.62E-07	6.92E-08	4.69E-07	5.17E-08
T^2t^2	4.45E-07	6.22E-08			1.55E-07	4.83E-08
u^2t^2	-4.84E-06	7.62E-07			-1.50E-06	4.91E-07
R^2	0.990		0.970		0.994	
RMSE	0.012		0.013		0.008	

To examine the reproducibility of the experiments, three replicates each of LMH at 0.10 m/s at 25 °C and 40 °C were processed respectively. The results for the air volume fraction changes can be seen in Figure 4.11.

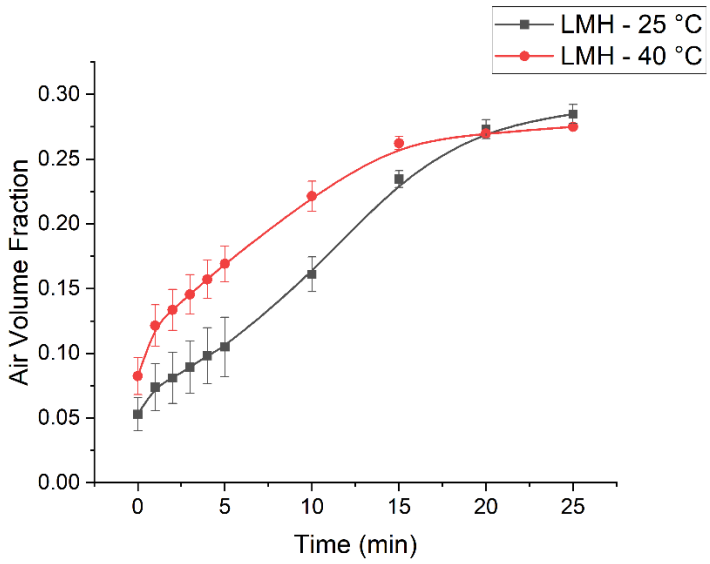

Figure 4.11 - Quantified changes to the pore volume for LMH replicates at 25 °C and 40 °C at 0.10 m/s to determine repeatability.

Similar to those results seen in Figure 4.7, the air volume fraction within the pores of the granules increases for both temperatures as drying continues, with the effect of temperature accelerating this change. The curves are consistent with those results seen in Figure 4.7, with acceptable deviations observed between the error bars and data points seen in Figure 4.11 and the data points seen in Figure 4.7.

4.5.2 Moisture Ratio

Alongside the 3D volume rendering, grayscale histograms were obtained for each time point during granule drying, covering the range of the entire granule and its pores. Contributions to the grayscale histograms include various attenuations from the air fraction within the pores, the moisture within the granule, and the solids of pharmaceutical materials. An example of these histograms can be seen in Figure 4.12.

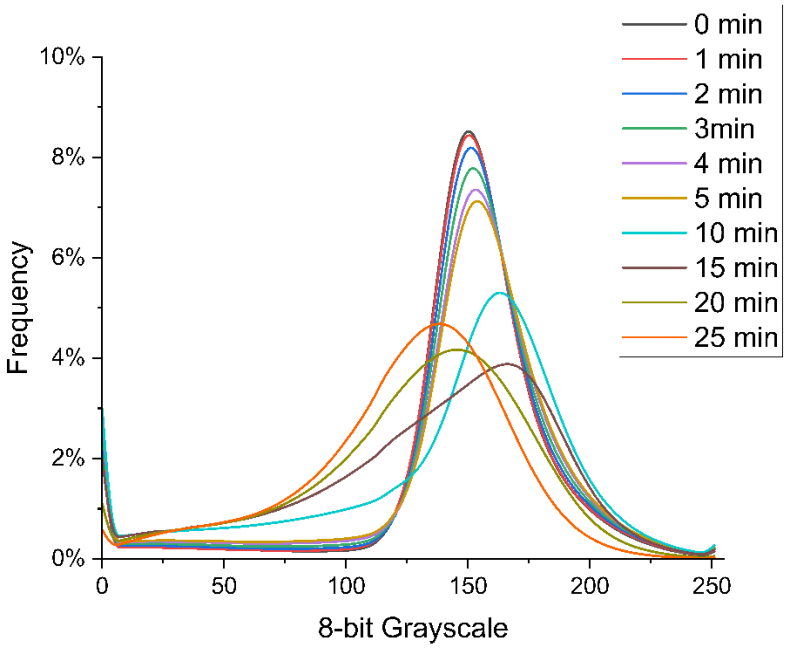

Figure 4.12 - Grayscale histogram curves taken from the reconstructed CT data for the drying of MCC at 0.06 m/s and 40 °C.

Initially, the wet granules see larger peak values trending toward the right-hand side of the plot, attributed to the higher moisture and pharmaceuticals within the sample, with a smaller peak towards the left-hand side of the plot, attributed to the lower air volume within the sample. As the granule undergoes drying, the peak values for the attenuation of the pharmaceutical materials and the moisture decrease, while an increase is observed in the peak values for the air content, seeing an overall shift of the curve downward and toward the lower left grayscale values. To illustrate the effects of moisture and air on the grayscale distribution, reference samples of pure components were processed, and their values are shown in Figure 4.13.

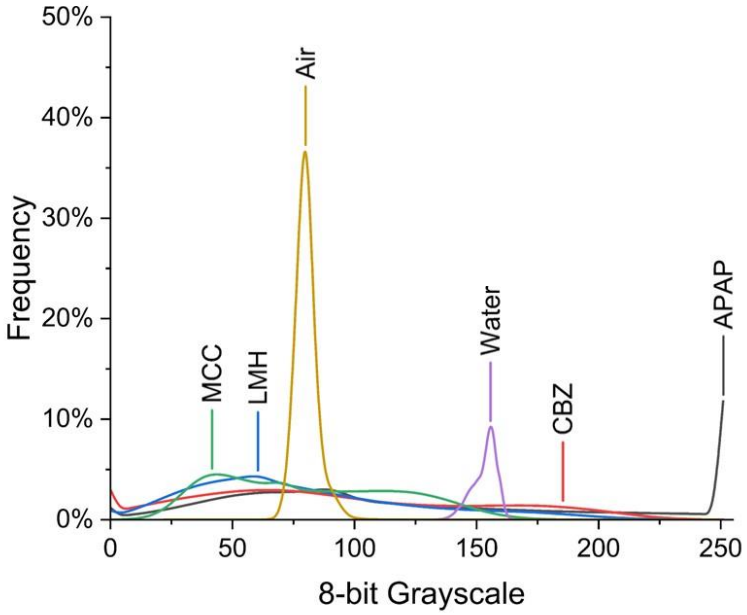

Figure 4.13 - Grayscale histogram curves for pure components.

To determine the moisture content at each time step within the granule, the segmented air volume fraction at each time step can be used to determine its contribution to the grayscale attenuation, with the contribution of any moisture within the air being negligible in comparison to the bound moisture within the solid fraction. The segmented X-ray intensity was determined from the grayscale values of each sample and control reference, a common method used in X-ray imaging for quantitative analysis [60]. Values representing an attenuation are then used with the Beer-Lambert Law [61]in conjunction with the given sample thickness to determine the overall linear attenuation coefficients for a sample.

$$\frac{N}{N_0} = \exp(-\mu l) \tag{4.7}$$

Where N/N_0 is the attenuation; μ is the linear attenuation coefficient; l is the sample thickness.

In addition to the obtained values, pure components of the pharmaceutical materials, water, and air were also determined to help calibrate the moisture content prediction. Using the known air volume fraction and the calculated overall linear attenuation coefficient for a sample at each given time, the moisture content at each time step can be calculated by an equation similar to equations (4.3) and (4.4):

$$\mu = (\mu_s * (1 - X) + \mu_w * X)(1 - \varepsilon) + \mu_a * \varepsilon \quad (4.8)$$

where μ is the overall linear attenuation coefficient; μ_s is the linear attenuation coefficient of the pharmaceutical solids; μ_w is the linear attenuation coefficient of water; μ_a is the linear attenuation coefficient of air; X is the moisture content; ε is the air volume fraction. The initial moisture content (X_0) and each time point for moisture content (X) can be used to determine the moisture ratio (MR) plots.

The obtained moisture ratio was fitted with the nine thin-layer drying models to evaluate the prediction for single-granule drying. The best model to predict the drying curve is determined by the largest R^2 and the smallest RMSE

Amongst the nine models, the Lewis model, the Henderson and Pabis model, and the Wang and Singh model were found to converge results for all samples with good R^2 and RMSE values, with the Henderson and Pabis model showing a prediction with the best overall R^2 values (average of 0.942) and the lowest RMSE values (average of 0.049). Tables 4.9-4.11 show the results for all samples as predicted by the Henderson and Pabis equation, with Figures 4.14-4.17 showing a comparison between the experimental data and the predicted data from the selected thin-layer drying model. While all models that converged have shown a relatively good agreement between experimental and predicted values, the Henderson and Pabis model possessed the smallest deviations, and is considered the best thin-layer drying model for the moisture ratio of the single pharmaceutical granules used in this work. Comparatively, models such as Midilli and Kucuk have been shown to fit well for larger scale operations like fluidized bed dryers with small deviations between experimental data and predicted values [35]. This can be attributed to varying factors related to the drying process, with the Midilli and Kucuk model better suited for situations where the drying gas velocity and temperature can vary significantly with their influence on the drying rate for non-uniform and irregularly shaped bodies of varying thickness, while the Henderson and Pabis model is better suited for materials of a relatively uniform thickness where the drying rate is more constant throughout the drying process. Furthermore, model selection and assessment describing thin-layer drying behaviour often take statistical parameters into consideration that produce a best-fit model, with the number of constants and form of the selected model offering better results for the criteria considering the application and material selected [62].

Table 4.9 - Thin-layer drying models for common APAP, MCC, and LMH type samples at 25 °C.

Material - Velocity	a	Std. Error	k_0	Std. Error	R^2	RMSE
APAP – 0.02 m/s	0.920	0.016	0.007	0.002	0.716	0.035
APAP – 0.06/s	0.972	0.007	0.007	0.001	0.938	0.014
APAP – 0.10 m/s	0.959	0.014	0.014	0.001	0.921	0.030
LMH – 0.02 m/s	1.054	0.019	0.052	0.003	0.986	0.035
LMH – 0.06 m/s	0.919	0.044	0.053	0.008	0.901	0.080
LMH – 0.10 m/s	1.075	0.052	0.082	0.011	0.951	0.086
MCC – 0.02 m/s	0.952	0.031	0.119	0.010	0.983	0.045
MCC – 0.06 m/s	1.029	0.054	0.180	0.022	0.971	0.069
MCC – 0.10 m/s	0.992	0.021	0.204	0.010	0.995	0.026
90MCC10APAP – 0.02 m/s	1.011	0.012	0.008	0.001	0.881	0.027
90MCC10APAP – 0.06 m/s	1.036	0.033	0.026	0.004	0.890	0.066
90MCC10APAP – 0.10 m/s	1.141	0.075	0.118	0.019	0.943	0.110
80MCC20APAP – 0.02 m/s	1.096	0.043	0.038	0.005	0.911	0.082
80MCC20APAP – 0.06 m/s	0.889	0.024	0.021	0.003	0.881	0.048
80MCC20APAP – 0.10 m/s	0.860	0.040	0.027	0.005	0.787	0.079
50MCC50APAP – 0.02 m/s	0.997	0.010	0.029	0.001	0.989	0.021
50MCC50APAP – 0.06 m/s	1.077	0.029	0.044	0.004	0.963	0.054
50MCC50APAP – 0.10 m/s	1.080	0.033	0.066	0.006	0.973	0.057
90LMH10APAP – 0.02 m/s	0.985	0.015	0.032	0.002	0.979	0.030
90LMH10APAP – 0.06 m/s	0.959	0.012	0.032	0.002	0.985	0.024
90LMH10APAP – 0.10 m/s	0.998	0.007	0.051	0.001	0.998	0.013
80LMH20APAP – 0.02 m/s	0.963	0.008	0.012	0.001	0.968	0.017
80LMH20APAP – 0.06 m/s	1.005	0.021	0.018	0.002	0.909	0.043
80LMH20APAP – 0.10 m/s	0.958	0.010	0.023	0.001	0.985	0.019
50LMH50APAP – 0.02 m/s	0.954	0.016	0.009	0.002	0.820	0.034

50LMH50APAP – 0.06 m/s	0.915	0.021	0.013	0.002	0.815	0.045
50LMH50APAP – 0.10 m/s	0.927	0.014	0.005	0.001	0.635	0.030

Table 4.10 - Thin-layer drying models for common APAP, MCC, and LMH type samples at 40 °C

Material - Velocity	a	Std. Error	k_0	Std. Error	R^2	RMSE
APAP – 0.02 m/s	0.958	0.012	0.011	0.001	0.918	0.025
APAP – 0.06/s	0.863	0.029	0.024	0.004	0.859	0.058
APAP – 0.10 m/s	1.052	0.024	0.034	0.003	0.959	0.048
LMH – 0.02 m/s	1.006	0.020	0.051	0.003	0.982	0.037
LMH – 0.06 m/s	1.129	0.061	0.102	0.014	0.951	0.094
LMH – 0.10 m/s	1.138	0.084	0.143	0.026	0.938	0.116
MCC – 0.02 m/s	1.083	0.032	0.076	0.006	0.977	0.054
MCC – 0.06 m/s	1.083	0.032	0.076	0.006	0.977	0.054
MCC – 0.10 m/s	1.097	0.034	0.051	0.005	0.960	0.062
90MCC10APAP – 0.02 m/s	0.947	0.022	0.042	0.003	0.967	0.042
90MCC10APAP – 0.06 m/s	1.056	0.023	0.043	0.003	0.975	0.043
90MCC10APAP – 0.10 m/s	1.123	0.070	0.093	0.015	0.935	0.110
80MCC20APAP – 0.02 m/s	1.045	0.020	0.037	0.003	0.975	0.039
80MCC20APAP – 0.06 m/s	1.087	0.036	0.063	0.006	0.965	0.063
80MCC20APAP – 0.10 m/s	1.085	0.073	0.123	0.021	0.942	0.106
50MCC50APAP – 0.02 m/s	0.936	0.025	0.065	0.005	0.978	0.043
50MCC50APAP – 0.06 m/s	0.983	0.019	0.069	0.004	0.989	0.033
50MCC50APAP – 0.10 m/s	0.999	0.022	0.072	0.004	0.986	0.038
90LMH10APAP – 0.02 m/s	0.956	0.012	0.030	0.002	0.983	0.025
90LMH10APAP – 0.06 m/s	1.067	0.034	0.045	0.005	0.950	0.064
90LMH10APAP – 0.10 m/s	0.944	0.019	0.057	0.003	0.984	0.034

80LMH20APAP – 0.02 m/s	0.910	0.021	0.048	0.004	0.973	0.039
80LMH20APAP – 0.06 m/s	0.981	0.025	0.218	0.012	0.992	0.031
80LMH20APAP – 0.10 m/s	1.009	0.022	0.566	0.023	0.996	0.023
50LMH50APAP – 0.02 m/s	0.880	0.052	0.056	0.010	0.861	0.093
50LMH50APAP – 0.06 m/s	0.907	0.022	0.035	0.003	0.955	0.042
50LMH50APAP – 0.10 m/s	0.959	0.015	0.034	0.002	0.979	0.030

Table 4.11 - Thin-layer drying models for common CBZ-type samples.

Material – Velocity – Temperature	a	Std. Error	k_0	Std. Error	R^2	RMSE
CBZ – 0.02 m/s – 25 °C	1.006	0.014	0.054	0.002	0.992	0.0260
CBZ – 0.02 m/s – 40 °C	1.085	0.057	0.047	0.008	0.889	0.106
CBZ – 0.10 m/s – 25 °C	1.132	0.062	0.075	0.011	0.932	0.104
CBZ – 0.10 m/s – 40 °C	1.054	0.042	0.077	0.008	0.964	0.070
50MCC50CBZ – 0.02 m/s – 25 °C	1.004	0.016	0.017	0.002	0.943	0.032
50MCC50CBZ – 0.02 m/s – 40 °C	1.040	0.016	0.024	0.002	0.968	0.033
50MCC50CBZ – 0.10 m/s – 25 °C	1.028	0.040	0.052	0.006	0.942	0.073
50MCC50CBZ – 0.10 m/s – 40 °C	1.017	0.031	0.060	0.005	0.969	0.056
50LMH50CBZ – 0.02 m/s – 25 °C	0.990	0.012	0.065	0.002	0.995	0.020
50LMH50CBZ – 0.02 m/s – 40 °C	0.989	0.014	0.051	0.002	0.992	0.025
50LMH50CBZ – 0.10 m/s – 25 °C	0.951	0.015	0.076	0.003	0.993	0.026
50LMH50CBZ – 0.10 m/s – 40 °C	0.951	0.017	0.068	0.003	0.991	0.029

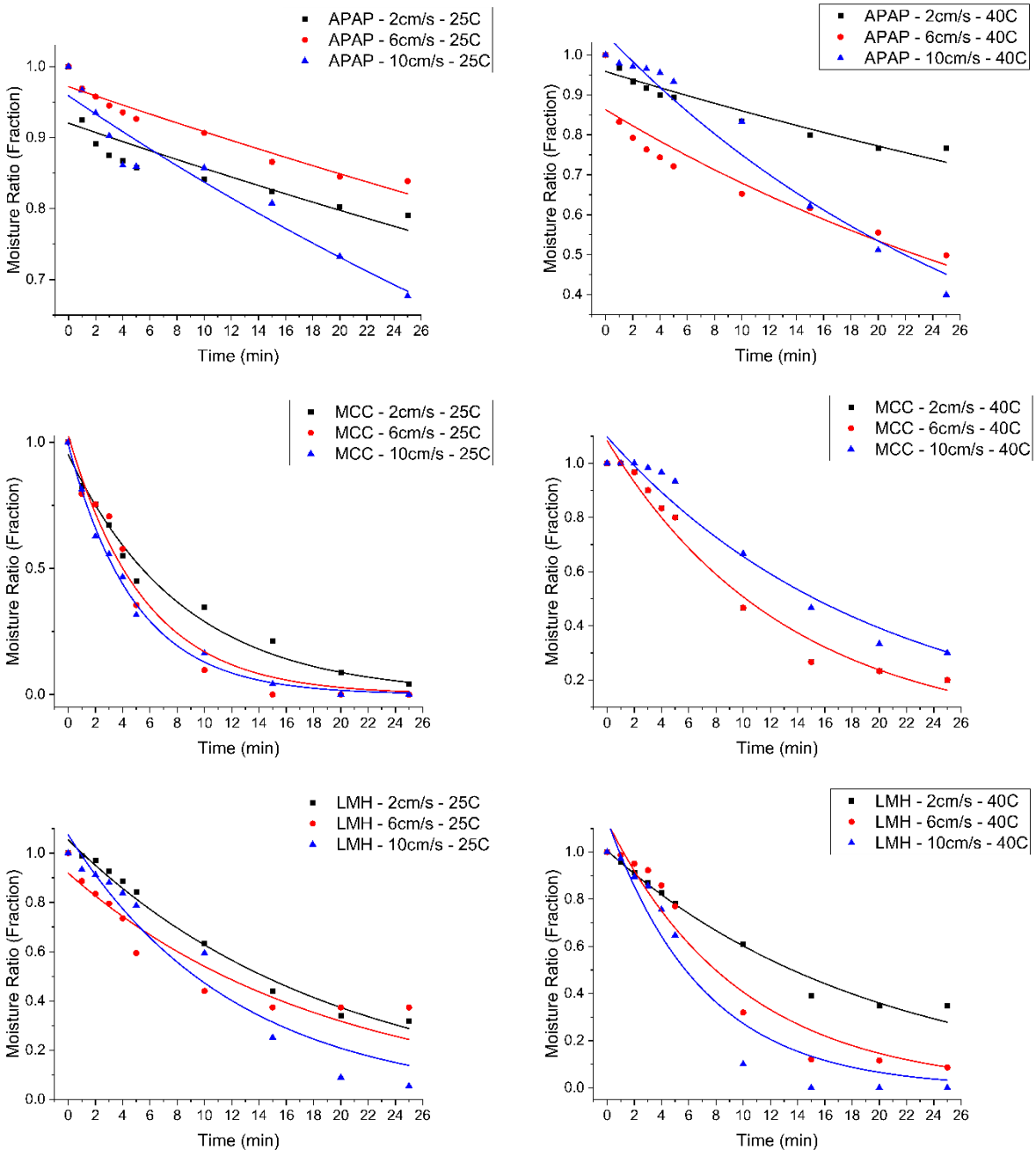

Figure 4.14 - Comparison of the experimental data and predicted values of moisture ratio for single granule drying of pure APAP, MCC, and LMH granules.

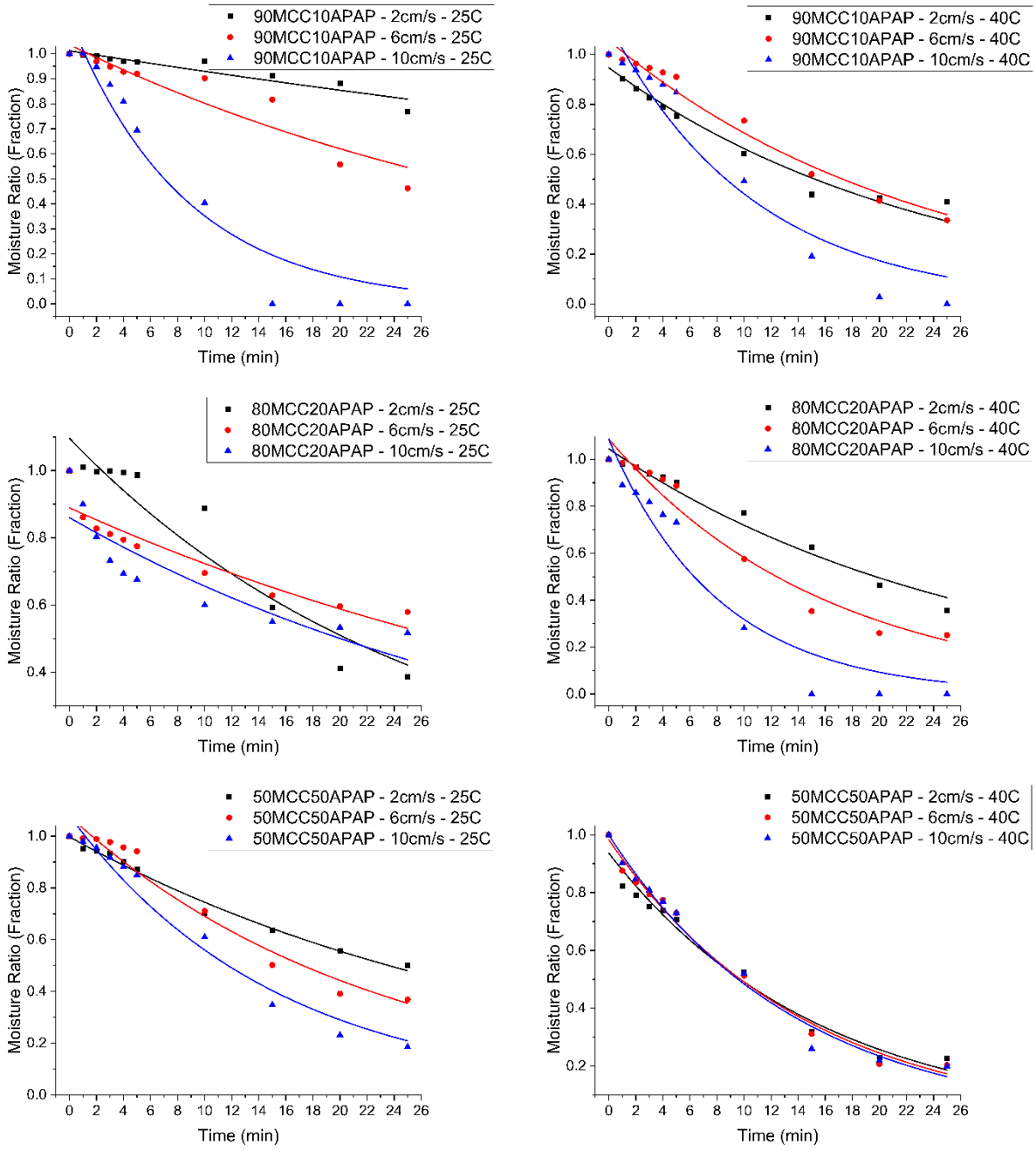

Figure 4.15 - Comparison of the experimental data and predicted values of moisture ratio for single granule drying of MCC/APAP binary granules.

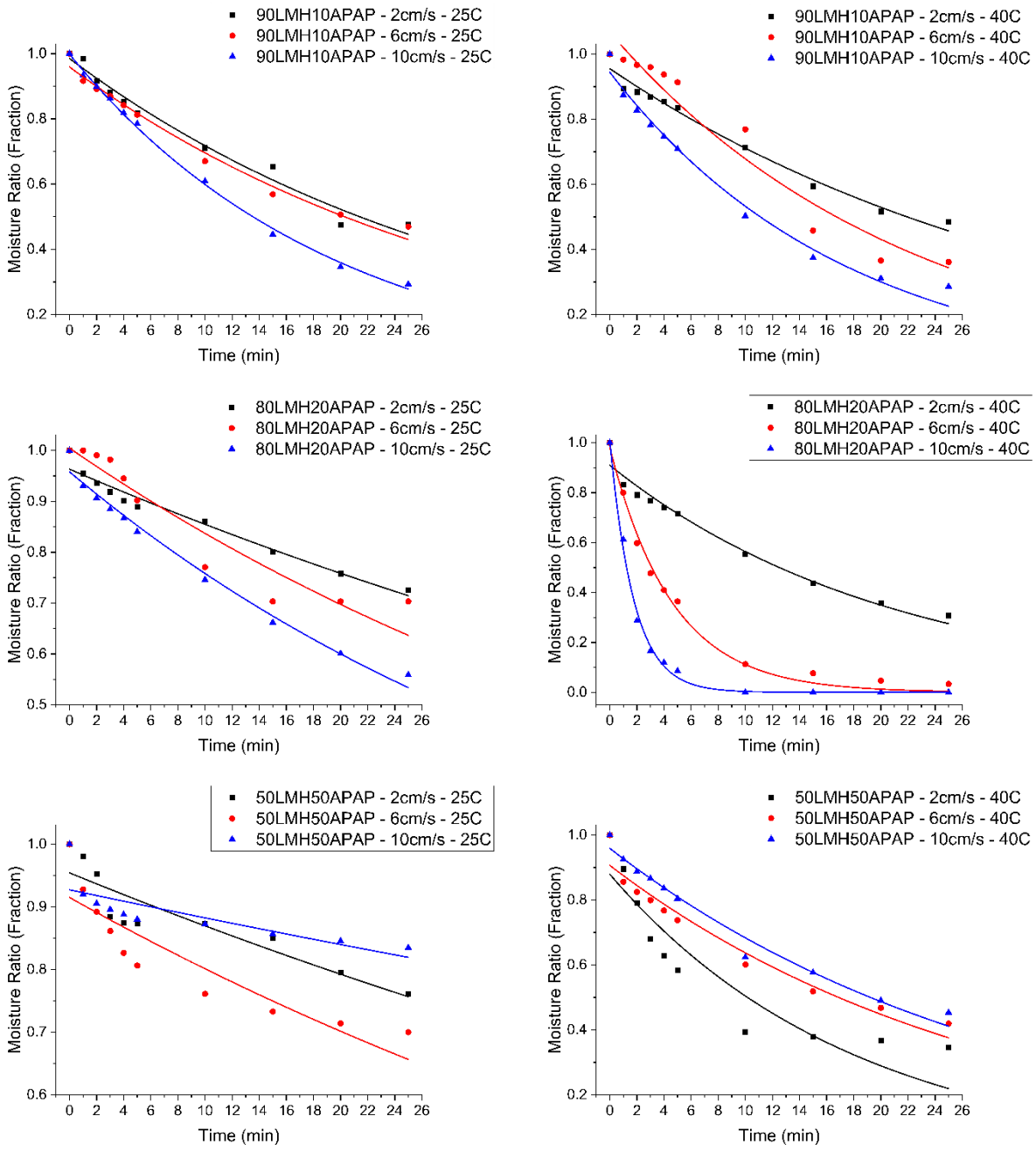

Figure 4.16 - Comparison of the experimental data and predicted values of moisture ratio for single granule drying of LMH/APAP binary granules.

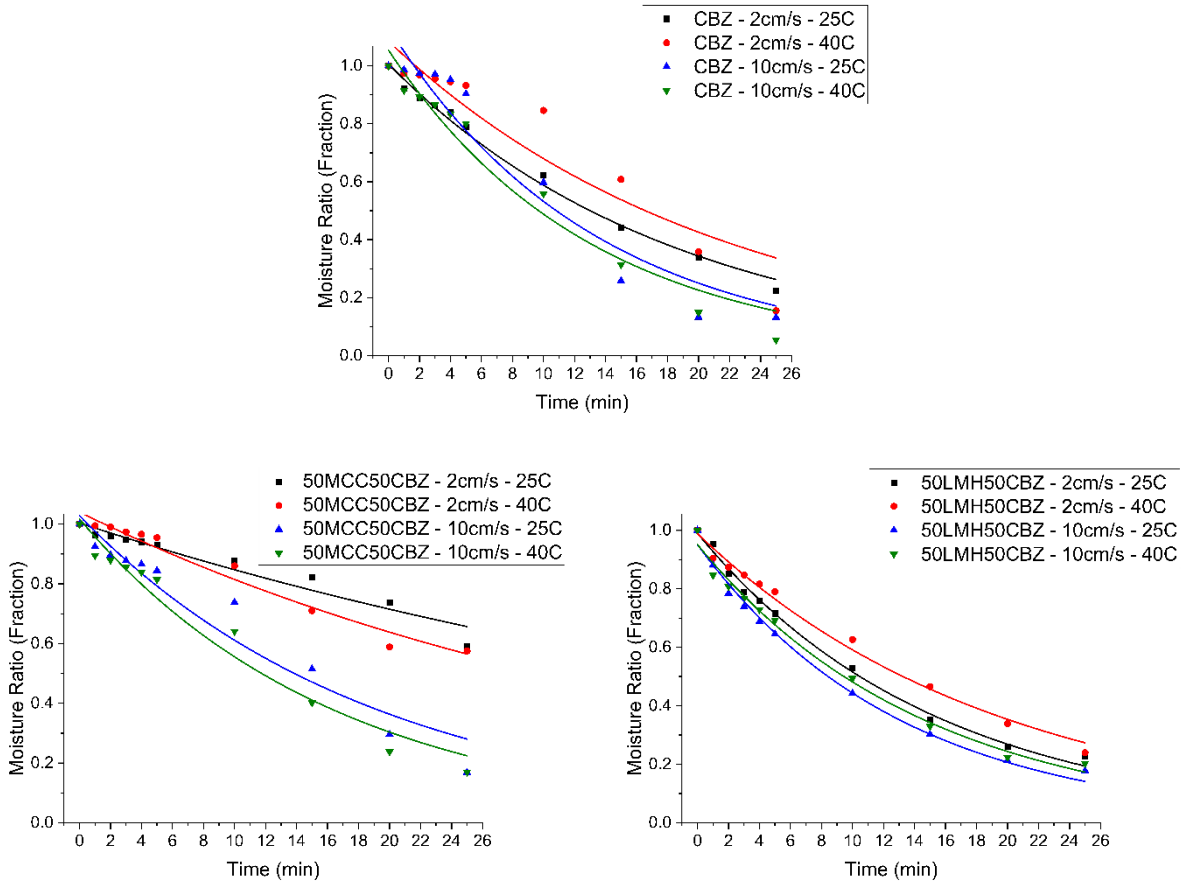

Figure 4.17 - Comparison of the experimental data and predicted values of moisture ratio for single granule drying of pure CBZ and excipient/CBZ binary granules.

A summary of the changes observed in the moisture ratio can be seen from the ANOVA results depicted in Table 4.12. All samples tested were included, with parameters of temperature, velocity, and time tested for each sample set. It should be noted that the results were also tested for sample composition across all samples, with the results finding significant influence from the sample composition on the moisture ratio changes with a p-value <0.001 (significance <0.05).

Table 4.12 - ANOVA results for the significance of investigated variables on the moisture ratio.

Material	Drying time significance	Drying air velocity significance	Drying air temperature significance
APAP	<0.001	0.449	0.025
MCC	<0.001	0.944	0.004
LMH	<0.001	0.398	0.514
90MCC10APAP	<0.001	0.031	0.262
80MCC20APAP	<0.001	0.081	0.258
50MCC50APAP	<0.001	0.851	0.05
90LMH10APAP	<0.001	0.283	0.761
80LMH20APAP	0.01	0.058	<0.001
50LMH50APAP	<0.001	0.419	<0.001
CBZ	<0.001	0.498	0.887
50MCC50CBZ	<0.001	0.019	0.723
50LMH50CBZ	<0.001	0.428	0.691

Within the observed changes to the moisture ratio, the drying time significantly influences changes in the moisture ratio as expected for all samples. As seen in Figures 4.14-4.17, both the experimental data and the predicted values follow a decreasing trend, which is expected for drying processes, with moisture content gradually decreased as factors of drying time, drying gas flow rate, and temperature increase [63,64]. This is easily seen in examples such as 80LMH20APAP in Figure 4.16, where the increase in velocity allows for a larger decrease in the moisture ratio, with increasing temperature observed to further decrease the moisture ratio over the same drying time. The drying time for all samples is comparable to results seen in methods such as acoustic levitation or a drying channel, with curve shapes similar to larger scale drying operations such as the use of fluidized bed drying for pharmaceutical granules [24,35]. This similarity is predominant in granules with 10 % to 20 % APAP loading for both MCC and LMH at higher temperatures, where the effects of increasing the drying gas velocity and temperature are more noticeable, although with a much shorter drying time resulting from the use of stationary single granules as compared to an entire bed of fluidized material [35].

The effects of the drying air velocity is observed to have mixed significance on the changes to the moisture ratio of the investigated pharmaceuticals, with 90MCC10APAP and 50MCC50CBZ being significantly influenced. These changes show a significant decrease in the

time required to achieve a lower moisture ratio as the drying air velocity is increased, while all other samples exhibited similar drying patterns for different velocities. The result of the drying air velocity not being overly significant in influencing changes in the moisture content and the drying kinetics may be attributed to capillary action and a strong retention of water molecules within hydrophilic, colloidal, organic materials [65,66].

Similar to the results for the effects of velocity, the effect of temperature was found to be of mixed significance on the changes to the moisture ratio. Pure APAP and MCC samples were found to be significantly influenced by an increase in the drying air temperature, with higher loadings of APAP in binary mixtures with excipients also being significantly impacted. While temperature changes were not found to significantly influence the drying of pure LMH, loadings of 20 % to 50 % APAP were found to be significant, exhibiting a shift from the drying of pure LMH as the drying becomes more dominated by the drying behaviour of APAP. Interestingly, the 50LMH50APAP group subject to the drying temperature of 40 °C as seen in Figure 4.16 is observed to have a larger decrease in the moisture ratio at lower velocities. From the 3D reconstructions of the data, the 50LMH50APAP granules are observed to form the surface crust much faster from the combined effects of increased temperature and velocity, inhibiting the removal of moisture and trapping water within the center of the granules. By decreasing the velocity, the increased temperature can still allow for the promotion of moisture transfer from the material to the surrounding air without the crust forming as rapidly, where diffusion and evaporation would be limited. APAP loadings of 50 % were found to be significant on the drying of MCC, again showing a trend toward APAP dominating the drying behaviour at higher API loadings as a result of the hydrophilic nature of APAP. Increased loading of the moderately hydrophobic CBZ was not shown to have any difference in the drying behaviour of its pure component and in binary mixtures with pharmaceutical excipients for an increase in temperature. For the samples where the drying gas velocity may not be significant while still being significantly influenced by temperature, it is indicative of temperature overriding the effects of capillary action and water retention; the vapour pressure of the surrounding air further promoting the transfer of moisture from the material to the surrounding air by diffusion as the increase in energy increases the evaporation rate with a higher temperature gradient observable between the drying gas and the granules surface [35,67,68].

Comparing the excipients of MCC and LMH, the materials possess drastically different mechanisms when in contact with water. While lactose is observed to dissolve directly into water and form pastes, MCC exhibits a swelling within the fine capillaries of the material as moisture in introduced [21]. Conversely, during the drying process by means of hot air, LMH is permitted to reform as the solvent evaporates and the concentration of the dissolved materials increases. However, the trapped moisture within the swelled MCC granules fine capillaries and internal pores pulls on the bounded regions as evaporation occurs due to capillary action resulting from the high surface tension of water [58].

The differences of the two APIs tested can also be compared, with several notable differences observed as a result of the difference in hydrophilicity and hydrophobicity. While the effect of temperature does not significantly influence the drying behaviour of CBZ, the increase in energy permits the bound water of APAP granules to be liberated more easily, significantly decreasing the moisture ratio. This is likely due to the hydrophilic nature of APAP, as the bound water will require a higher energy input for evaporative effects to occur more efficiently. For the API loadings on both excipients, CBZ was not shown to impact the drying behaviour of either MCC or LMH, with results comparable to the drying of their respective pure components. However, by increasing the loading of APAP on either excipient, the drying behaviour became more dominated by the hydrophilic effects of APAP, with the drying nature trending more toward the behaviour of pure APAP.

Resulting from the changes to the pore volume as the individual granules structure is influenced by the changes in moisture content, the single granules hardness is subject to changes influenced by pore properties [33,69]. Before the drying process, the granules higher initial moisture content creates a soft and flexible internal structure. As drying is introduced and moisture is permitted to evaporate, the pore volume changes, and the individual granules become more rigid. As observed by Danalou et al. [33], an individual granule with lower porosity and finer pores exhibits a higher hardness, with materials such as LMH possessing a higher hardness from a smaller mean pore volume. For all of the samples used in this study, the coupled pore volume and moisture content changes can be used to evaluate the hardness of the produced granules. For all materials, the increase in the temperature and velocity of the drying air enhances the efficiency of moisture removal and will generally increase the hardness, although

excessive conditions may lead to degradation and impacts on the granule quality resulting from uneven drying [16], with the decreased moisture content and pore volume of samples consisting of LMH and 80LMH20APAP consistent with higher hardness findings from Danalou et al. [33].

To examine the reproducibility of the experiments, three replicates each of LMH at 0.10 m/s at 25 °C and 40 °C were processed respectively. The results for the moisture ratio changes can be seen in Figure 4.18.

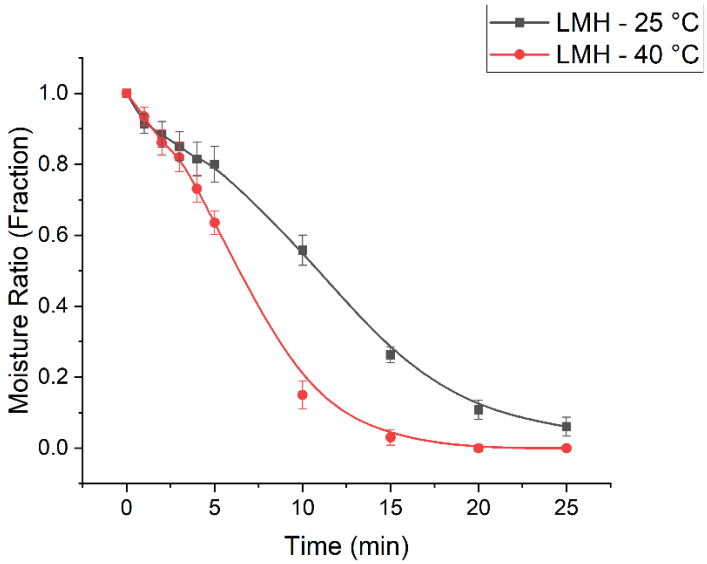

Figure 4.18 - Quantified changes to the moisture ratio for LMH replicates at 25 °C and 40 °C at 0.10 m/s to determine repeatability.

Similar to those results seen in Figure 4.14, the moisture ratio decreases for both temperatures as drying continues, with the effect of temperature accelerating this change. The curves are consistent with those results seen in Figure 4.14, with acceptable deviations observed between the error bars and data points seen in Figure 4.18 and the data points seen in Figure 4.14.

4.6 Conclusions

In this work, synchrotron X-ray micro-computed tomography was used to determine the influence of drying air parameters of time, velocity, and temperature on the single pharmaceutical granule drying behaviour of APAP, MCC, LMH, CBZ, and their mixtures. Segmentation was performed to view pore volume changes, with histogram data extracted for the granule region to determine changes in the moisture content. The drying time and sample composition were found to significantly impact the pore volume evolution and the change in moisture ratio for all samples, with parameters of the drying gas velocity and temperature possessing mixed significance on the drying across the range of tested sample compositions. The findings of this work could be used to predict the porosity and moisture content of single granules during the dynamic drying process, with further implications in predicting thermal conductivity and volumetric specific heat capacity for modelling single granule drying within the equations of heat and mass transfer.

4.7 Acknowledgements

The authors would like to gratefully acknowledge Divyapratim Das, Tolu Emiola-Sadiq, Mojtaba Nabipoor Hassankiadeh, Denis Kalugin, and Amy Coller from the University of Saskatchewan for all of their help in performing experiments, who without, this research would not have been possible. The authors would also like to acknowledge Dr. Jerry Heng from the Imperial College of London and Dr. Apostolos Kantzas from the University of Calgary for their technical contributions and recommendations. All research described within this work was performed at the Canadian Light Source, serving the Canadian and global scientific community thanks to the support of the Canada Foundation for Innovation (CFI), the Natural Sciences and Engineering Research Council (NSERC), the National Research Council (NRC), the Canadian Institutes of Health Research (CIHR), the Government of Saskatchewan, and the University of Saskatchewan.

4.8 References

[1] Deck, L.-T., Ochsenbein, D. R., & Mazzotti, M. (2022). Stochastic shelf-scale modeling framework for the freezing stage in freeze-drying processes. International Journal of Pharmaceutics, 613, 121276.

[2] Yadav, D., & Kumar, N. (2014). Nanonization of curcumin by antisolvent precipitation: Process development, characterization, freeze drying and stability performance. International Journal of Pharmaceutics, 477(1–2), 564–577.

[3] Salmon, A., Hounslow, M. J., Seville, J. P. K., & ScienceDirect, vendor. (2007). Granulation (1st ed., Handbook of powder technology ; v. 11).

[4] Kan, Nakamura, H., & Watano, S. (2018). Effect of collision angle on particle-particle adhesion of colliding particles through liquid droplet. Advanced Powder Technology : the International Journal of the Society of Powder Technology, Japan, 29(6), 1317–1322. https://doi.org/10.1016/j.apt.2018.02.026

[5] Lehmann, S., Oesau, T., Jongsma, A., Innings, F., & Heinrich, S. (2020). Material specific drying kinetics in fluidized bed drying under mechanical vibration using the reaction engineering approach. Advanced Powder Technology : The International Journal of the Society of Powder Technology, Japan, 31(12), 4699-4713.

[6] Maxwell, J.C. (1890). In: Niven, W.D. (ed). Collected scientific papers. Cambridge University Press, Cambridge. http://strangebeautiful.com/other-texts/maxwell-scientific-papers-vol-1.pdf, http://strangebeautiful.com/other-texts/maxwell-scientific-papers-vol-2.pdf

[7] Breinlinger, T., Hashibon, A., & Kraft, T. (2015). Simulation of the influence of surface tension on granule morphology during spray drying using a simple capillary force model. Powder Technology, 283, 1-8.

[8] Mezhericher, M., Levy, A., & Borde, I. (2007). Theoretical Drying Model of Single Droplets Containing Insoluble or Dissolved Solids. Drying Technology, 25(6), 1025–1032. https://doi.org/10.1080/07373930701394902

[9] Mortier, S. T. F. ., De Beer, T., Gernaey, K. V., Vercruysse, J., Fonteyne, M., Remon, J. P., Vervaet, C., & Nopens, I. (2012). Mechanistic modelling of the drying behaviour of single pharmaceutical granules. European Journal of Pharmaceutics and Biopharmaceutics, 80(3), 682–689. https://doi.org/10.1016/j.ejpb.2011.12.010

[10] Breinlinger, T., Hashibon, A., & Kraft, T. (2015). Simulation of the Spray Drying of Single Granules: The Correlation Between Microscopic Forces and Granule Morphology. Journal of the American Ceramic Society, 98(6), 1778-1786.

[11] Vandeputte, T., Ghijs, M., De Beer, T., & Nopens, I. (2024). Cracking the code: Spatial heterogeneity as the missing piece for modeling granular fluidized bed drying. International Journal of Pharmaceutics, 657, 124135.

[12] Taghavivand, M., Choi, K., & Zhang, L. (2017). Investigation on drying kinetics and tribocharging behaviour of pharmaceutical granules in a fluidized bed dryer. Powder Technology, 316, 171-180.

[13] Putra, R. N., & Ajiwiguna, T. A. (2017). Influence of Air Temperature and Velocity for Drying Process. Procedia Engineering, 170, 516-519.

[14] Reyer, S., Awiszus, S., Meissner, K., & Müller, J. (2020). High precision laboratory dryer for thin layer and bulk drying with adjustable temperature, relative humidity and velocity of the drying air. HardwareX, 8, e00133.

[15] Zammouri, A., Mihoubi, N. B., & Kechaou, N. (2022). A performance analysis of batch fluidized bed drying of two pharmaceutical powders by desirability approach. Drying Technology, 40(6), 1210-1231.

[16] Gilpin, R. K., & Zhou, W. (2004). Studies of the Thermal Degradation of Acetaminophen Using a Conventional HPLC Approach and Electrospray Ionization-Mass Spectrometry. Journal of Chromatographic Science, 42(1), 15-20.

[17] Li, C., Zhu, N., Emady, H. N., & Zhang, L. (2019). Synchrotron-based X-ray in-situ imaging techniques for advancing the understanding of pharmaceutical granulation. International Journal of Pharmaceutics, 572, 118797.

[18] Asada, T., Kobiki, M., Ochiai, Y., Iwao, Y., & Itai, S. (2017). An innovative method for the preparation of high API-loaded hollow spherical granules for use in controlled-release formulation. International Journal of Pharmaceutics, 523(1), 167–175.

[19] Blocka, C., Nabipoor Hassankiadeh, M., Zhang, L., & Baik, O.-D. (2023). Effects of moisture content and porosity on the thermal conductivity and volumetric specific heat capacity of pharmaceutical powders. International Journal of Pharmaceutics, 642, 123130.

[20] Khoo, J. Y., Heng, J. Y. Y., & Williams, D. R. (2010). Agglomeration Effects on the Drying and Dehydration Stability of Pharmaceutical Acicular Hydrate: Carbamazepine Dihydrate. Industrial & Engineering Chemistry Research, 49(1), 422-427.

[21] Kyttä, K. M., Lakio, S., Wikström, H., Sulemanji, A., Fransson, M., Ketolainen, J., & Tajarobi, P. (2020). Comparison between twin-screw and high-shear granulation - The effect of filler and active pharmaceutical ingredient on the granule and tablet properties. Powder Technology, 376, 187-198.

[22] Assar, M., Golmohammadi, M., Rajabi-Hamaneh, M., & Hassankiadeh, M. N. (2016). A Combined Experimental and Theoretical Approach to Study Temperature and Moisture Dynamic Characteristics of Intermittent Paddy Rice Drying. Chemical Engineering Communications, 203(9), 1242-1250.

[23] Vandeputte, T., Ghijs, M., Van Hauwermeiren, D., Dos Santos Schultz, E., Schäfer, E., Stauffer, F., De Beer, T., Nopens, I. (2023). Mechanistic modeling of semicontinuous fluidized bed drying of pharmaceutical granules by incorporating single particle and bulk drying kinetics. International Journal of Pharmaceutics, 646, 123447.

[24] Groenewold, C., Möser, C., Groenewold, H., & Tsotsas, E. (2002). Determination of single-particle drying kinetics in an acoustic levitator. Chemical Engineering Journal (1996), 86(1), 217-222.

[25] Schiffter, H., & Lee, G. (2007). Single-Droplet Evaporation Kinetics and Particle Formation in an Acoustic Levitator. Part 1: Evaporation of Water Microdroplets Assessed Using Boundary-Layer and Acoustic Levitation Theories. Journal of Pharmaceutical Sciences, 96(9), 2274-2283.

[26] Janocha, M., & Tsotsas, E. (2022). Coating layer formation from deposited droplets: A comparison of nanofluid, microfluid and solution. Powder Technology, 399, 117202.

[27] Rantalainen, T., Chivers, P., Beck, B. R., Robertson, S., Hart, N. H., Nimphius, S., Weeks, B. K., McIntyre, F., Hands, B., Siafarikas, A. (2018). Please Don't Move—Evaluating Motion Artifact From Peripheral Quantitative Computed Tomography Scans Using Textural Features. Journal of Clinical Densitometry, 21(2), 260-268.

[28] Keklikoglou, K., Arvanitidis, C., Chatzigeorgiou, G., Chatzinikolaou, E., Karagiannidis, E., Koletsa, T., Magoulas, A., Makris, K., Mavrothalassitis, G., Papanagnou, E.-D., Papazoglou, A. S., Pavloudi, C., Trougakos, I. P., Vasileiadou, K. Vogiatzi, A. (2021). Micro-CT for Biological and Biomedical Studies: A Comparison of Imaging Techniques. Journal of Imaging, 7(9), 172.

[29] Triche, B. L., Nelson, Jr, John T, McGill, N. S., Porter, K. K., Sanyal, R., Tessler, F. N., McConathy, J. E., Gauntt, D. M., Yester, M. V., Singh, S. P. (2019). Recognizing and Minimizing Artifacts at CT, MRI, US, and Molecular Imaging. Radiographics, 39(4), 1017-1018.

[30] Barrett, J. F., & Keat, N. (2004). Artifacts in CT: recognition and avoidance. Radiographics, 24(6), 1679-1691.

[31] Danalou, S. Z., Ding, X. F., Zhu, N., Emady, H. N., & Zhang, L. (2022). 4D study of liquid binder penetration dynamics in pharmaceutical powders using synchrotron X-ray micro computed tomography. International Journal of Pharmaceutics, 627, 122192.

[32] Li, C., Zhang, Y., Zhu, N., Emady, H. N., & Zhang, L. (2021). Experimental investigation of wet pharmaceutical granulation using in-situ synchrotron X-ray imaging. Powder Technology, 378, 65-75.

[33] Zeinali Danalou, S., Blocka, C., Yang, J., Zhu, N., Emady, H. N., Wasan, E., & Zhang, L. (2023). Advanced 3D and 4D microstructure study of single granule formation for pharmaceutical powders using synchrotron x-ray imaging. AIChE Journal, 69(5), n/a.

[34] Prakash, B., & Pan, Z. (2012). Effect of Geometry of Rice Kernels on Drying Modeling Results. Drying Technology, 30(8), 801-807.

[35] Li, C., Blocka, C., & Zhang, L. (2022). Experimental investigation on drying performance of pharmaceutical granules in a pulsation-assisted fluidized bed dryer. Canadian Journal of Chemical Engineering, 100(9), 2608-2622.

[36] He, C., Wang, H., Yang, Y., Huang, Y., Zhang, X., Arowo, M., Ye, J., Zhang, N., & Xiao, M. (2021). Drying Behavior and Kinetics of Drying Process of Plant-Based Enteric Hard Capsules. Pharmaceutics, 13(3), 335.

[37] Celma, A. R., Cuadros, F., & López-Rodríguez, F. (2012). Convective drying characteristics of sludge from treatment plants in tomato processing industries. Food and Bioproducts Processing, 90(2), 224-234.

[38] Sacilik, K., & Elicin, A. K. (2006). The thin layer drying characteristics of organic apple slices. Journal of Food Engineering, 73(3), 281-289.

[39] Lewis, W. K. (1921). The Rate of Drying of Solid Materials. Journal of Industrial and Engineering Chemistry, 13(5), 427-432.

[40] Page, G. E. (1949). FACTORS INFLUENCING THE MAXIMUM RATES OF AIR DRYING SHELLED CORN IN THIN LAYERS.

[41] Henderson, S.M. and Pabis, S. (1961) Grain Drying Theory: Temperature Effect on Drying Coefficient. Journal of Agricultural Engineering Research, 6, 169-174.

[42] Yaldiz, O., Ertekin, C., & Uzun, H. I. (2001). Mathematical modeling of thin layer solar drying of sultana grapes. Energy (Oxford), 26(5), 457-465.

[43] Henderson, S. M. (1974). Progress in developing the thin layer drying equation [for maize]. Transactions of the ASAE (USA), 17(6), Transactions of the ASAE (USA), 1974, Vol.17 (6).

[44] Y. I. Sharaf-Eldeen. (1980). A Model for Ear Corn Drying. Transactions of the ASAE, 23(5), 1261-1265.

[45] Wang, C. Y., & Singh, R. P. (1978). A single layer drying equation for rough rice (No. 78-3001, p. 33). ASAE paper.

[46] Midilli, A., Kucuk, H., & Yapar, Z. (2002). A NEW MODEL FOR SINGLE-LAYER DRYING. Drying Technology, 20(7), 1503-1513.

[47] Hii, C. L., Law, C. L., & Cloke, M. (2009). Modeling using a new thin layer drying model and product quality of cocoa. Journal of Food Engineering, 90(2), 191-198.

[48] Zhang, Y., Hirpara, V., Patel, V., Li, C., Anderson, R., Zhu, N., & Zhang, L. (2021). Imaging of desaturation of the frozen gas diffusion layers by synchrotron X-ray radiography. International Journal of Hydrogen Energy, 46(34), 17897-17908.

[49] Seo, D., Tomizato, F., Toda, H., Uesugi, K., Takeuchi, A., Suzuki, Y., & Kobayashi, M. (2012). Spatial resolution of synchrotron x-ray microtomography in high energy range: Effect of x-ray energy and sample-to-detector distance. Applied Physics Letters, 101(26), 1.

[50] Ding, X. F., Zeinali Danalou, S., Zhang, L., & Zhu, N. (2023). In situ wet pharmaceutical granulation captured using synchrotron radiation based dynamic micro-CT. Journal of Synchrotron Radiation, 30(2), 430-439.

[51] Faragó, T., Gasilov, S., Emslie, I., Zuber, M., Helfen, L., Vogelgesang, M., & Baumbach, T. (2022). Tofu: a fast, versatile and user-friendly image processing toolkit for computed tomography. Journal of Synchrotron Radiation, 29(3), 916-927.

[52] Vogelgesang, M., Farago, T., Morgeneyer, T. F., Helfen, L., dos Santos Rolo, T., Myagotin, A., & Baumbach, T. (2016). Real-time image-content-based beamline control for smart 4D X-ray imaging. Journal of Synchrotron Radiation, 23(5), 1254-1263.

[53] Kirz, J., Attwood, D. T., Henke, B. L., Howells, M. R., Kennedy, K. D., Kim, K.-J., Kortright, J. B., Perera, R. C. C., Pianetta, P., Riordan, J. C., Scofield, J. H., Stradling, G. L., Thompson, A. C., Underwood, J. H., Vaughan, D., Williams, G. P., & Winick, H. (1986). Center for X-ray Optics, X-ray Data Booklet.

[54] Barakat, N. S., Elbagory, I. M., & Almurshedi, A. S. (2008). Formulation, Release Characteristics and Bioavailability Study of Oral Monolithic Matrix Tablets Containing Carbamazepine. AAPS PharmSciTech, 9(3), 931–938.

[55] Maswal, M., Pandith, A. H., Islam, N., & Dar, A. A. (2013). Co-solubilization of the Hydrophobic Drugs Carbamazepine and Nifedipine in Aqueous Nonionic Surfactant Media. Journal of Solution Chemistry, 42(7), 1374-1392.

[56] Lesov, I., Tcholakova, S., & Denkov, N. (2014). Drying of particle-loaded foams for production of porous materials: mechanism and theoretical modeling. RSC Advances, 4(2), 811–823.

[57] Hamamoto, S., Ohko, Y., Ohtake, Y., Moldrup, P., & Nishimura, T. (2022). Water- and air-filled pore networks and transport parameters under drying and wetting processes. Vadose Zone Journal, 21(4), n/a.

[58] Bashaiwoldu, A. B., Podczeck, F., & Newton, J. M. (2004). A study on the effect of drying techniques on the mechanical properties of pellets and compacted pellets. European Journal of Pharmaceutical Sciences, 21(2–3), 119–129.

[59] Thomik, M., Gruber, S., Kaestner, A., Foerst, P., Tsotsas, E., & Vorhauer-Huget, N. (2022). Experimental Study of the Impact of Pore Structure on Drying Kinetics and Sublimation Front Patterns. Pharmaceutics, 14(8), 1538.

[60] Kelkar, S., Boushey, C. J., & Okos, M. (2015). A method to determine the density of foods using X-ray imaging. Journal of Food Engineering, 159, 36–41.

[61] Mayerhöfer, T. G., Pahlow, S., & Popp, J. (2020). The Bouguer-Beer-Lambert Law: Shining Light on the Obscure. Chemphyschem, 21(18), 2029–2046.

[62] Kucuk, H., Midilli, A., Kilic, A., & Dincer, I. (2014). Review on Thin-Layer Drying-Curve Equations. Drying Technology, 32(7), 757–773.

[63] Silva, A. F., Sarraguça, M. C., Fonteyne, M., Vercruysse, J., De Leersnyder, F., Vanhoorne, V., Bostijn, N., Verstraeten, M., Vervaet, C., Remon, J. P., De Beer, T., & Lopes, J. A. (2017). Multivariate statistical process control of a continuous pharmaceutical twin-screw granulation and fluid bed drying process. International Journal of Pharmaceutics, 528(1-2), 242–252.

[64] Susarla, R., Sievens-Figueroa, L., Bhakay, A., Shen, Y., Jerez-Rozo, J. I., Engen, W., … Davé, R. N. (2013). Fast drying of biocompatible polymer films loaded with poorly water-soluble drug nano-particles via low temperature forced convection. International Journal of Pharmaceutics, 455(1–2), 93–103.

[65] Ben Haj Said, L., Najjaa, H., Farhat, A., Neffati, M., & Bellagha, S. (2015). Thin layer convective air drying of wild edible plant (Allium roseum) leaves: experimental kinetics, modeling and quality. Journal of Food Science and Technology, 52(6), 3739–3749.

[66] Li X, Zhao Y, Zhao C. Applications of capillary action in drug delivery. iScience. 2021 Jul 1;24(7):102810. doi: 10.1016/j.isci.2021.102810. PMID: 34296074; PMCID: PMC8282986.

[67] Salager, S., ElYoussoufi, M. S., & Saix, C. (2010). Effect of temperature on water retention phenomena in deformable soils: theoretical and experimental aspects. European Journal of Soil Science, 61(1), 97–107.

[68] Akpinar, E. K., & Toraman, S. (2016). Determination of drying kinetics and convective heat transfer coefficients of ginger slices. Heat and Mass Transfer, 52(10), 2271–2281

[69] Grote, S., & Kleinebudde, P. (2018). Roll Compaction/Dry Granulation of Dibasic Calcium Phosphate Anhydrous—Does the Morphology of the Raw Material Influence the Tabletability of Dry Granules? Journal of Pharmaceutical Sciences, 107(4), 1104–1111.

Chapter 5 – Conclusions and Recommendations

5.1 Conclusions

The use of synchrotron-based X-ray imaging techniques was used to visualize and quantify the internal pore structure and moisture content changes of single pharmaceutical granules during the dynamic drying process. The results of this research determined a correlation between the drying gas velocity and temperature with the rate of drying for a variety of formulations that follow the Henderson and Pabis thin-layer drying model, with further implications of changes to the thermal conductivity and specific heat capacity dependent on moisture content and porosity changes observed during drying.

A transient-line heat source method was implemented to investigate the effect of moisture content and porosity on the thermal conductivity and volumetric specific heat capacity of pure components and binary mixtures of acetaminophen, microcrystalline cellulose, and lactose monohydrate. It was found that both the thermal conductivity and volumetric specific heat capacity increased with increasing moisture content for all samples, with a decrease in the porosity observed with increasing moisture content. Furthermore, increasing the active pharmaceutical ingredient loading on binary mixtures for both excipients exhibited a trend toward the pure active ingredient's properties. A three-parameter linear regression model was fitted to all datasets to predict the thermal properties at varying conditions, with a good statistical fit found with the contribution of moisture content and porosity included in the model.

Synchrotron X-ray micro-computed tomography was used to investigate the effects of drying air temperature and velocity on the drying time of the single pharmaceutical granules. The pharmaceutical powders included pure components of acetaminophen and carbamazepine to determine hydrophilic and hydrophobic effects respectively, with binary mixtures generated with common excipients of either microcrystalline cellulose or lactose monohydrate to determine the effect of active ingredient loading. Segmentation of the collected data was performed to reveal changes to the pore volume during dynamic drying, with moisture content determined through the changes to the attenuation values of the extracted granule region. Drying time and composition were determined to significantly influence the changes to the pore volume and moisture content for all samples. The drying gas velocity and temperature were found to possess mixed significance depending on the sample composition.

For the first time, in-situ advanced synchrotron X-ray imaging techniques were used to monitor the drying process for single pharmaceutical granules, evaluating changes to the pore volume and moisture content. An advanced understanding of dynamic drying for single granules was obtained, with further implications of predicting changes to thermal properties throughout the drying process. The new findings of this study are beneficial to modelling the drying behaviour through equations such as Fourier's law of heat conduction, while further improving the selection of pharmaceutical materials and process conditions for drying processes within the pharmaceutical industry.

5.2 Recommendations

The results of this research demonstrate the utility of synchrotron X-ray computed tomography for rapidly occurring dynamic processes including the dynamic drying of single pharmaceutical granules.

Further improvements into the method can be made, including a larger field of view that maintains the temporal resolution; and further variations to the operating conditions to better quantify the effects of parameters such as drying gas velocity, temperature, and granule composition, namely, the materials composition. The application of this advanced imaging technique can be extended to various other materials where drying is a key unit operation, such as the agriculture and mining sectors.

Intrinsically, the application of synchrotron X-ray computed tomography is not limited to a single beamline and beam-type. The application of alternative beamlines can be explored further, with the use of a monochromatic beam capable of obtaining more precise attenuation values, reducing deviations in the photon energies that are present in a filtered, white beam.

Lastly, this advanced imaging technique can be applied to downstream dynamic process related to tableting that present a research topic of interest, with the rapid wetting and dissolution of pharmaceutical tablets presenting itself as topic that can be explored within future research.

Appendices

Appendix A – Sample Reconstruction Parameters for Image Processing

For detailed information regarding the ufo-kit software package and the data reconstruction tools used, please see the GitHub webpage for EZ-UFO located at:

https://github.com/sgasilov/ez_ufo?tab=readme-ov-file

Further reading into the applications of the ufo-kit software and tofu can be found in Faragó et al. [1].

[1] Faragó, T., Gasilov, S., Emslie, I., Zuber, M., Helfen, L., Vogelgesang, M., & Baumbach, T. (2022). Tofu: a fast, versatile and user-friendly image processing toolkit for computed tomography. Journal of Synchrotron Radiation, 29(3), 916-927.

Example Reconstruction Parameters

*** General ***

Input directory /experiments/bmitremoteuser2/Desktop/37G13137Raw/2024-4-5-BM/Carter/APAP_001

CT set scan_000

Center of rotation 799.0 (user defined)

Dimensions of projections 700 x 1600 (height x width)

Number of projections 1500

*** Preprocessing ***

None

*** Image filters ***

Remove large spots disabled

Phase retrieval enabled

energy 20.0 keV

pixel size 5.5 um

sample-detector distance 0.5 m

delta/beta ratio 2.3010299956639813

*** Ring removal ***

RR with ufo 2D stripes filter

sigma horizontal 10 sigma vertical 1*** Region of interest ***

Vertical ROI: all rows

ROI in slice plane not defined

*** Reconstructed values ***

8 bit

Min value in 32-bit histogram -2.829e-07

Max value in 32-bit histogram 4.507e-07

*** Optional reco parameters ***

Example UFO Specific Parameters

```
ezvars:
  COR:
    min-std-apply-pr:
      value: false
    patch-size:
      value: 256
    search-interval:
      value: 1010,1030,0.5
    search-method:
      value: 3
    search-row:
      value: 100
    user-defined-ax:
      value: 799.0
    user-defined-dax:
      value: 0.0
  RR:
    enable-RR:
      value: true
    spy-narrow-window:
      value: 21
    spy-rm-wide:
      value: false
    spy-wide-SNR:
      value: 3
    spy-wide-window:
      value: 91
```

```
  sx:
    value: 10
  sy:
    value: 1
  ufo-2d:
    value: false
  use-ufo:
    value: true
advanced:
  enable-optimization:
    value: false
  more-reco-params:
    value: false
  parameter-type:
    value: ''
filters:
  rm_spots:
    value: false
  spot-threshold:
    value: 1000.0
flat-correction:
  dark-scale:
    value: 1.0
  downsample:
    value: 4
  eigen-pco-downsample:
    value: 2
  eigen-pco-reps:
```

```
    value: 4
  flat-scale:
    value: 1.0
  smart-ffc:
    value: false
  smart-ffc-method:
    value: eigen
inout:
  bigtiff-output:
    value: false
  clip_hist:
    value: true
  darks-dir:
    value: darks
  dryrun:
    value: false
  flats-dir:
    value: flats
  flats2-dir:
    value: flats2
  input-dir:
    value: /experiments/bmitremoteuser2/Desktop/37G13137Raw/2024-4-5-
BM/Carter/APAP_001
  input_ROI:
    value: false
  keep-tmp:
    value: false
  open-viewer:
    value: false
```

output-ROI:

value: false

output-dir:

value: /experiments/bmitremoteuser2/Desktop/37G13137Rec/2024-4-5-BM/Carter_8bit/APAP_001

output-height:

value: 0

output-width:

value: 0

output-x:

value: 0

output-y:

value: 0

path2-shared-darks:

value: Absolute path to darks

path2-shared-flats:

value: Absolute path to flats

path2-shared-flats2:

value: Absolute path to flats2

preprocess:

value: false

preprocess-command:

value: remove-outliers size=3 threshold=500 sign=1

save-params:

value: true

shared-df-used:

value: false

shared-flats-after:

value: false

```
  shared-flatsdarks:
    value: false
  tmp-dir:
    value: /experiments/bmitremoteuser2/tmp-ezufo
  tomo-dir:
    value: tomo
nlmdn:
  bigtiff_output:
    value: false
  do-after-reco:
    value: false
  dryrun:
    value: false
  estimate-sigma:
    value: false
  fast:
    value: true
  h:
    value: 0.0
  input-dir:
    value: /experiments/bmitremoteuser2
  input-is-1file:
    value: false
  output_pattern:
    value: /experiments/bmitremoteuser2-nlmfilt
  patch-radius:
    value: 3
  search-radius:
```

```
      value: 10
    sigma:
      value: 0.0
    window:
      value: 0.0
  retrieve-phase:
    apply-pr:
      value: true
sections:
  cone-beam-weight:
    axis-angle-x:
      value: '30.0'
    center-position-z:
      value: '0.0'
  dfi: {}
  estimate: {}
  fbp: {}
  find-large-spots:
    gauss-sigma:
      value: 2.0
    spot-threshold:
      value: 1000.0
  flat-correction: {}
  general:
    output-bitdepth:
      value: 8
    output-maximum:
      value: 4.507e-07
```

```
  output-minimum:
    value: -2.829e-07
  verbose:
    value: false
general-reconstruction:
  axis-angle-y:
    value: '0.0'
  data-splitting-policy:
    value: one
  num-gpu-threads:
    value: null
  overall-angle:
    value: 360.0
  slice-memory-coeff:
    value: 0.7
  slices-per-device:
    value: null
  volume-angle-z:
    value: '0.0'
gui: {}
inpaint: {}
ir: {}
laminographic-reconstruction: {}
perf: {}
preprocess: {}
reading:
  height:
    value: 200
```

```
  step:
    value: 1
  y:
    value: 500
  y-step:
    value: 5
reconstruction: {}
retrieve-phase:
  energy:
    value: 20.0
  pixel-size:
    value: 5.5e-06
  propagation-distance:
    value: '0.5'
  regularization-rate:
    value: 2.3010299956639813
sart: {}
sbtv: {}
sinos: {}
tomographic-reconstruction: {}
```

Appendix B – Derivation of the Empirical Correlations for Thermal Conductivity and Volumetric Specific Heat Capacity

Thermal Conductivity

$$k = k_s^*(1-\varepsilon) + k_g\varepsilon$$

$$k_s^* = k_s(1-M) + k_l M$$

$$k = (k_s^* * (1-M) + k_l * M)(1-\varepsilon) + k_g * \varepsilon$$

or

$$k = (A * (1-M) + B * M)(1-\varepsilon) + C * \varepsilon$$

Volumetric Specific Heat Capacity

$$\rho C_p = \rho C_{p,s}^*(1-\varepsilon) + \rho C_{p,g}\varepsilon$$

$$\rho C_{p,s}^* = \rho C_{p,s}(1-M) + \rho C_{p,l} M$$

$$\rho C_p = \left(\rho C_{p,s}^* * (1-M) + \rho C_{p,l} * M\right)(1-\varepsilon) + \rho C_{p,g} * \varepsilon$$

or

$$\rho C_p = (D * (1-M) + E * M)(1-\varepsilon) + F * \varepsilon$$

Appendix C - Permissions

The following pages provide permissions for the reuse of figures in Chapter 2 as part of the dissertation/thesis.

JOHN WILEY AND SONS LICENSE
TERMS AND CONDITIONS
Jul 26, 2024

This Agreement between Carter Blocka ("You") and John Wiley and Sons ("John Wiley and Sons") consists of your license details and the terms and conditions provided by John Wiley and Sons and Copyright Clearance Center.

License Number	5836690610507
License date	Jul 26, 2024
Licensed Content Publisher	John Wiley and Sons
Licensed Content Publication	Canadian Journal of Chemical Engineering
Licensed Content Title	Contacting modes and behaviour classification of gas—solid and other two-phase suspensions
Licensed Content Author	John R. Grace
Licensed Content Date	Mar 26, 2009
Licensed Content Volume	64
Licensed Content Issue	3
Licensed Content Pages	11
Type of use	Dissertation/Thesis
Requestor type	University/Academic
Format	Electronic
Portion	Figure/table
Number of figures/tables	1
Will you be translating?	No
Title of new work	In-situ Study of Single Pharmaceutical Granule Drying using Synchrotron X-ray Imaging
Institution name	University of Saskatchewan
Expected presentation date	Sep 2024
Portions	Image of different fluidization regimes with increasing gas velocity (fixed bed to pneumatic conveying)
The Requesting Person / Organization to Appear on the License	Carter Blocka

	University of Saskatchewan 57 Campus Drive
Requestor Location	
	Saskatoon, SK S7N 5A9 Canada Attn: University of Saskatchewan
Publisher Tax ID	EU826007151
Total	0.00 CAD
Terms and Conditions	

TERMS AND CONDITIONS

JOHN WILEY AND SONS LICENSE
TERMS AND CONDITIONS
Jul 26, 2024

This Agreement between Carter Blocka ("You") and John Wiley and Sons ("John Wiley and Sons") consists of your license details and the terms and conditions provided by John Wiley and Sons and Copyright Clearance Center.

License Number	5836691012309
License date	Jul 26, 2024
Licensed Content Publisher	John Wiley and Sons
Licensed Content Publication	Canadian Journal of Chemical Engineering
Licensed Content Title	Experimental investigation on drying performance of pharmaceutical granules in a pulsation-assisted fluidized bed dryer
Licensed Content Author	Chen Li, Carter Blocka, Lifeng Zhang
Licensed Content Date	Jun 24, 2022
Licensed Content Volume	100
Licensed Content Issue	9
Licensed Content Pages	15
Type of use	Dissertation/Thesis
Requestor type	Author of this Wiley article
Format	Electronic
Portion	Figure/table
Number of figures/tables	1
Will you be translating?	No
Title of new work	In-situ Study of Single Pharmaceutical Granule Drying using Synchrotron X-ray Imaging
Institution name	University of Saskatchewan
Expected presentation date	Sep 2024
Portions	Figure 8
The Requesting Person / Organization to Appear on the License	Carter Blocka

	University of Saskatchewan 57 Campus Drive
Requestor Location	
	Saskatoon, SK S7N 5A9 Canada Attn: University of Saskatchewan
Publisher Tax ID	EU826007151
Total	0.00 CAD
Terms and Conditions	

TERMS AND CONDITIONS

ELSEVIER LICENSE
TERMS AND CONDITIONS
Jul 26, 2024

This Agreement between Carter Blocka ("You") and Elsevier ("Elsevier") consists of your license details and the terms and conditions provided by Elsevier and Copyright Clearance Center.

License Number	5836691170766
License date	Jul 26, 2024
Licensed Content Publisher	Elsevier
Licensed Content Publication	International Journal of Pharmaceutics
Licensed Content Title	4D study of liquid binder penetration dynamics in pharmaceutical powders using synchrotron X-ray micro computed tomography
Licensed Content Author	Sima Zeinali Danalou,Xiao Fan Ding,Ning Zhu,Heather N. Emady,Lifeng Zhang
Licensed Content Date	Nov 5, 2022
Licensed Content Volume	627
Licensed Content Issue	n/a
Licensed Content Pages	1
Start Page	122192
End Page	0
Type of Use	reuse in a thesis/dissertation
Portion	figures/tables/illustrations
Number of figures/tables/illustrations	1
Format	electronic
Are you the author of this Elsevier article?	No
Will you be translating?	No
Title of new work	In-situ Study of Single Pharmaceutical Granule Drying using Synchrotron X-ray Imaging
Institution name	University of Saskatchewan
Expected presentation date	Sep 2024
Portions	Figure 11
The Requesting Person / Organization to Appear on the License	Carter Blocka

	University of Saskatchewan 57 Campus Drive
Requestor Location	
	Saskatoon, SK S7N 5A9 Canada Attn: University of Saskatchewan
Publisher Tax ID	GB 494 6272 12
Total	0.00 CAD
Terms and Conditions	

INTRODUCTION